

Taking control of compressible modes: bulk viscosity and the turbulent dynamo

James R. Beattie^{1,2,3,1*}, Christoph Federrath^{1,4}, Neco Kriel¹, Justin Kin Jun Hew^{1,5,6}

& Amitava Bhattacharjee^{2,7}

¹Research School of Astronomy and Astrophysics, Australian National University, Canberra, ACT 2611, Australia

²Department of Astrophysical Sciences, Princeton University, Princeton, NJ 08544, USA

³Canadian Institute for Theoretical Astrophysics, University of Toronto, 60 St. George Street, Toronto, ON M5S 3H8, Canada

⁴Australian Research Council Centre of Excellence in All Sky Astrophysics (ASTRO3D), Canberra, ACT 2611, Australia

⁵Space Plasma Power and Propulsion Laboratory, Department of Nuclear Physics and Accelerator Applications, Research School of Physics, Australian National University, ACT 2601, Canberra, Australia

⁶Mathematical Sciences Institute, Australian National University, Canberra, ACT, 2601, Australia

⁷Princeton Plasma Physics Laboratory, Princeton University, Princeton, NJ 08544, USA

Accepted XXX. Received YYY; in original form ZZZ

ABSTRACT

Many polyatomic astrophysical plasmas are compressible and out of chemical and thermal equilibrium, and yet, a means to carefully control the decay of compressible modes in these systems has largely been neglected. This is especially important for small-scale, turbulent dynamo processes, which are known to be sensitive to the effects of compression. To control the viscous properties of the compressible modes, we perform supersonic, visco-resistive dynamo simulations with additional bulk viscosity ν_{bulk} , deriving a new ν_{bulk} Reynolds number Re_{bulk} , and viscous Prandtl number $\text{P}\nu \equiv \text{Re}_{\text{bulk}}/\text{Re}_{\text{shear}}$, where Re_{shear} is the shear viscosity Reynolds number. For $10^{-3} \leq \text{P}\nu \leq \infty$, we explore a broad range of statistics critical to the dynamo problem, including the integral and spectral energy ratios, growth rates, and the magnetic $E_{\text{mag}}(k)$ and kinetic $E_{\text{kin}}(k)$ energy spectrum. We derive a general framework for decomposing E_{mag} growth rates into incompressible and compressible terms via orthogonal tensor decompositions of $\nabla \otimes \mathbf{v}$, where \mathbf{v} is the fluid velocity. We find that compressible modes play a dual role, growing and decaying E_{mag} , and that field-line stretching is the main driver of growth, even in supersonic dynamos. In the absence of ν_{bulk} ($\text{P}\nu \rightarrow \infty$), compressible modes pile up on small-scales, creating a spectral bottleneck, which disappears for $\text{P}\nu \approx 1$. As $\text{P}\nu$ decreases, compressible modes are dissipated at increasingly larger scales, in turn suppressing incompressible modes through a coupling between viscosity operators. We emphasise the importance of further understanding the role of ν_{bulk} in compressible astrophysical plasmas and direct numerical simulations that include compressibility.

Key words: MHD – turbulence – dynamo – magnetic fields – plasmas

1 INTRODUCTION

Compressibility changes the nature of turbulence, from the energy cascade (e.g. Kritsuk et al. 2007; Lithwick & Goldreich 2001; Federrath 2013; Wang et al. 2018a; Ferrand et al. 2020; Federrath et al. 2021) to the magnetic field fluctuations embedded within the turbulent medium (e.g., Mee & Brandenburg 2006; Federrath 2016; White et al. 2019; Mandal et al. 2020; Beattie & Federrath 2020; Skolidis et al. 2021; Seta & Federrath 2021; Bott et al. 2021; Beattie et al. 2022b,a). Naturally, one way of parameterising the compressibility of a medium is through the root-mean-squared (rms) sonic Mach number $\mathcal{M} = \langle (v/c_s)^2 \rangle_V^{1/2}$ where v is the fluid velocity, V is the system volume and c_s is the sound speed within the

volume. Directly through the Rankine-Hugoniot shock jump relations, the rms \mathcal{M} tells us both the amplitude of a characteristic shock in a supersonic $\mathcal{M} > 1$ medium (Lehmann et al. 2016; Park & Ryu 2019), and by how much the shocks will compress the gas structure (Landau & Lifshitz 1959; Padoan & Nordlund 2011; Molina et al. 2012; Nolan et al. 2015; Federrath & Banerjee 2015; Beattie et al. 2020; Hew & Federrath 2023; Davidovits et al. 2022), which directly changes the statistics of all the fluid variables through flux freezing. Regardless of whether a plasma is compressible or not, in the presence of turbulent motions, magnetic fields will be grown and nourished through a small-scale, turbulent dynamo (also called fluctuation dynamo, or just small-scale dynamo (SSD); for reviews, Brandenburg & Subramanian 2005; Rincon 2019; Tobias 2021).

* E-mail: james.beattie@princeton.edu

Broadly speaking¹, the turbulent dynamo converts turbulent kinetic energy in the plasma into magnetic energy through a three-stage process. First, while $|\mathbf{b}| \ll |\mathbf{v}|$ – where \mathbf{b} is the magnetic field permeating through the fluid – the induction equation becomes (approximately) linear, leading to exponential growth in the volume-averaged magnetic energy, $\langle E_{\text{mag}} \rangle_V$,

$$\frac{d\langle E_{\text{mag}} \rangle_V}{dt} = 2\gamma_1 \langle E_{\text{mag}} \rangle_V. \quad (\text{kinematic}) \quad (1)$$

Considering the standard incompressible phenomenology, once the Reynolds stress becomes comparable to the magnetic tension $\nabla \cdot (\rho \mathbf{v} \otimes \mathbf{v}) \sim \nabla \cdot (\mathbf{b} \otimes \mathbf{b})$, the magnetic field exerts a back-reaction on the momentum equation (through the Lorentz force) in turn making the system of equations nonlinear, and suppressing the exponential growth until it becomes algebraic (specifically, linear) in time

$$\frac{d\langle E_{\text{mag}} \rangle_V}{dt} = 2\gamma_2. \quad (\text{nonlinear}) \quad (2)$$

Finally, with the field growth suppressed, the plasma resistivity balances with the growth terms and the velocity field maintains $\langle E_{\text{mag}} \rangle_V$ in a statistically stationary state where

$$\frac{d\langle E_{\text{mag}} \rangle_V}{dt} = 0, \quad (\text{saturated}) \quad (3)$$

where γ_1 and γ_2 are the growth rates of the respective stages (e.g., Schober et al. 2015; Xu & Lazarian 2016; Seta & Federrath 2020; Galishnikova et al. 2022; Kriel et al. 2025). Compared to incompressible, solenoidal turbulence, both the kinematic growth rate γ_1 and $t \rightarrow \infty$ ratio of the volume-averaged energy $\langle E_{\text{mag}} \rangle_V / \langle E_{\text{kin}} \rangle_V$ are reduced if the medium is highly compressible (Federrath et al. 2011; Schober et al. 2015; Seta & Federrath 2021; Sur & Subramanian 2023; Kriel et al. 2025) – that is, it appears more difficult to grow and maintain a strong magnetic field in the presence of continuously driven shocks than in their absence. In Section 3 we will discuss in more detail why this may be the case.

Considering the effects of compression on the turbulent dynamo is important for many astrophysical phenomena. For example, the interstellar medium in our Galaxy is turbulent and trans-sonic in volume-average (Gaensler et al. 2011), and turbulent and supersonic by mass-average (e.g., Klessen 2011; Federrath et al. 2016; Orkisz et al. 2017; Beattie et al. 2019). Hence, the coupling and flow of energy between the turbulence and magnetic fields that are embedded within the compressible interstellar medium are maintained with a super-to-trans-sonic dynamo (e.g., Beck & Wielebinski 2013; Xu & Lazarian 2016; McKee et al. 2020; Gent et al. 2023; Beattie et al. 2023). This means that all phenomena that either depend upon the magnetic field structure or amplitude in the interstellar medium, e.g., cosmic rays trapped on magnetic field lines, transported through the medium (Krumholz et al. 2020; Beattie et al. 2022a; Kempster et al. 2023; Lemoine 2023; Sampson et al. 2023), or stars forming in magnetised H_2 clouds (Federrath & Klessen 2012; Krumholz & Federrath

2019; McKee et al. 2020; Mathew & Federrath 2021), must have initial magnetic fields that are seeded and maintained by a supersonic turbulent dynamo (supersonic dynamo hereafter). Hence, all of these processes require an understanding of not just a dynamo, but a supersonic dynamo.

The supersonic dynamo is ubiquitous across many scales in an active galaxy. It has been shown that galaxy mergers excite these dynamos on kpc scales in the interstellar medium, (Pakmor et al. 2014, 2017; Brzycki & ZuHone 2019; Whittingham et al. 2021, 2023; Pfrommer et al. 2022), but they can also be found down at km scales in the plasma environment between merging neutrons stars (Aguilera-Miret et al. 2023a; Chabanov et al. 2023) and ubiquitously in quark gluon plasmas (e.g., Czajka et al. 2019). Of course, many of these phenomena contain more than a single dynamo operating in tandem. For example the magnetorotational instability dynamo, the α dynamo, shear current effect and ω dynamo (see Brandenburg & Ntormousi 2023, for recent review) have been found to all operate at the same time at least for some parameterisations of black hole accretion disks (Jacquemin-Ide et al. 2023). The turbulent dynamo fits into these dynamo ecosystems by efficiently building and maintaining the energy reservoir through the electromotive force, $\langle \mathbf{v} \times \mathbf{b} \rangle_V$, that in turn fuels the operation of the other dynamos (Rincon 2019; Brandenburg & Ntormousi 2023).

Even though compressibility has been shown to have a strong effect on the statistics of the turbulent dynamo, previous supersonic dynamo experiments have solely focused on the shear viscosity, ν_{shear} , and the corresponding shear Reynolds number Re_{shear} to control the viscous dissipative properties of the plasma. Changing Re_{shear} directly controls the decay timescale for the solenoidal modes e.g., $t_{\nu_{\text{shear}}} \sim (k_{\nu_{\text{shear}}}^2 \nu_{\text{shear}})^{-1}$ (where $k_{\nu_{\text{shear}}}$ is the dissipation wavenumber, with corresponding length scale $\ell_{\nu_{\text{shear}}}$), and the growth rate in the kinematic stage, $\gamma_1 \sim v_{\nu_{\text{shear}}} / \ell_{\nu_{\text{shear}}} \sim (\langle v^2 \rangle_V^{1/2}) \text{Re}_{\text{shear}}^{1/2}$ where the growth of the magnetic field is set by the dynamical timescale on $\ell_{\nu_{\text{shear}}}$ (Batchelor 1950; Yousef et al. 2007; Schekochihin et al. 2004c; Xu & Lazarian 2016; Galishnikova et al. 2022). However, the decay timescale (and corresponding length scale) for compressible modes, $t_{\nu_{\text{bulk}}} \sim (k_{\nu_{\text{bulk}}}^2 \nu_{\text{bulk}})^{-1}$ (and $\ell_{\nu_{\text{bulk}}}$), have been left to decay on the same timescale as the incompressible modes, where ν_{bulk} is the bulk (volume or longitudinal) viscosity (e.g., Pan & Johnsen 2017; Chen et al. 2019; Sharma & Kumar 2023), which we discuss in much more detail in Section 2. Because the dynamical timescale of compressible turbulent modes is known to be fast, $t \sim \ell / v_\ell \sim \ell / \ell^{1/2} \sim \ell^{1/2}$ (assuming Burgers 1948-type turbulence), compared to incompressible modes $t \sim \ell / \ell^{1/3} \sim \ell^{2/3}$ (assuming Kolmogorov 1941-type turbulence), this means that the diffusion timescale $t_{\nu_{\text{shear}}}$ may be insufficient to decay the compressible modes within a simulation domain. Therefore, even in direct numerical simulations that explicitly set Re_{shear} , the decay of the compressible modes may be governed completely by numerical dissipation, which is controlled by the numerical discretisation scheme for the fluxes in the simulation code, as well as the number of resolution elements in the simulation domain (Grete et al. 2023; Malvadi Shivakumar & Federrath 2023).

Theoretically, under the Stokes (1850) hypothesis, $\nu_{\text{bulk}} = 0$ is justified, and exact for mono-atomic gases (Tisza 1942), however, for di-atomic gases, such as H_2 , or tri-atomic gases

¹ Note we do not discuss the diffusion-free stage, which happens before the kinematic dynamo, where the magnetic field is successively folded to smaller-scales, until it reaches the resistive dissipation scale (Schekochihin et al. 2002b; Schekochihin et al. 2004c; St-Onge et al. 2020).

such as CO_2 , which are not in thermal or chemical equilibrium, the magnitude of the bulk viscosity can vary between tens and thousands of times larger than the shear viscosity (Pan & Johnsen 2017; Sharma & Kumar 2019; Sharma & Kumar 2023). This is certainly the case for the plasma entrapped by merging neutron stars (Camelio et al. 2023), which support dynamos excited by Kelvin Helmholtz instabilities (Chabanov et al. 2023), where strong bulk viscosities ($\nu_{\text{bulk}}/\nu_{\text{shear}} \gtrsim 100$; Most et al. 2022a,b) may play a role in the gravitational wave signatures of the merger events (Chabanov & Rezzolla 2023). Even beyond the theory of gases, the exact role of bulk viscosity on the numerics of supersonic turbulent dynamo simulations have remained largely unexplored.

In this study, we take the first steps toward describing the appropriate framework for bringing bulk viscosity into the context of turbulent dynamos. This includes defining new dimensionless plasma parameters, the bulk viscous Reynolds number, and the viscous Prandtl number, and making a number of important measurements that probe the role of this type of viscosity for the dynamo. Our results are not only broadly applicable to general poly-atomic plasmas, but also highly important for doing controlled studies of supersonic, magnetised gases, where spatial and temporal properties of compressible modes are controlled through an explicit viscosity operator. Our study is organised in the following manner. In Section 2 we introduce the bulk viscosity through orthogonal decompositions of the velocity gradient tensor, following a somewhat pedagogical approach. In Section 3 we go on to provide the theory for understanding compressibility in the context of key dynamo statistics – the growth rate and the saturated energy ratio. In Section 4 we describe the visco(both shear and bulk)-resistive magnetohydrodynamic (MHD) simulation setup that we use to explore the role of bulk viscosity in turbulent dynamos. In Section 5 we discuss the results of the saturation, dynamo growth rates, and in general, the volume integral quantities of the plasma, including decompositions into compressible and incompressible velocity modes. In Section 6 we explore the total, compressible and incompressible kinetic energy spectra, highlighting the effects of bulk viscosity, not just on the compressible spectrum, but also on the coupling between the compressible and incompressible modes through the mixing of the modes and viscosity operators. In Section 7 we focus on the magnetic spectra, the evolution of the integral scales. In Section 8 we combine the decomposed kinetic and magnetic energy spectra to explore how the dynamo saturates, on a mode-by-mode basis. Finally, in Section 9 we summarise and conclude.

2 FLUID VISCOSITY & THE VELOCITY GRADIENT TENSOR

2.1 Bulk and shear viscosity

The viscous momentum equation for a fluid is,

$$\frac{\partial \rho \mathbf{v}}{\partial t} + \nabla \cdot \mathbb{F} = \nabla \cdot \boldsymbol{\sigma}, \quad (4)$$

where \mathbb{F} is a tensor of conserved momentum fluxes, and $\boldsymbol{\sigma}$ is viscous stress tensor. Before kinetic theory showed us the way to describe $\boldsymbol{\sigma}$ through perturbations away from thermal equilibrium in the form of the Maxwell-Boltzmann distribution

function it was an empirical fact that for Newtonian fluids $\boldsymbol{\sigma}$ was proportional to the velocity gradient tensor $\nabla \otimes \mathbf{v}$, as,

$$\|\boldsymbol{\sigma}\| \sim \|\nabla \otimes \mathbf{v}\|, \quad (5)$$

where $\nabla \otimes \mathbf{v} = \partial_i v_j$ is the tensor product. By decomposing $\nabla \otimes \mathbf{v}$ into the rate of expansion \mathbb{B} , the traceless, symmetric, rate of strain \mathbb{S} , and the traceless, antisymmetric, rate of rotation \mathbb{A} , tensor components, one can gain some insight into the structure of this type of viscosity,

$$\nabla \otimes \mathbf{v} = \mathbb{B} + \mathbb{S} + \mathbb{A}, \quad (6)$$

$$\mathbb{B} = \frac{1}{3}(\nabla \cdot \mathbf{v})\mathbb{I}, \quad (7)$$

$$\mathbb{S} = \frac{1}{2}(\nabla \otimes \mathbf{v} + [\nabla \otimes \mathbf{v}]^T) - \frac{1}{3}(\nabla \cdot \mathbf{v})\mathbb{I}, \quad (8)$$

$$\mathbb{A} = \frac{1}{2}(\nabla \otimes \mathbf{v} - [\nabla \otimes \mathbf{v}]^T). \quad (9)$$

Because \mathbb{S} is traceless, $\text{tr}(\mathbb{S}) = \mathbb{S}_{xx} + \mathbb{S}_{yy} + \mathbb{S}_{zz} = 0$, it describes volume-preserving (incompressible and isochoric) transformations of fluid elements, and likewise for \mathbb{A} ; where $\text{tr}\{\dots\}$ is the trace operator. The difference is that all diagonal elements of \mathbb{A} are identically zero, hence there are no components of \mathbb{A} orthogonal to the fluid element, whereas $\text{tr}(\mathbb{S})$ sums to zero, hence the orthogonal forces exist, but cancel out over the whole element. Furthermore, \mathbb{S} is symmetric so $\mathbb{S} = \mathbb{S}^T$, and \mathbb{A} is anti-symmetric, $\mathbb{A} = -\mathbb{A}^T$, which constrains the types of transformations that are allowable for each tensor.

From this decomposition, it is clear that only \mathbb{B} and \mathbb{S} , contribute to the fluid viscosity, since

$$\mathbb{A} = \frac{1}{2}(\partial_j v_i - \partial_i v_j) = -\frac{1}{2}\epsilon_{ijk}\omega_k = \frac{1}{2} \begin{pmatrix} 0 & -\omega_z & \omega_y \\ \omega_z & 0 & -\omega_x \\ -\omega_y & \omega_x & 0 \end{pmatrix}, \quad (10)$$

where $\boldsymbol{\omega} = \nabla \times \mathbf{v}$ is the fluid vorticity, and ϵ_{ijk} is the Levi-Civita tensor. This is exactly the rate of rotation tensor, hence \mathbb{A} cannot be a source of fluid viscosity (see our derivation in Appendix A; note that \mathbb{A} describes the rigid body rotation of a fluid element along its path – formerly, antisymmetric matrices form a representation of the $\text{SO}(3)$ group, describing infinitesimal rotations of the fluid elements; Choudhuri 1998). We may therefore write the viscous stress tensor as,

$$\boldsymbol{\sigma} = 2\nu_{\text{shear}} \left[\frac{1}{2}(\nabla \otimes \mathbf{v} + [\nabla \otimes \mathbf{v}]^T) - \frac{1}{3}(\nabla \cdot \mathbf{v})\mathbb{I} \right] + \nu_{\text{bulk}}(\nabla \cdot \mathbf{v})\mathbb{I}, \quad (11)$$

where ν_{shear} and ν_{bulk} are the coefficients of bulk viscosity and the shear viscosity, respectively². Macroscopically, $\nu_{\text{bulk}}\mathbb{B}$ is the normal viscous stress associated with non-thermal-equilibrium changes to the volume of the fluid. To get insight into the microscopic description of ν_{bulk} , we turn to the two standard procedures for calculating it (which is more challenging than the shear viscosity; Sharma & Kumar 2023): Boltzmann equation-based relaxation time approximation and linear response theory (Sharma & Kumar 2019).

² Note that based on this definition $\nu_{\text{bulk}} = \lambda + 2\nu_{\text{shear}}/3$, where λ is the second viscosity coefficient (e.g., Emanuel 1990; Sharma & Kumar 2019), but we prefer to parameterise our simulations in terms of ν_{bulk} , which is equivalent to changing λ for fixed ν_{shear} .

Using the latter, for a dilute gas the bulk viscosity can be calculated,

$$\nu_{\text{bulk}} = \rho_{\text{eq}} c_s^2 \frac{\gamma - 1}{\gamma} \sum_i^N \frac{c_{v,i}}{c_v} \tau_i, \quad (12)$$

where ρ_{eq} is the equilibrium gas density, γ is the ratio of specific heats at equilibrium, $c_{v,i}$ is the heat capacity of the i^{th} internal mode, c_v is the total heat capacity and τ_i is the relaxation time for each mode (where it assumed $\omega \ll \tau_i^{-1}$ and ω is the sound wave frequency), summed over N rotational and vibrational degrees of freedom (Tisza 1942). It is then easy to see that ν_{bulk} is associated with the summed time lags τ_i that each internal mode takes to relax to thermal equilibrium (indeed, each mode may be decomposed into its own associated ν_{bulk} ; Shang et al. 2020). For mono-atomic gases, there are no such modes, so $\nu_{\text{bulk}} = 0$ (Stokes 1850 hypothesis), but for any other gas, this is no longer the case.

As Sharma & Kumar (2023) suggest in their review of bulk viscosity in fluid dynamics, the theory for bulk viscosity has largely been neglected in the literature. Here we summarise the few studies that are relevant to bulk viscosity in the context of fluid plasma turbulence. Chen et al. (2019) studied forced homogeneous isotropic (and hydrodynamical) turbulence (HIT) for moderate sonic Mach numbers $\mathcal{M} \leq 0.6$ and Taylor microscale Reynolds numbers $\text{Re}_{\text{shear}} \approx 100$. Through the kinetic energy spectrum, they showed that for large $\nu_{\text{bulk}}/\nu_{\text{shear}}$ ratios the turbulence almost returned to an incompressible state, i.e., the bulk viscosity acted primarily to decay the compressible modes. Pan & Johnsen (2017) studied the effect of bulk viscosity in decaying hydrodynamical turbulence, over a the same range of $\nu_{\text{bulk}}/\nu_{\text{shear}}$ that we do in our study, finding that high bulk viscosities enhanced the total decay rate of the kinetic energy by both suppressing the compressible modes in magnitude, and through the compressible mode-pressure and the compressible-incompressible mode interactions. However, they found that the incompressible modes were reasonably insensitive to bulk viscosity. Touber (2019) studied the eigen-modes of the Navier-Stokes equation with the addition of bulk viscosity, showing that in the Stokes (viscous) regime, significant bulk viscosity may be able to disrupt the small-scale, incompressible structures (the building blocks for enstrophy, ω^2) in the turbulence, enhancing the dissipation of the incompressible modes on small-scales. However, no studies exist in the MHD turbulence regime, nor in the presence of the turbulent dynamo, but if there is a strong coupling of the bulk viscosity at $\ell_{\nu_{\text{shear}}}$ (undoubtedly transitioning into the Stokes regime), then we should expect there to be an effect on the turbulent dynamo, since $\ell_{\nu_{\text{shear}}}$ is responsible for the magnetic field growth. To situate the bulk viscosity into a regular SSD formalism, we now define the dimensionless numbers that we can use to parameterise the additional bulk viscous fluxes in the momentum equation, and thus, our simulations.

2.2 Dimensionless plasma numbers

2.2.1 Viscous plasma numbers

The bulk viscosity, as in Equation 11, can be added simply as an additional viscous flux in the momentum equation of the

MHD fluid model, which we write for an isothermal fluid,

$$\begin{aligned} \frac{\partial \rho \mathbf{v}}{\partial t} - \nabla \cdot \left[\frac{1}{4\pi} \mathbf{b} \otimes \mathbf{b} - \rho \mathbf{v} \otimes \mathbf{v} - \left(c_s^2 \rho + \frac{b^2}{8\pi} \right) \mathbb{I} \right. \\ \left. + 2\nu_{\text{shear}} \rho \left\{ \frac{1}{2} \left(\nabla \otimes \mathbf{v} + [\nabla \otimes \mathbf{v}]^T \right) - \frac{1}{3} (\nabla \cdot \mathbf{v}) \mathbb{I} \right\} \right. \\ \left. + \nu_{\text{bulk}} \rho (\nabla \cdot \mathbf{v}) \mathbb{I} \right] = \rho \mathbf{S}, \end{aligned} \quad (13)$$

where ρ is the gas density, and $\rho \mathbf{S}$ is an arbitrary momentum source. One way of understanding the magnitude of each term in the momentum equation is to make it dimensionless to see how each term scales with dimensionless parameters. In light of this, we scale all length scales by L , all velocities by V , all times by $T = L/V$, all magnetic fields by B , and all densities by ρ_0 , such that, e.g., $\hat{\mathbf{v}} = \mathbf{v}/V$ (dimensionless quantities are denoted with hat-notation). As a simple example, the time-derivative term of the momentum becomes,

$$\frac{\partial \rho \mathbf{v}}{\partial t} \rightarrow \frac{\rho_0 V}{T} \frac{\partial \hat{\rho} \hat{\mathbf{v}}}{\partial \hat{t}} = \frac{\rho_0 V^2}{L} \frac{\partial \hat{\rho} \hat{\mathbf{v}}}{\partial \hat{t}}. \quad (14)$$

Let us non-dimensionalise the momentum equation, rearranging the magnetic tension and pressure,

$$\begin{aligned} \frac{\rho_0 V^2}{L} \frac{\partial \hat{\rho} \hat{\mathbf{v}}}{\partial \hat{t}} - \frac{1}{L} \hat{\nabla} \cdot \left[\frac{B^2}{4\pi} \left(\hat{\mathbf{b}} \otimes \hat{\mathbf{b}} - \frac{\hat{b}^2}{2} \mathbb{I} \right) - V^2 \rho_0 \hat{\rho} \hat{\mathbf{v}} \otimes \hat{\mathbf{v}} \right. \\ \left. - c_s^2 \rho_0 \hat{\rho} \mathbb{I} + \frac{2\nu_{\text{shear}} \rho_0 \hat{\rho} V}{L} \left[\frac{1}{2} \left(\hat{\nabla} \otimes \hat{\mathbf{v}} + [\hat{\nabla} \otimes \hat{\mathbf{v}}]^T \right) \right. \right. \\ \left. \left. - \frac{1}{3} (\hat{\nabla} \cdot \hat{\mathbf{v}}) \mathbb{I} \right] + \frac{\nu_{\text{bulk}} \rho_0 \hat{\rho} V}{L} (\hat{\nabla} \cdot \hat{\mathbf{v}}) \mathbb{I} \right] = \frac{\rho_0 V^2}{L} \hat{\rho} \hat{\mathbf{S}}. \end{aligned} \quad (15)$$

We can now divide the whole equation by $\rho_0 V^2/L$, appearing as the coefficient for the time derivative of the momentum,

$$\begin{aligned} \frac{\partial \hat{\rho} \hat{\mathbf{v}}}{\partial \hat{t}} - \hat{\nabla} \cdot \left[\frac{B^2}{4\pi \rho_0 V^2} \left(\hat{\mathbf{b}} \otimes \hat{\mathbf{b}} - \frac{\hat{b}^2}{2} \mathbb{I} \right) - \hat{\rho} \hat{\mathbf{v}} \otimes \hat{\mathbf{v}} - \frac{c_s^2}{V^2} \hat{\rho} \mathbb{I} \right. \\ \left. + 2 \frac{\nu_{\text{shear}} \hat{\rho}}{VL} \left[\frac{1}{2} \left(\hat{\nabla} \otimes \hat{\mathbf{v}} + [\hat{\nabla} \otimes \hat{\mathbf{v}}]^T \right) - \frac{1}{3} (\hat{\nabla} \cdot \hat{\mathbf{v}}) \mathbb{I} \right] \right. \\ \left. + \frac{\nu_{\text{bulk}} \hat{\rho}}{VL} (\hat{\nabla} \cdot \hat{\mathbf{v}}) \mathbb{I} \right] = \hat{\rho} \hat{\mathbf{S}}. \end{aligned} \quad (16)$$

Now we can make a number of observations. First, for the Lorentz force, $V_A^2 = B^2/(4\pi \rho_0)$, and $V_A^2/V^2 = 1/\mathcal{M}_A^2$ is the dimensionless Alfvén Mach number. Likewise, for the thermal pressure, $c_s^2/V^2 = 1/\mathcal{M}^2$ is the sonic Mach number. For the strain rate dissipation model $\text{Re}_{\text{shear}} \sim VL/\nu_{\text{shear}}$ and for the bulk dissipation model $\text{Re}_{\text{bulk}} \sim VL/\nu_{\text{bulk}}$. Hence, we can write the dimensionless momentum equation as,

$$\begin{aligned} \frac{\partial \hat{\rho} \hat{\mathbf{v}}}{\partial \hat{t}} - \hat{\nabla} \cdot \left[\frac{1}{\mathcal{M}_A^2} \left(\hat{\mathbf{b}} \otimes \hat{\mathbf{b}} - \frac{\hat{b}^2}{2} \mathbb{I} \right) - \hat{\rho} \hat{\mathbf{v}} \otimes \hat{\mathbf{v}} - \frac{\hat{\rho}}{\mathcal{M}^2} \mathbb{I} \right. \\ \left. + \frac{2\hat{\rho}}{\text{Re}_{\text{shear}}} \left(\frac{1}{2} [\hat{\nabla} \otimes \hat{\mathbf{v}} + (\hat{\nabla} \otimes \hat{\mathbf{v}})^T] - \frac{1}{3} (\hat{\nabla} \cdot \hat{\mathbf{v}}) \mathbb{I} \right) \right. \\ \left. + \frac{\hat{\rho}}{\text{Re}_{\text{bulk}}} (\hat{\nabla} \cdot \hat{\mathbf{v}}) \mathbb{I} \right] = \hat{\rho} \hat{\mathbf{S}}, \end{aligned} \quad (17)$$

which demonstrates how each of the terms in the momentum equation are related to each of the dimensionless constants³ we use to parameterise our FLASH simulations, including the new definition of Re_{bulk} .

More precisely than simple scaling arguments, the shear viscosity is controlled by changing the shear Reynolds number,

$$\text{Re}_{\text{shear}} = \frac{|\nabla \cdot (\rho \mathbf{v} \otimes \mathbf{v})|}{|2\nu_{\text{shear}} \nabla \cdot (\rho \mathbf{S})|} \sim \frac{\langle v^2 \rangle_{\mathbf{v}}^{1/2} \ell_0}{\nu_{\text{shear}}}, \quad (19)$$

and the bulk viscosity via the bulk Reynolds number,

$$\text{Re}_{\text{bulk}} = \frac{|\nabla \cdot (\rho \mathbf{v} \otimes \mathbf{v})|}{|\nu_{\text{bulk}} \nabla \cdot (\rho \mathbb{B})|} \sim \frac{\langle v^2 \rangle_{\mathbf{v}}^{1/2} \ell_0}{\nu_{\text{bulk}}}, \quad (20)$$

which in ratio (keeping ν_{shear} in the numerator, consistent with the definition of the magnetic Prandtl number) defines our viscous Prandtl number,

$$\text{P}\nu = \frac{\nu_{\text{shear}}}{\nu_{\text{bulk}}} = \frac{\text{Re}_{\text{bulk}}}{\text{Re}_{\text{shear}}} \sim \frac{t_{\nu_{\text{bulk}}}}{t_{\nu_{\text{shear}}}}. \quad (21)$$

With this definition, in the $\text{P}\nu \leq 1$ regime, bulk viscosity dominates over the shear viscosity ($t_{\nu_{\text{bulk}}} \leq t_{\nu_{\text{shear}}}$), and we therefore might expect that the compressible modes decay on larger scales than the incompressible modes, and vice versa for the $\text{P}\nu > 1$ regime ($t_{\nu_{\text{bulk}}} > t_{\nu_{\text{shear}}}$). We go through the natural implications of these two regimes on the energy spectra in the following Section 3. But before that, we turn our attention to the dimensionless parameters for the magnetic field.

2.2.2 Resistive plasma numbers

Performing the same analysis as above for fluid the induction equation with Ohmic resistivity gives,

$$\frac{\partial \hat{\mathbf{b}}}{\partial \hat{t}} - \hat{\nabla} \times (\hat{\mathbf{v}} \times \hat{\mathbf{b}}) = \frac{1}{\text{Rm}} \hat{\nabla}^2 \hat{\mathbf{b}}, \quad (22)$$

where

$$\text{Rm} = \frac{|\nabla \times (\mathbf{v} \times \mathbf{b})|}{|\eta \nabla^2 \mathbf{b}|} \sim \frac{\langle v^2 \rangle_{\mathbf{v}}^{1/2} \ell_0}{\eta}, \quad (23)$$

is the magnetic Reynolds number for the Ohmic resistivity and η is the Ohmic resistivity coefficient. Unlike Re_{shear} and $\ell_{\nu_{\text{shear}}}$, the dimensionless number Rm alone is not sufficient to

³ Previous studies have adopted $\text{Re}_{\text{shear}} = 2\pi \langle v^2 \rangle_{\mathbf{v}}^{1/2} / (k_0 \nu_{\text{shear}})$, where $k_0 = \ell_0 / (2\pi)$ is the turbulent driving scale in wavenumber space. This leads to a boost in Reynolds number by a factor of 2π , which seems confounding, since all we have done is substituted ℓ_0 for k_0 in the definition. However, note that real-space and wavenumber space statistics are linked by integrals, e.g.,

$$\langle v^2 \rangle_{\mathbf{v}}^{1/2} = \int_{\mathbb{V}_k} d\mathbf{k} |\mathbf{v}(\mathbf{k}) \mathbf{v}^*(\mathbf{k})|, \quad (18)$$

Parseval's theorem, where $|\mathbf{v}(\mathbf{k}) \mathbf{v}^*(\mathbf{k})|$ is the power spectrum of \mathbf{v} , and hence the velocity dispersion on k_0 is actually only a fraction of $\langle v^2 \rangle_{\mathbf{v}}^{1/2}$, $\langle v^2 \rangle_{k_0 + dk}^{1/2} = \int_{k_0}^{k_0 + dk} d\mathbf{k} |\mathbf{v}(\mathbf{k}) \mathbf{v}^*(\mathbf{k})|$. This means, to use a wavenumber definition of Re_{shear} , one has to also reduce $\langle v^2 \rangle_{\mathbf{v}}^{1/2}$ such that one is associating the correct velocities with the correct wavenumbers. This is unnecessarily complicated, so we always chose to use real-space Reynolds number definitions, which come directly from the momentum equation, as we have shown.

define the resistive scale in the turbulence (Schekochihin et al. 2004c; Galishnikova et al. 2022; Kriel et al. 2022; Brandenburg et al. 2023; Kriel et al. 2025). Instead, by balancing the stretching rate at the shear viscous scale, $v_{\ell_{\nu_{\text{shear}}}} / \ell_{\nu_{\text{shear}}}$ with the resistive dissipation rate, η / ℓ_{η}^2 , $v_{\ell_{\nu_{\text{shear}}}} / \ell_{\nu_{\text{shear}}} \sim \eta / \ell_{\eta}^2$, we can rearrange to find,

$$\frac{\ell_{\nu_{\text{shear}}}}{\ell_{\eta}} \sim \text{Pm}_{\text{shear}}^{1/2}, \quad (24)$$

where

$$\text{Pm}_{\text{shear}} = \frac{\nu_{\text{shear}}}{\eta} = \frac{\text{Rm}}{\text{Re}_{\text{shear}}}, \quad (25)$$

is the shear magnetic Prandtl number. Equation 24 is independent from the effects of compressibility (Kriel et al. 2025). Pm_{shear} parameterises the range of scales, $\ell_{\nu_{\text{shear}}} > \ell > \ell_{\eta}$ (the classical sub-viscous range; Schekochihin et al. 2002a, 2004c). We can furthermore define a bulk magnetic Prandtl number,

$$\text{Pm}_{\text{bulk}} = \frac{\nu_{\text{bulk}}}{\eta} = \frac{\text{Rm}}{\text{Re}_{\text{bulk}}}, \quad (26)$$

and it follows that,

$$\text{P}\nu = \frac{\text{Pm}_{\text{shear}}}{\text{Pm}_{\text{bulk}}}, \quad (27)$$

which relates all three of the Prandtl numbers that we define in this study. Pm_{bulk} , like Pm_{shear} may be related to a scale separation $\ell_{\nu_{\text{bulk}}} / \ell_{\eta} \sim \text{Pm}_{\text{bulk}}^{\alpha}$, if the $v_{\ell_{\nu_{\text{bulk}}}} \sim \ell_{\nu_{\text{bulk}}} / t_{\ell_{\nu_{\text{bulk}}}}$ modes are responsible changing the resistive properties of the plasma, but because Kriel et al. (2025) found that Equation 24 is universal for high and low \mathcal{M} , this is unlikely. We will constrain ourselves to a subset of the total parameter range in this study, keeping Re_{shear} and Pm_{shear} fixed, with $\text{Pm}_{\text{shear}} = 1$, but changing $\text{P}\nu$, which means Pm_{bulk} is solely determined by $\text{P}\nu$, $\text{Pm}_{\text{bulk}} = \text{P}\nu^{-1}$. This is because we are solely focusing on the role of bulk viscosity in the dynamo, and keeping Pm_{shear} and Re_{shear} fixed makes for a simple and informative experiment.

3 COMPRESSIBILITY IN THE TURBULENT DYNAMO

In this section we: (1) construct a general picture for what a compressible small-scale dynamo with bulk viscosity looks like in k space, using our parameterisations, $\text{P}\nu$, Pm_{shear} and \mathcal{M} ; and (2), highlight the theoretical aspects of the effects from compressible modes on the growth rate and saturation of the turbulent dynamo. We adopt an approach that focuses on the magnetic energy equation, as done before in Schekochihin et al. (2004c), Seta & Federrath (2021) and Sur & Subramanian (2023), with some important differences⁴. Let us begin with schematics of the dynamo energy spectrum.

⁴ Schekochihin et al. (2002b) considered only the incompressible magnetic energy equation, and both Seta & Federrath (2021) and Sur & Subramanian (2023) did not decompose the velocity gradient tensor to completely separate the incompressible and compressible tensors, \mathbb{A} , \mathbb{S} and \mathbb{B} , respectively, whilst trying to directly measure the effect of incompressible (stretching) and compressible effects in the dynamo. They only consider the effect of projecting the symmetric component of the velocity gradient tensor – the rate of strain tensor – the first term in Equation 35, onto the magnetic field, critically neglecting \mathbb{B} . Furthermore, Sur & Subrama-

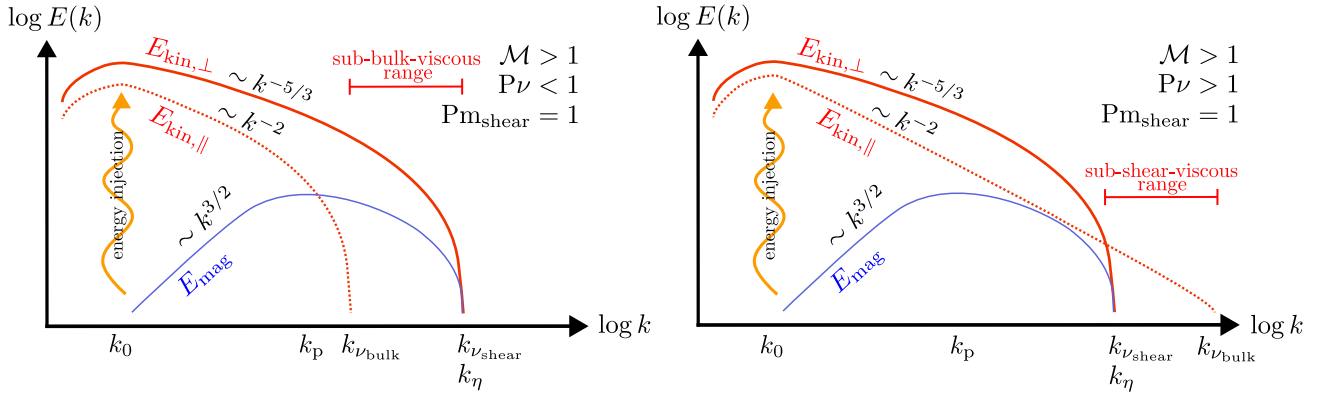


Figure 1. Schematics for the energy spectrum in the kinematic stage of the trans-sonic ($\mathcal{M} > 1$), turbulent dynamo with $\text{Pm}_{\text{shear}} = 1$ (Equation 25), varying $\text{P}\nu$ (Equation 21), including the incompressible ($E_{\text{kin},\perp}$; solid, red), compressible ($E_{\text{kin},\parallel}$; dotted, red) kinetic and magnetic spectra (E_{mag} ; blue). We annotate the energy injection scale k_0 , peak magnetic energy scale k_p , dissipation scale for the compressible modes $k_{\nu_{\text{bulk}}}$, dissipation scale for the incompressible modes $k_{\nu_{\text{shear}}}$ and dissipation scale for the magnetic field k_η on the $\log k$ axis. Note that for both the left and right panel, we have adopted a key result from Kriel et al. (2025), who showed that $k_p < k_{\nu_{\text{shear}}}$ for the compressible turbulent dynamo, as opposed to the incompressible case where $k_p \sim k_\eta$ (Schekochihin et al. 2002c; Schekochihin et al. 2004c). **Left:** The $\text{P}\nu < 1$ case, where $k_{\nu_{\text{shear}}} > k_{\nu_{\text{bulk}}}$, decaying the compressible modes faster than the incompressible modes and creating a sub-bulk-viscous range of scales $k_{\nu_{\text{bulk}}} < k < k_{\nu_{\text{shear}}}$, where $E_{\text{kin},\perp}(k) \gg E_{\text{kin},\parallel}(k)$. **Right:** The $\text{P}\nu > 1$ case, where $k_{\nu_{\text{bulk}}} > k_{\nu_{\text{shear}}}$, creating a sub-shear-viscous range in kinetic energies $k_{\nu_{\text{shear}}} < k < k_{\nu_{\text{bulk}}}$, where $E_{\text{kin},\parallel}(k) \gg E_{\text{kin},\perp}(k)$, and for $\text{Pm}_{\text{shear}} = 1$, $E_{\text{kin},\parallel}(k) \gg E_{\text{mag}}(k)$. The simulations presented in this study will not directly test the cascade exponents visualized in this schematic. For a Helmholtz decomposition showing the $E_{\text{kin},\perp}(k)$ and $E_{\text{kin},\parallel}(k)$ spectrum in the cascade, see recent work by Beattie et al. (2024), showing compressible MHD simulations at $10,080^3$ and $\text{Re}_{\text{shear}} \gtrsim 10^6$, showing explicitly this dichotomy.

3.1 Setting the scene for the compressible dynamo

We schematically represent the $\text{P}\nu < 1$ and $\text{P}\nu > 1$ regimes in Figure 1, with $\text{P}\nu < 1$ in the left panel, and $\text{P}\nu > 1$ in the right panel, respectively. Both panels correspond to $\text{Pm}_{\text{shear}} = 1 \implies \ell_{\nu_{\text{shear}}} \sim \ell_\eta$, and $\mathcal{M} > 1$ in both panels. We further annotate the fundamental scales for the dynamo problem: the integral or energy injection scale k_0 , the peak magnetic energy scale k_p , following the results from super-sonic dynamo experiments in Kriel et al. (2025), the viscous dissipation scales, $k_{\nu_{\text{shear}}}$ and $k_{\nu_{\text{bulk}}}$, and the magnetic energy dissipation scale k_η . We also annotate a Kolmogorov (1941)-type energy spectrum $\sim k^{-5/3}$ for the incompressible mode spectrum $E_{\text{kin},\perp}(k)$, giving rise to $\ell_0 \sim \text{Re}^{3/4} \ell_{\nu_{\text{shear}}}$, and a Burgers (1948)-type spectrum $\sim k^{-2}$ for the compressible mode spectrum $E_{\text{kin},\parallel}(k)$, which gives $\ell_0 \sim \text{Re}^{2/3} \ell_{\nu_{\text{bulk}}}$. This is also the acoustic wave spectrum for $\mathcal{M} < 1$. The simulations presented in this study will not directly test the cascade exponents presented in this schematic. For the exact $E_{\text{kin},\perp}(k)$ and $E_{\text{kin},\parallel}(k)$ spectrum in the cascade, see recent work by Beattie et al. (2024), showing compressible MHD simulations at $10,080^3$ and $\text{Re}_{\text{shear}} \gtrsim 10^6$, explicitly supporting Figure 1. For the magnetic field, we annotate a Kazantsev

(2023) do not make their stretching tensor traceless, just using $(\nabla \otimes \mathbf{v} + [\nabla \otimes \mathbf{v}]^T)/2$, which no longer makes \mathbb{S} volume-preserving, and hence is contaminated by isotropic compression. Neglecting the additional compression within $\nabla \otimes \mathbf{v}$ gives rise to overestimating the impact of compressions by a factor of 3 in Seta & Federrath (2021) and 6 in Sur & Subramanian (2023), which may significantly modify the 1st moment interpretations and conclusions presented in Sur & Subramanian (2023). Steinwandel et al. (2023) also neglect the \mathbb{B} contribution from within their $\hat{\mathbf{b}} \otimes \hat{\mathbf{b}} : \nabla \otimes \mathbf{v}$ term in the magnetic field energy equation for their magnetised intracluster medium simulations, which impacts their decomposition in a similar, negligible way as Seta & Federrath (2021).

(1968)-type spectrum $\sim k^{3/2}$. For $\text{P}\nu < 1$ (left panel), where the compressible modes decay on shorter timescales than the incompressible modes, a new sub-bulk-viscous range of scales

$$\ell_0 > \ell_{\nu_{\text{bulk}}} > \ell > \ell_{\nu_{\text{shear}}} \quad (\text{sub-bulk-viscous range}) \quad (28)$$

emerges, where $E_{\text{kin},\perp}(k) \gg E_{\text{kin},\parallel}(k)$. This regime is only achievable with explicit control over $k_{\nu_{\text{bulk}}}$, which we expect may lead to the small-scales becoming fundamentally incompressible. Conversely, for $\text{P}\nu > 1$ (right panel), a sub-shear-viscous range of scales emerges in the kinetic energy,

$$\ell_0 > \ell_{\nu_{\text{shear}}} > \ell > \ell_{\nu_{\text{bulk}}} \quad (\text{sub-shear-viscous range}) \quad (29)$$

where compressible modes are dominant, $E_{\text{kin},\parallel}(k) \gg E_{\text{kin},\perp}(k)$. For $\text{Pm} = 1$, the compressible kinetic energy on these scales will also be beyond the magnetic energy, $E_{\text{kin},\parallel}(k) \gg E_{\text{mag}}(k)$, making for an interesting range of scales that is naively fundamentally hydrodynamical, and dominated by compressions. If Figure 1 is representative of how bulk viscosity works, then the $\text{P}\nu > 1$ regime ought to be the regime that all $\mathcal{M} > 1$ simulations are in without any explicit bulk viscosity. It is not obvious if this is desirable, but what is desirable will clearly depend strongly on the $\text{P}\nu$ regime that exists in the turbulent plasma of interest. We aim to test the predictions outlined in this schematic in the remainder of the study.

Moreover, we further note that in the literature, previous studies have used the ratio $\nu_{\text{bulk}}/\nu_{\text{shear}}$ to parameterise the different plasma regimes, (e.g., Chen et al. 2019), but we prefer our definition⁵, which (1) explicitly defines the extra vis-

⁵ Note that because $\nu_{\text{bulk}} = (2/3)\nu_{\text{shear}} + \lambda$, $\text{P}\nu = 3\nu_{\text{shear}}/(2\nu_{\text{shear}} + 3\lambda)$, hence when $\text{P}\nu = 1$, $\nu_{\text{shear}}/\lambda = 3$, as expected from Equation 7. What this means is that at $\text{P}\nu = 1/3$ the dissipation timescale of the bulk and shear viscosity is the same, which we will later find is consistent with our simulation results.

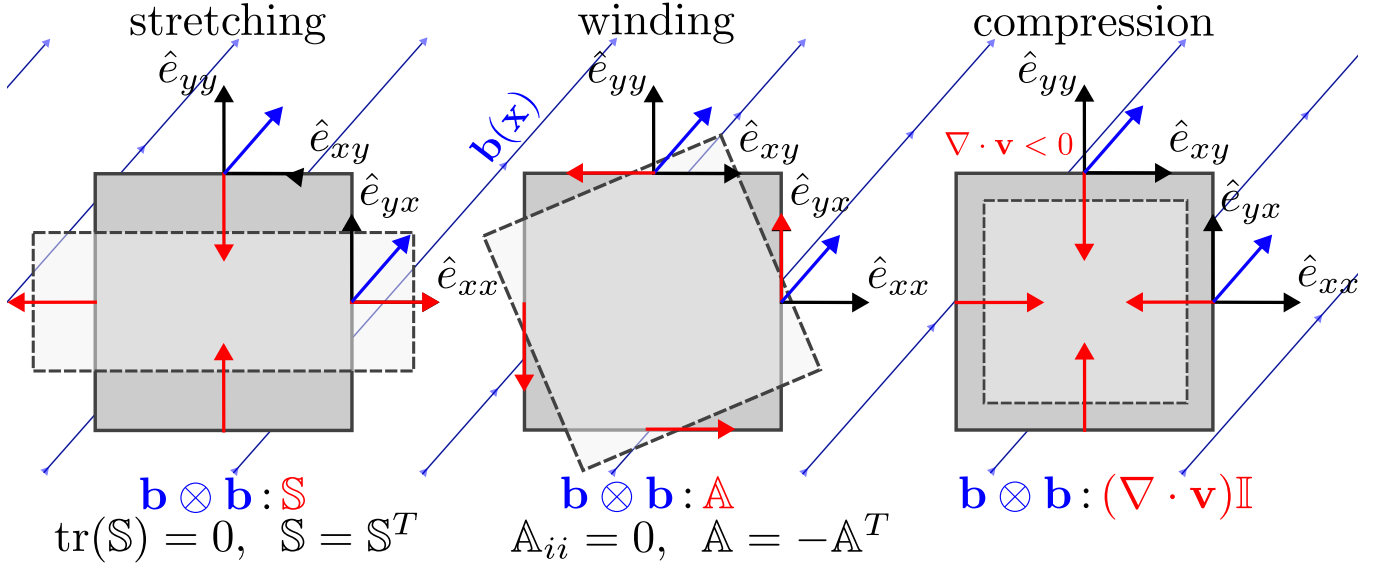


Figure 2. The three growth terms in Equation 35 visualised as orthogonal operations on the three 2D fluid elements (grey) that are evolving from the elements with solid lines to the elements with dashed lines. Key of the properties of the tensor operations are listed below the fluid elements. Each panel represents a geometrical projection between the blue (magnetic) vectors and the red vectors, which corresponds to the traceless rate of strain tensor \mathbb{S} (Equation 8; leftmost panel), the traceless rate of rotation tensor \mathbb{A} (Equation 9; central panel) and the rate of expansion tensor \mathbb{B} (Equation 7; rightmost panel). The \mathbb{S} and \mathbb{A} tensors enforce volume-preserving, incompressible transformations of the fluid element, that is $\text{tr}(\mathbb{S}) = \text{tr}(\mathbb{A}) = 0$ (orthogonal forces sum to zero). Note that we have represented only one possible stretching mode for \mathbb{S} , and \mathbb{S} also contains all shearing modes. \mathbb{A} only has components in the plane of the fluid element, with all orthogonal components being exactly zero, and all off-diagonal components being equal to the components of the fluid vorticity (Equation 10). Because $\mathbb{A} = -\mathbb{A}^T$, \mathbb{A} corresponds to shear-free rotations of the fluid element. The final $(\nabla \cdot \mathbf{v})\mathbb{I}$ tensor operation only has components in the orthogonal directions to the fluid element face. Each force must always point either away or into the fluid faces, because all components share the sign of $\nabla \cdot \mathbf{v}$. Hence $(\nabla \cdot \mathbf{v})\mathbb{I}$ is either a isotropic contraction, $\nabla \cdot \mathbf{v} < 0$, as shown in the schematic, or dilation $\nabla \cdot \mathbf{v} > 0$, changing the volume of the fluid element.

cosity through a bulk viscosity Reynolds number, and (2) puts the bulk viscosity in a framework similar to the resistivity and magnetic Prandtl number.

3.2 Turbulent dynamo growth

The 1st moment of the E_{mag} equation can be found by taking the scalar product of the magnetic field and induction equation and then averaging over space (similar to Schekochihin et al. 2002b; Seta & Federrath 2021, but retaining the full velocity gradient tensor and the effects of compressibility; see Appendix B for our derivation). Considering only Ohmic dissipation as a means of magnetic diffusion, it is,

$$\frac{d\langle E_{\text{mag}} \rangle_{\mathcal{V}}}{dt} = 2\gamma \langle E_{\text{mag}} \rangle_{\mathcal{V}} - 2\eta k_u^2 \langle E_{\text{mag}} \rangle_{\mathcal{V}}, \quad (30)$$

$$\gamma = \frac{\langle (\mathbf{b} \otimes \mathbf{b}) : [(\nabla \otimes \mathbf{v}) - \frac{1}{2}(\nabla \cdot \mathbf{v})\mathbb{I}] \rangle_{\mathcal{V}}}{\langle b^2 \rangle_{\mathcal{V}}}, \quad (31)$$

$$k_u^2 = \frac{\langle (\nabla \otimes \mathbf{b}) : (\nabla \otimes \mathbf{b}) \rangle_{\mathcal{V}}}{\langle b^2 \rangle_{\mathcal{V}}}, \quad (32)$$

noting that for the incompressible, kinematic case,

$$\gamma t_0 \sim \langle (\hat{\mathbf{b}} \otimes \hat{\mathbf{b}}) : (\nabla \otimes \mathbf{v}) \rangle_{\mathcal{V}} t_0 \sim t_0/t_{\nu_{\text{shear}}} \sim \text{Re}_{\text{shear}}^{1/2}, \quad (33)$$

since $\nabla \otimes \mathbf{v} \sim \mathbb{S} \sim t_{\nu_{\text{shear}}}^{-1}$, as expected and discussed in Section 1 for Kolmogorov (1941)-type turbulence. We know from Section 2.1 that we can decompose $\nabla \otimes \mathbf{v}$ into tensor

components for the different modes, \mathbb{S} and \mathbb{A} for the incompressible modes, and \mathbb{B} for the compressible modes. Hence we may write the γ equation as

$$\gamma = \underbrace{\frac{\langle (\mathbf{b} \otimes \mathbf{b}) : (\mathbb{S} + \mathbb{A}) \rangle_{\mathcal{V}}}{\langle b^2 \rangle_{\mathcal{V}}}}_{\text{incompressible}} + \underbrace{\frac{\langle (\mathbf{b} \otimes \mathbf{b}) : [\mathbb{B} - \frac{1}{2}(\nabla \cdot \mathbf{v})\mathbb{I}] \rangle_{\mathcal{V}}}{\langle b^2 \rangle_{\mathcal{V}}}}_{\text{compressible}}. \quad (34)$$

Splitting the incompressible term and using \mathbb{B} we find that the growth rate can be understood as the combination of fundamental fluid element deformations,

$$\gamma = \underbrace{\frac{\langle (\mathbf{b} \otimes \mathbf{b}) : \mathbb{S} \rangle_{\mathcal{V}}}{\langle b^2 \rangle_{\mathcal{V}}}}_{\text{stretching}} + \underbrace{\frac{\langle (\mathbf{b} \otimes \mathbf{b}) : \mathbb{A} \rangle_{\mathcal{V}}}{\langle b^2 \rangle_{\mathcal{V}}}}_{\text{winding}} - \underbrace{\frac{\langle (\mathbf{b} \otimes \mathbf{b}) : (\nabla \cdot \mathbf{v})\mathbb{I} \rangle_{\mathcal{V}}}{6 \langle b^2 \rangle_{\mathcal{V}}}}_{\text{compression}}. \quad (35)$$

The first term in Equation 35 is the projection of the magnetic field onto the velocity gradient field that stretches it. One may expect that this term must dominate the growth of the magnetic field, since field-line-stretching is well-known to be the key growth mechanism in the turbulent dynamo (Moffatt & Saffman 1964; Zel'dovich et al. 1984; Schekochihin et al. 2004c; Seta & Federrath 2021; Kriel et al. 2022; St-Onge et al. 2020). Next is the winding term, which is the projection of the magnetic field onto the rate of rotation tensor, Equation 10.

Consider $\mathbb{M} = \mathbf{b} \otimes \mathbf{b}$, and note that $\mathbb{M} = \mathbb{M}^T$ is symmetric ($b_i b_j = b_j b_i$). Then it follows from the definition of \mathbb{A} ,

$$\begin{aligned} \mathbb{M} : \mathbb{A} &= \text{tr} \{ \mathbb{M} \mathbb{A}^T \} = -\text{tr} \{ \mathbb{M} \mathbb{A} \}, \\ &= -\frac{1}{2} \text{tr} \{ \mathbb{M} (\nabla \otimes \mathbf{v}) \} + \frac{1}{2} \text{tr} \{ \mathbb{M} (\nabla \otimes \mathbf{v}) \} \\ &= 0, \end{aligned} \quad (36)$$

which means we expect $\langle (\mathbf{b} \otimes \mathbf{b}) : \mathbb{A} \rangle_{\mathcal{V}} / \langle b^2 \rangle_{\mathcal{V}} \equiv 0$. More broadly, this means turbulent magnetic fields are prevented from undergoing any kind of local winding to enhance or decay the field, quite unlike large-scale toroidal fields, which can undergo linear growth via winding (Aguilera-Miret et al. 2023b). The final term is the compression, which is the projection of the magnetic field onto the dilatational components of the fluid element. This term has a negative sign, with the total sign contribution of the term solely determined by the divergence, because

$$\langle (\mathbf{b} \otimes \mathbf{b}) : (\nabla \cdot \mathbf{v}) \mathbb{I} \rangle_{\mathcal{V}} = \text{tr} \{ (\mathbf{b} \otimes \mathbf{b}) (\nabla \cdot \mathbf{v}) \} = b^2 (\nabla \cdot \mathbf{v}). \quad (37)$$

Hence, for $\nabla \cdot \mathbf{v} < 0$, e.g., shocked fluid, the compressions enhance the growth rate by a local factor $(1/6)|\nabla \cdot \mathbf{v}|$. However, for rarefactions this term reduces the growth rate by the same factor. Therefore, one can ask, on average, in a volume, is the fluid dilated $\langle \nabla \cdot \mathbf{v} \rangle_{\mathcal{V}} > 0$ or compressed $\langle \nabla \cdot \mathbf{v} \rangle_{\mathcal{V}} < 0$? It is well known that for supersonic compressible turbulence, most of the fluid in the volume is $\langle \nabla \cdot \mathbf{v} \rangle_{\mathcal{V}} > 0$, with only a very small amount of the fluid contained with the $\nabla \cdot \mathbf{v} < 0$ structures (Passot & Vázquez-Semadeni 1998; Schmidt et al. 2008; Hopkins 2013; Squire & Hopkins 2017; Mocz & Burkhardt 2019; Beattie et al. 2022c and also see the $\nabla \cdot \mathbf{v}$ probability density function in Chen et al. 2019 and in Appendix A1 and A2 in Sur & Subramanian 2023). Hence as the compressions become stronger (for e.g., larger \mathcal{M}), this term, on average, ought to act to reduce the growth rate of the volume-averaged magnetic energy, which has been shown in numerical simulations (Federrath et al. 2011), however, not from evolving the bulk viscosity, but rather changing \mathcal{M} .

In the nonlinear induction stage Equation 2, $\langle E_{\text{mag}} \rangle_{\mathcal{V}} \sim E_{\text{kin}}(\ell_{\text{eq}})$, on energy equipartition scale ℓ_{eq} (St-Onge et al. 2020; Galishnikova et al. 2022; Beattie et al. 2023). Hence the growth term in Equation 30, $2\gamma \langle E_{\text{mag}} \rangle_{\mathcal{V}}$, becomes

$$2\gamma t_0 \langle E_{\text{mag}} \rangle_{\mathcal{V}} \sim \frac{\langle E_{\text{mag}} \rangle_{\mathcal{V}} E_{\text{kin}}^{1/2}(\ell_{\text{eq}})}{\ell_{\text{eq}}} t_0 \sim \frac{E_{\text{kin}}^{3/2}(\ell_{\text{eq}})}{\ell_{\text{eq}}} t_0, \quad (38)$$

which is approximately constant, giving rise to linear growth as described in Section 1.

3.3 Dynamo saturation

Let us explore Equation 30 in the saturated stage. Setting $\partial_t \langle E_{\text{mag}} \rangle_{\mathcal{V}} = 0$ for statistically stationary saturation,

$$\begin{aligned} \langle (\mathbf{b} \otimes \mathbf{b}) : \mathbb{S} \rangle_{\mathcal{V}} - \frac{1}{6} \langle (\mathbf{b} \otimes \mathbf{b}) : (\nabla \cdot \mathbf{v}) \mathbb{I} \rangle_{\mathcal{V}} = \\ \eta \langle (\nabla \otimes \mathbf{b}) : (\nabla \otimes \mathbf{b}) \rangle_{\mathcal{V}}, \end{aligned} \quad (39)$$

previously derived in Yousef et al. (2007) for incompressible turbulence. Very simply put, when the growth terms balance with the dissipation, the dynamo saturates. However, these may balance in at least three different ways: (1) the growth terms may be suppressed such that they eventually find their

way to $\eta \langle (\nabla \otimes \mathbf{b}) : (\nabla \otimes \mathbf{b}) \rangle_{\mathcal{V}}$, or (2) $\eta \langle (\nabla \otimes \mathbf{b}) : (\nabla \otimes \mathbf{b}) \rangle_{\mathcal{V}}$ may grow, eventually balancing with the growth terms, or (3) there is a mixture of both. For $\mathcal{M} \approx 0.2$ turbulence, Sur & Subramanian (2023) showed that $\eta \langle (\nabla \otimes \mathbf{b}) : (\nabla \otimes \mathbf{b}) \rangle_{\mathcal{V}}$ reduced by a small amount as the dynamo saturates⁶, hinting that it is the 1st moment growth terms that need to shrink to eventually reach a saturation. Hence, the incompressible growth term, $\langle (\mathbf{b} \otimes \mathbf{b}) : \mathbb{S} \rangle_{\mathcal{V}}$, is suppressed (presumably by the magnetic tension $\sim \nabla \cdot [\mathbf{b} \otimes \mathbf{b}]$). Schekochihin et al. (2004b) showed that this could be achieved through anisotropising the velocity field along folded field structures in $\mathbf{b} \otimes \mathbf{b}$. Furthermore, Seta & Federrath (2021) showed that in the saturation, $|\mathbf{u} \times \mathbf{b}| \approx 0$ for both $\mathcal{M} = 0.1$ and $\mathcal{M} = 10$ dynamos, which suggests that all tensor projection growth terms weaken in the saturation.

Moreover, as shown in Sur & Subramanian (2023) for the $\mathcal{M} > 1$ dynamo, the compressible growth term, $(1/6) \langle (\mathbf{b} \otimes \mathbf{b}) : (\nabla \cdot \mathbf{v}) \mathbb{I} \rangle_{\mathcal{V}}$, is suppressed by the magnetic field pressure gradients $\nabla b^2 / (8\pi)$ that are preferentially parallel to $\nabla \rho$, opposing compression, since shocked gas can generate large ∇b^2 , organising the magnetic field into filamentary structures that are supported by magnetic pressure (Molina et al. 2012; Beattie et al. 2022c; Kriel et al. 2025). This is relevant in regions of high ∇b^2 (corresponding to high mass), but in the magnetic voids, $(1/6) \langle (\mathbf{b} \otimes \mathbf{b}) : (\nabla \cdot \mathbf{v}) \mathbb{I} \rangle_{\mathcal{V}}$, which are the more volume-filling state of the gas, these terms act to reduce $\langle E_{\text{mag}} \rangle_{\mathcal{V}} / \langle E_{\text{kin}} \rangle_{\mathcal{V}}$, which ought to decrease final saturation of the dynamo. We will revisit these volume-averaged terms, computing them through the temporal evolution of the simulations in both the kinematic and saturated stage in Section 5.

4 NUMERICAL SIMULATIONS & METHODS

4.1 Visco-resistive magnetohydrodynamic fluid model

We use a modified version of the finite volume MHD code FLASH (Fryxell et al. 2000; Dubey et al. 2008), utilising a second-order conservative MUSCL-Hancock 5-wave approximate Riemann scheme (Bouchut et al. 2010; Waagan et al. 2011), and $\nabla \cdot \mathbf{b}$ parabolic diffusion flux cleaning (Marder 1987) to solve the 3D, visco-resistive, isothermal, compressible MHD equations with a stochastic acceleration field acting

⁶ Note that for $\mathcal{M} \approx 10$ turbulence Seta & Federrath (2021) showed that the Ohmic dissipation probability density function (the current; not simply the 1st moment, that we are commenting upon here) reduced in the saturation. This is also shown for the supersonic runs in Sur & Subramanian (2023).

Table 1. Main simulation parameters and derived quantities.

Sim. ID (1)	Re_{shear} (2)	Re_{bulk} (3)	$\text{P}\nu$ (4)	$\nu_{\text{shear}}t_0/\ell_0^2$ (5)	$\nu_{\text{bulk}}t_0/\ell_0^2$ (6)	\mathcal{M} (7)	$2\gamma_1t_0$ (8)	$\left(\frac{E_{\text{mag}}}{E_{\text{kin}}}\right)_{\text{sat}}$ (9)	$(\mathcal{M}_A)_{\text{sat}}$ (10)	N_{grid}^3 (11)
$\text{P}\nu\infty$	1000	∞	∞	1×10^{-3}	-	0.96 ± 0.03	1.48 ± 0.03	0.17 ± 0.03	2.49 ± 0.29	512^3
$\text{P}\nu 1_{1024}$	1000	1000	1	1×10^{-3}	1×10^{-3}	0.95 ± 0.03	1.42 ± 0.01	0.15 ± 0.04	2.62 ± 0.40	1024^3
$\text{P}\nu 1$	1000	1000	1	1×10^{-3}	1×10^{-3}	0.95 ± 0.03	1.42 ± 0.02	0.14 ± 0.03	2.71 ± 0.30	512^3
$\text{P}\nu 1_{256}$	1000	1000	1	1×10^{-3}	1×10^{-3}	0.95 ± 0.03	1.36 ± 0.04	0.15 ± 0.02	2.61 ± 0.22	256^3
$\text{P}\nu 1_{128}$	1000	1000	1	1×10^{-3}	1×10^{-3}	0.94 ± 0.04	1.36 ± 0.03	0.14 ± 0.04	2.76 ± 0.38	128^3
$\text{P}\nu 1\text{e-}1$	1000	100	0.1	1×10^{-3}	1×10^{-2}	0.94 ± 0.04	1.47 ± 0.05	0.20 ± 0.03	2.26 ± 0.30	512^3
$\text{P}\nu 1\text{e-}1_{256}$	1000	100	0.1	1×10^{-3}	1×10^{-2}	0.92 ± 0.03	1.44 ± 0.04	0.18 ± 0.05	2.44 ± 0.33	256^3
$\text{P}\nu 1\text{e-}1_{128}$	1000	100	0.1	1×10^{-3}	1×10^{-2}	0.93 ± 0.03	1.35 ± 0.05	0.12 ± 0.04	2.88 ± 0.36	128^3
$\text{P}\nu 1\text{e-}2$	1000	10	0.01	1×10^{-3}	1×10^{-1}	0.90 ± 0.02	1.46 ± 0.03	0.19 ± 0.07	2.38 ± 0.39	256^3
$\text{P}\nu 1\text{e-}3$	1000	1	0.001	1×10^{-3}	1×10^0	0.93 ± 0.04	1.28 ± 0.02	-	-	256^3

Notes. All simulations have magnetic Reynolds number $\text{Rm} = 1000$, corresponding to Ohmic resistivity coefficient $\eta = 1 \times 10^{-3} \ell_0^2/t_0$, a $\text{Pm}_{\text{shear}} = 1$ (Equation 25) and a $\text{Pm}_{\text{bulk}} = \text{P}\nu^{-1}$ (Equation 26), hence we list only the viscous material properties in the table. $\text{P}\nu 1\text{e-}3$ was not run to saturation due to the computational cost (extremely viscous, very small diffusion integration time step over long integration times), so we do not report saturated statistics for that simulation. **Column (1):** the unique simulation ID. **Column (2):** the shear Reynolds number of the plasma. **Column (3):** the same as column (2), but for the bulk viscosity. **Column (4):** the viscous Prandtl number. **Column (5):** the coefficient of shear viscosity in units of turbulent correlation times on the driving scale of the turbulence. **Column (6):** the same as column (5) but for the coefficient of bulk viscosity. **Column (7):** the turbulent Mach number in the kinematic stage of the dynamo. **Column (8):** the growth rate of the kinematic stage in units of turbulent correlation times. **Column (9):** the ratio of the volume-averaged magnetic energy and volume-averaged kinetic energy in the saturated stage of the dynamo. **Column (10):** the same as column (9) but for the Alfvénic Mach number. **Column (11):** the number of grid points used in the numerical discretisation. We perform a convergence study in Appendix C for both the $\text{P}\nu 1\text{e-}1$ and $\text{P}\nu 1$ simulations.

to drive the turbulence,

$$\frac{\partial \rho}{\partial t} + \nabla \cdot (\rho \mathbf{v}) = 0, \quad (40)$$

$$\begin{aligned} \frac{\partial \rho \mathbf{v}}{\partial t} + \nabla \cdot \left[\rho \mathbf{v} \otimes \mathbf{v} - \frac{1}{4\pi} \mathbf{b} \otimes \mathbf{b} \right. \\ \left. + \left(c_s^2 \rho + \frac{b^2}{8\pi} \right) \mathbb{I} \right] = \nabla \cdot (\rho \boldsymbol{\sigma}) + \rho \mathbf{f}, \end{aligned} \quad (41)$$

$$\frac{\partial \mathbf{b}}{\partial t} + \nabla \cdot (\mathbf{v} \otimes \mathbf{b} - \mathbf{b} \otimes \mathbf{v}) = -\eta \nabla \times \mathbf{j}, \quad (42)$$

$$\nabla \cdot \mathbf{b} = 0, \quad (43)$$

where the viscous stress tensor is

$$\boldsymbol{\sigma} = 2\nu_{\text{shear}}\mathbb{S} + \nu_{\text{bulk}}\mathbb{B}, \quad (44)$$

using the same definitions as in Section 2.1. We solve the equations on a triply periodic domain of dimension $\mathcal{V} \equiv L^3$, with uniform grids of $128^3 - 1024^3$ cells (we show a detailed convergence study in Appendix C, and implementation of the bulk viscosity in Appendix E), where $\langle \mathbf{b}(t) \rangle_{\mathcal{V}} = \langle \rho \mathbf{v}(t) \rangle_{\mathcal{V}} = 0$ (i.e., no net magnetic flux over \mathcal{V} , in the zero-momentum frame of \mathcal{V}), c_s is the sound speed, $\mathbf{j} = \nabla \times \mathbf{b}/(4\pi)$ is the current density, and \mathbf{f} is the stochastic turbulent acceleration source term that drives the turbulence.

4.2 Turbulent driving

The turbulent source term \mathbf{f} follows an Uhlenbeck & Ornstein (1930) process with finite e -fold correlation time, $t_0 = \ell_0 / \langle v^2 \rangle_{\mathcal{V}}^{1/2}$ (Schmidt et al. 2009; Federrath et al. 2010). The field \mathbf{f} is constructed in Fourier space with energy isotropically injected on the peak scale $|\mathbf{k}L/2\pi| = 2$ (equivalently, $\ell_0 = L/2$) and falls off to zero with a parabolic spectrum

within $1 \leq |\mathbf{k}L/2\pi| \leq 3$. On ℓ_0 we use t_0 and the energy injection rate to control the rms velocity, which we set to $\langle v^2 \rangle_{\mathcal{V}}^{1/2}/c_s = \mathcal{M} = 1.0$ in the kinematic stage of the dynamo, ensuring that we have compressible modes for the bulk viscosity to control. Furthermore, we inject energy such that $\mathbf{f}_{\perp}^2/\mathbf{f}_{\parallel}^2 = 2$, corresponding to 2:1 energy in incompressible $\nabla \cdot \mathbf{f}_{\perp} = 0$ and compressible $\nabla \times \mathbf{f}_{\parallel} = 0$ mode components of \mathbf{f} , ensuring that the compressible modes are being replenished on large-scales. See Federrath et al. (2010) and Federrath et al. (2022) for more details about the TURBGEN driving source. We integrate each of the experiments from $t/t_0 = 0$ to $t/t_0 = 100$, writing the 3D field variables to disk every $t/t_0 = 0.1$ for post-processing.

4.3 Setting Reynolds and Prandtl numbers

Following Section 2, we parameterise the visco-resistive properties of our simulations with five numbers. Throughout the study we fix $\text{Re}_{\text{shear}} = 1000$, corresponding to setting $\nu_{\text{shear}} = 1 \times 10^{-3} \ell_0^2/t_0$ in Equation 20. This ensures that the incompressible modes are in a state of turbulence in our simulations (Frisch 1995). We then vary $\text{P}\nu$ between $\text{P}\nu = \text{Re}_{\text{bulk}} = \infty$, where $\nu_{\text{bulk}} = 0$ (the dissipation is controlled purely by numerical means) to $\text{P}\nu = 0.001$, where the $\nu_{\text{bulk}} = 10^3 \nu_{\text{shear}}$ and $\text{Re}_{\text{bulk}} = 1$, which corresponds to $t_{\nu_{\text{bulk}}} \sim t_0$ (i.e., the diffusion is as fast as the dynamical time on ℓ_0 ; see column 6 in Table 1 where we write the viscous coefficients in units of t_0). For $\text{P}\nu > 1$, the simulations develop a sub-shear-viscous range, Equation 29, where the compressible modes ought to dominate at high- k ; and for $\text{P}\nu < 1$, they develop a sub-bulk-viscous range, Equation 28, where compressible modes are suppressed whilst incompressible modes are left to dynamically evolve with the turbulence. The two ranges of scales are shown schematically in Figure 1.

We control the resistivity by setting the magnetic Reynolds

number, Rm Equation 23. We choose $\eta = 1 \times 10^{-3} \ell_0^2/t_0$ corresponding to $Rm = 1000$. The extent of the (classical) sub-viscous range is set through the shear magnetic Prandtl number, Pm_{shear} (Equation 23; the regular Pm that has been studied in the small-scale dynamo; Schekochihin et al. 2004c; Federrath et al. 2014; Galishnikova et al. 2022; Kriel et al. 2022; Brandenburg et al. 2023; Kriel et al. 2025). Since $Re_{\text{shear}} = Rm = 1000$, $Pm_{\text{shear}} = 1$ for all of the simulations in our study, hence we decay the incompressible and magnetic modes similarly, without the development of a sub-viscous range, $\ell_\eta \leq \ell \leq \ell_{\nu_{\text{shear}}}$. We leave the study of the bulk viscosity in the context of evolving Pm_{shear} for future studies. Based on Equation 26, the corresponding bulk magnetic Prandtl number, Pm_{bulk} , is completely controlled by changing $P\nu$, because $Pm_{\text{bulk}} = P\nu^{-1}$ for $Pm_{\text{shear}} = 1$. Hence, for the remainder of the study, we focus only on the principle parameters that are evolved across the present simulations, Re_{bulk} and $P\nu$. All of our diffusion coefficients, ν_{shear} , ν_{bulk} , η are constant in time and space.

4.4 Initial field conditions

Following, e.g., Kriel et al. (2022), we initialise the velocity field to $|\mathbf{v}(x, y, z, t = 0)|/c_s = 0$, with units $c_s = 1$ and the density field $\rho(x, y, z, t = 0) = \rho_0$, where the density has units $\rho_0 = 1$. Likewise, \mathbf{b} has units of $c_s \rho_0^{1/2} = 1$, and is initialised as a Gaussian field in k -space with a parabolic spectral power distribution matching the turbulent forcing function. The total energy in the turbulent fluctuations of the field is set such that $\langle E_{\text{mag},0} \rangle_V / \rho_0 c_s^2 = 10^{-10} = \beta^{-1}$, where $\langle E_{\text{mag},0} \rangle_V$ is the initial volume integral energy and β is the plasma beta. This corresponds to an incredibly weak seed magnetic field compared to the constant thermal energy, allowing for the simulations to spend a significant time in the kinematic stage of the dynamo.

4.5 Helmholtz decomposition of velocity field

Any vector field can be written as a vector sum of curl-free and divergence-free vectors – the Helmholtz decomposition of a vector field. Because we are seeking to understand the role of bulk viscosity on the compressible modes in the super-sonic dynamo, we specifically decompose our \mathbf{v} into orthogonal compressible \mathbf{v}_\parallel ($\nabla \times \mathbf{v}_\parallel = 0$) and incompressible \mathbf{v}_\perp ($\nabla \cdot \mathbf{v}_\perp = 0$) modes, such that,

$$\mathbf{v} = \mathbf{v}_\parallel + \mathbf{v}_\perp. \quad (45)$$

This is easily done in Fourier space, where

$$\mathbf{v}_\parallel(\ell) = \Re \left\{ \int d\mathbf{k} [\mathbf{k} \cdot \tilde{\mathbf{v}}(\mathbf{k})] \mathbf{k} / k^2 e^{2\pi i \mathbf{k} \cdot \ell} \right\}, \quad (46)$$

is the real \Re component of the inverse Fourier transform of the Fourier transformed velocity $\tilde{\mathbf{v}}(\mathbf{k})$ projected along \mathbf{k} . Then $\mathbf{v}_\perp = \mathbf{v} - \mathbf{v}_\parallel$, ensuring that Equation 45 is maintained. Throughout this study we utilise the 1D shell-integrated (isotropic) power spectra for the magnetic and kinetic energy,

$$E_{\text{mag}}(k) = \frac{1}{8\pi} \int_{\Omega_k} d\Omega_k 4\pi k^2 |\tilde{\mathbf{b}}(\mathbf{k})|^2, \quad (47)$$

$$E_{\text{kin}}(k) = \frac{\rho_0}{2} \int_{\Omega_k} d\Omega_k 4\pi k^2 |\tilde{\mathbf{v}}(\mathbf{k})|^2, \quad (48)$$

where $d\Omega_k$ is the shell angle at radius k and $\tilde{\mathbf{b}}(\mathbf{k})$ and $\tilde{\mathbf{v}}(\mathbf{k})$ are the Fourier transforms of the magnetic and velocity field, respectively. We likewise create the $E_{\text{kin},\parallel}(k)$ and $E_{\text{kin},\perp}(k)$ spectrum, based on our definitions in Equation 45, for exploring the Helmholtz decomposed kinetic energies.

We show examples of two-dimensional slices of the Helmholtz decomposed velocity fields in Figure 3 in our $P\nu = \infty$ (top row) and $P\nu = 0.001$ simulations (bottom row). The first column corresponds to the total velocity field, the second column the incompressible \mathbf{v}_\perp field, and the last column the compressible \mathbf{v}_\parallel fields, all which are coloured by the magnitude normalised by the rms. Both the \mathbf{v} and \mathbf{v}_\parallel fields qualitatively remained unchanged by the strong bulk viscosity, however the \mathbf{v}_\parallel field loses all of its high- k structure, and becomes dominated by low- k modes that are being replenished by the forcing.

We show how this translates into changing $\nabla \cdot \mathbf{v}$ (middle panel) and $\nabla \times \mathbf{v}$ (right panel) in Figure 4, with $P\nu = \infty$ (top row), $P\nu = 0.1$ (middle row), and $P\nu = 0.001$ (bottom row) simulations, along with the structure of $E_{\text{mag}}/E_{\text{kin}}$ (left column). Similar to Figure 3, the largest effect that changing $P\nu$ has is shown in the $\nabla \cdot \mathbf{v}$ field, where strong, thin compressions (yellow) that form in the $P\nu = \infty$ simulations are diffusive and thick in the $P\nu = 0.1$ simulations, until they are completely dissipated away in the $P\nu = 0.001$ simulation. From this plot, it is also clear both $\nabla \times \mathbf{v}$ and $E_{\text{mag}}/E_{\text{kin}}$ are also losing high- k mode structure as $P\nu$ decreases. To understand this process quantitatively, we turn now to the integral energy statistics.

5 INTEGRAL ENERGIES AND GROWTH RATES

We start the exploration for the role of the bulk viscosity on the turbulent dynamo via the integral quantities of energy, growth rates and growth rate terms ($\mathbf{b} \otimes \mathbf{b}$ tensor projections) that we derived in Section 3.2.

5.1 Volume integrated energies

We define the volume integral energies as,

$$\langle E_{\text{mag}} \rangle_V = \frac{\langle b^2 \rangle_V}{8\pi}, \quad \langle E_{\text{kin}} \rangle_V = \frac{\langle \rho_0 v^2 \rangle_V}{2}, \quad (49)$$

which we will use throughout this entire study. We plot the integral energy ratio $\langle E_{\text{mag}} \rangle_V / \langle E_{\text{kin}} \rangle_V$ (top) and \mathcal{M} (bottom) in Figure 5, colouring by $P\nu$. These colours will be maintained throughout the entire study. In log-linear space, we immediately identify the kinematic (exponential growth; highlighted in dark violet) and saturated (stationarity; highlighted with grey) stages of the dynamo in the $\langle E_{\text{mag}} \rangle_V / \langle E_{\text{kin}} \rangle_V$ plot, which all experiments undertake (i.e., all simulations are above the critical Rm for small-scale dynamo growth; Ruzmaikin & Sokolov 1981; Haugen et al. 2004b; Schekochihin et al. 2004a; Federrath et al. 2014; Seta et al. 2015). In log-linear scale, the nonlinear stage (Equation 2) between the two regimes is quite obfuscated. However, it is clearly observed in the $\mathcal{M}(t/t_0)$ plot, shown in the bottom panel of Figure 5. The transition happens between $30 \leq t/t_0 \leq 70$ between kinematic and saturated stages. This corresponds to the backreacting magnetic field steepening the kinetic energy cascade as $\nabla \cdot (\rho \mathbf{v} \otimes \mathbf{v}) \sim \nabla \cdot (\mathbf{b} \otimes \mathbf{b}) + \nabla b^2$ throughout the k

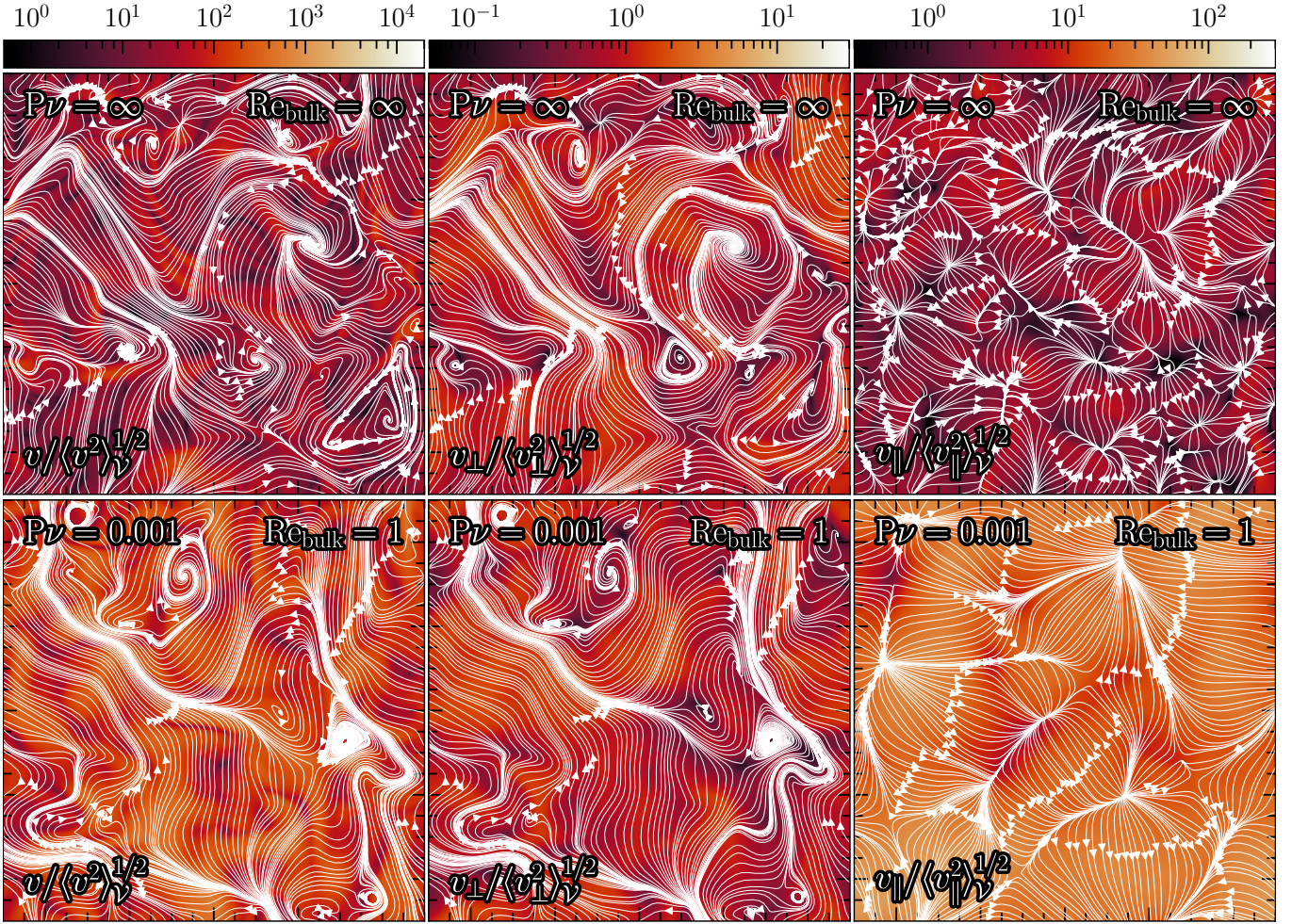


Figure 3. Two-dimensional slices of the total (v ; left), incompressible (v_{\perp} ; middle) and compressible (v_{\parallel} ; right) velocity modes in the kinematic stage ($t/t_0 = 30$) of the turbulent dynamo. All velocities are scaled by the rms, which determines the colour of the plots, with the corresponding vector field slice of the modes overlaid. The top row corresponds to the $P\nu = \infty$ simulation, where there is no explicit bulk viscosity, and the bottom row is for $P\nu = 0.001$, where the decay timescale of the bulk viscosity $t_{\nu_{\text{bulk}}}$ is comparable to the dynamical timescale of the turbulence on the outer scale t_0 . Both the $v/\langle v^2 \rangle_V^{1/2}$ and $v_{\perp}/\langle v_{\perp}^2 \rangle_V^{1/2}$ panels are aesthetically similar between the simulations, but the $v_{\parallel}/\langle v_{\parallel}^2 \rangle_V^{1/2}$ panels are vastly different, with only low- k v_{\parallel} modes left in the plasma when the bulk viscosity is strong.

modes in the cascade (see Fig. B1 in Beattie et al. 2023 and theory in Schekochihin et al. 2002a).

We tabulate all of the $\langle E_{\text{mag}} \rangle_V / \langle E_{\text{kin}} \rangle_V$ saturation statistics in Table 1, averaged over the saturated $\langle E_{\text{mag}} \rangle_V / \langle E_{\text{kin}} \rangle_V$ and \mathcal{M}_A in the grey region, $t/t_0 \geq 75$, all of which indicate a quite small effect throughout $0.01 \leq P\nu \leq \infty$ range, always maintaining $\langle E_{\text{mag}} \rangle_V / \langle E_{\text{kin}} \rangle_V \approx 0.15$, corresponding to $\mathcal{M}_A \approx 2.5$, consistent within 1σ with $P\nu = \infty$ calculations in Federrath et al. (2011). This indicates that the bulk viscosity does not have a large effect on the low- k modes, which dominate the integral energies (Beattie et al. 2022a). This is suggestive that previous \mathcal{M} dependencies upon small-scale dynamo saturation, e.g., Federrath et al. (2011); Seta & Federrath (2021); Sur & Subramanian (2023), are being controlled (more specifically the magnetic field being suppressed) by the lowest k modes. Performing the same calculation with

instead the Helmholtz decomposed integral kinetic energies,

$$\langle E_{\text{kin},\parallel} \rangle_V = \frac{\langle \rho_0 v_{\parallel}^2 \rangle_V}{2}, \quad \langle E_{\text{kin},\perp} \rangle_V = \frac{\langle \rho_0 v_{\perp}^2 \rangle_V}{2}, \quad (50)$$

provides a clearer picture for how the bulk viscosity effects the integral plasma quantities.

In Figure 6 we show the $\langle E_{\text{mag}} \rangle_V / \langle E_{\text{kin},\parallel} \rangle_V$ (solid lines) and $\langle E_{\text{mag}} \rangle_V / \langle E_{\text{kin},\perp} \rangle_V$ (dashed lines) in the top panel; and $\langle E_{\text{kin},\parallel} \rangle_V / \langle E_{\text{kin}} \rangle_V$ (solid lines) and $\langle E_{\text{kin},\perp} \rangle_V / \langle E_{\text{kin}} \rangle_V$ (dashed lines) ratios in the bottom panel, coloured in the same fashion as Figure 5. We turn our attention to the bottom panel. For all $P\nu$, we find the turbulence is dominated by the incompressible motions, even though we are replenishing the source on compressible modes with the same amount of energy as the incompressible modes in *f*. Federrath et al. (2010) showed this is the case previously for hydrodynamical turbulence – i.e., the forcing modes and the momentum modes cannot be treated analogously. For $P\nu = \infty$, we find

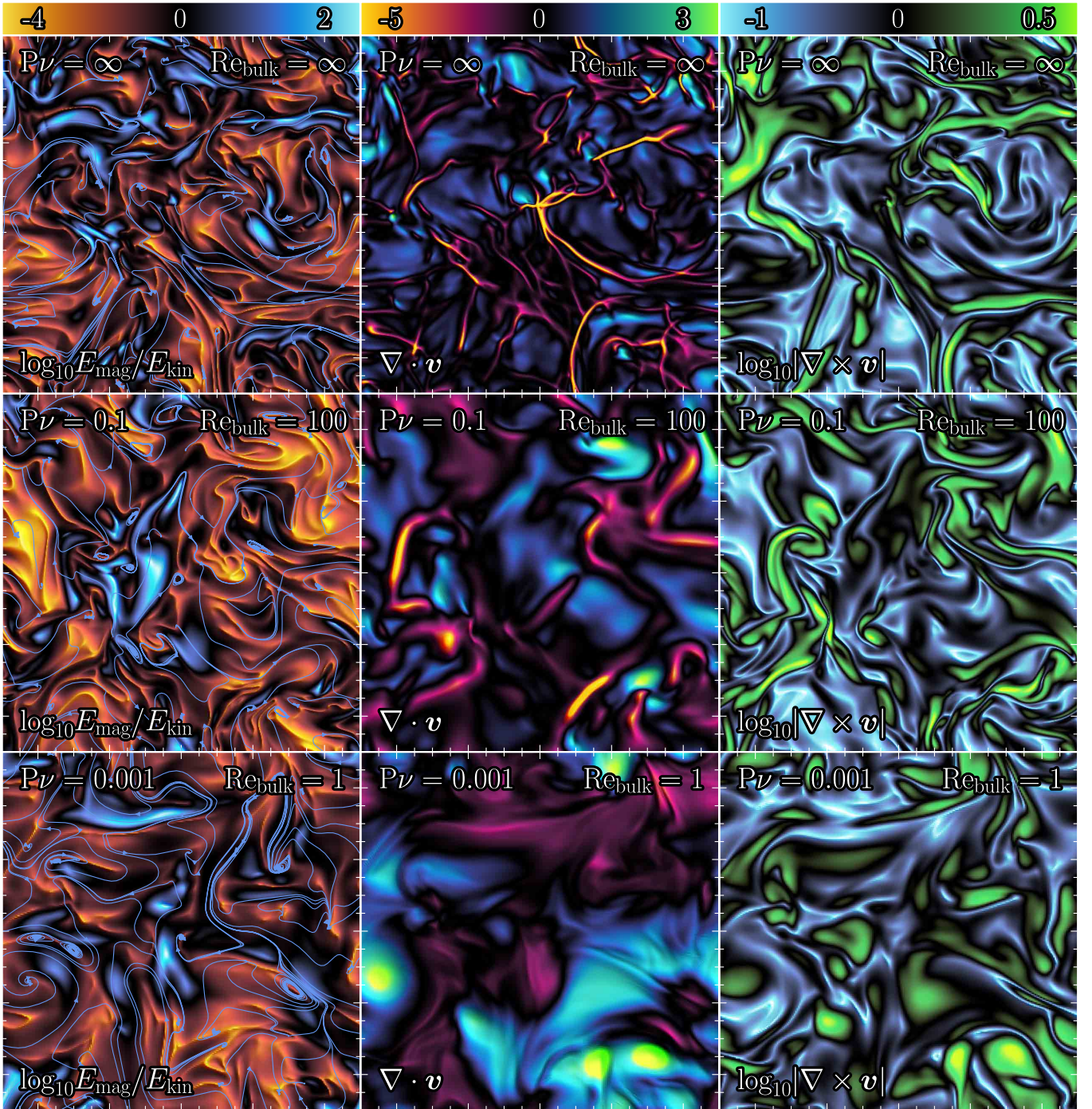


Figure 4. Two-dimensional slices in the kinematic stage of the dynamo ($t/t_0 = 30$) for $E_{\text{mag}}/E_{\text{kin}}$ (left column), $\nabla \cdot \mathbf{v}$ (middle column) and $|\nabla \times \mathbf{v}|$. Each of the quantities are normalised by the root-mean-squared value of the field to focus on the structure. The least viscous simulations are in the top row, where $P\nu = \infty$ and $\text{Re}_{\text{bulk}} = \infty$, and the dissipation of the compressible modes is controlled by the numerical viscosity (Malvadi Shivakumar & Federrath 2023). The most bulk viscous simulations are shown in the bottom row where $P\nu = 0.001$ (Equation 21) and $\text{Re}_{\text{bulk}} = 1$ (Equation 20). Magnetic field lines are shown in blue in the $E_{\text{mag}}/E_{\text{kin}}$ panels. The $\nabla \cdot \mathbf{v}$ panel show the strongest effect as the bulk viscous increases down the page. Thin shocks (yellow structures) in the $P\nu = \infty$ simulation (top row, middle column), become wider, diffusing away until they are completely absent in the $P\nu = 0.001$ simulation (bottom row, middle column). There is a lesser effect on the vorticity, which loses some of the small-scale structure as $P\nu$ gets smaller. A similar effect is shown for $E_{\text{mag}}/E_{\text{kin}}$ and the magnetic field structure that can be seen in the streamlines.

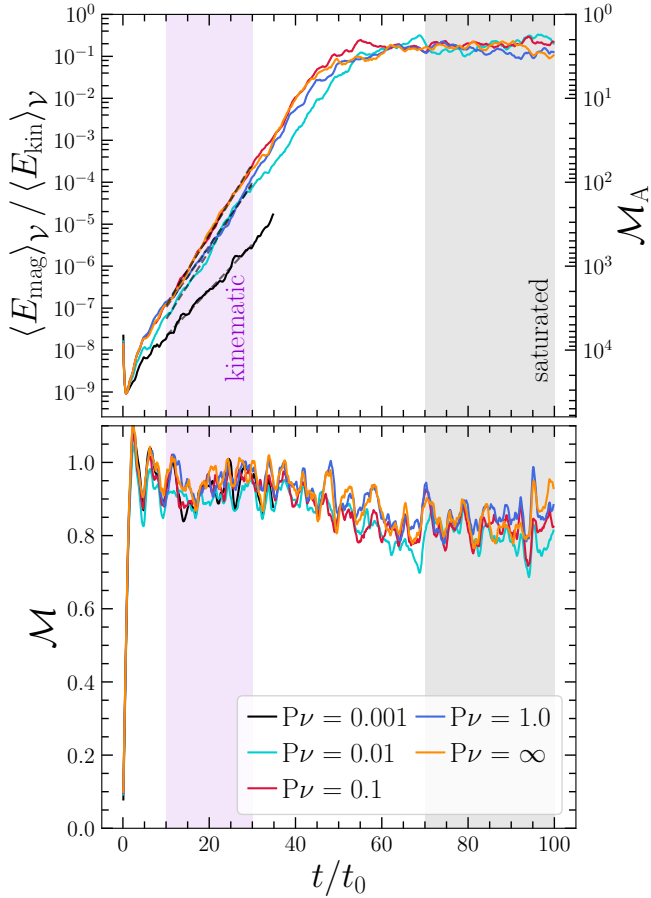


Figure 5. Top: the integral magnetic to kinetic energy ratio $\langle E_{\text{mag}} \rangle_{\nu} / \langle E_{\text{kin}} \rangle_{\nu}$ as a function of time in units of turbulent correlation times t/t_0 on the driving scale ℓ_0 , coloured by $P\nu$. The purple region indicates where we define the kinematic stage of the dynamo, $10 \leq t/t_0 \leq 30$, which we use for the entirety of our study. This is where $\langle E_{\text{mag}} \rangle_{\nu}$ exhibits exponential growth (Equation 1), which we fit an exponential model to shown with the black-dashed lines. We tabulate growth rates from these fits $2\gamma_1$ for each curve in Table 1. The grey region indicates the saturated stage of the dynamo (Equation 3). Similarly, we tabulate the $\langle E_{\text{mag}} \rangle_{\nu} / \langle E_{\text{kin}} \rangle_{\nu}$ ratios averaged over this region as well as the \mathcal{M}_A in Table 1. We find that for fixed Re_{shear} and Rm , moderate $P\nu$ ($\nu_{\text{bulk}} \sim \nu_{\text{shear}}$) does not have a strong influence on the growth rates or final $\langle E_{\text{mag}} \rangle_{\nu} / \langle E_{\text{kin}} \rangle_{\nu}$ saturation, however for low $P\nu$ ($\nu_{\text{bulk}} > \nu_{\text{shear}}$), the viscosity begins to have a strong, negative effect on both statistics. **Bottom:** The same as the top plot but for the \mathcal{M} evolution of the simulations, which moves between stationary states for the kinematic and saturated dynamo stages as the magnetic flux modifies the kinetic energy spectrum.

that $\langle E_{\text{kin},\parallel} \rangle_{\nu} / \langle E_{\text{kin}} \rangle_{\nu} \approx 10^{-1}$ (consistent with what has been measured previously in Federrath et al. 2011), down to $P\nu = 0.001$, where $\langle E_{\text{kin},\parallel} \rangle_{\nu} / \langle E_{\text{kin}} \rangle_{\nu} \approx 10^{-3}$, decreasing somewhat linearly with $P\nu$,

$$\langle E_{\text{kin},\parallel} \rangle_{\nu} / \langle E_{\text{kin}} \rangle_{\nu} \sim P\nu, \quad (51)$$

for $P\nu < 1$. This illustrates that as $P\nu$ shrinks there is a strong suppression of \mathbf{v}_{\parallel} modes, even for moderate $P\nu$, that we were not able to see before in Figure 5.

In the top panel of Figure 6 we show how the kinetic energy in these modes balance with the magnetic energy. As

we expect from the top panel of Figure 5, the final saturation of the \mathbf{v}_{\parallel} modes (dashed lines) is insensitive to the bulk viscosity, with $\langle E_{\text{mag}} \rangle_{\nu} / \langle E_{\text{kin},\parallel} \rangle_{\nu} \approx 0.1$ for all $P\nu$. However, the same is not true for the \mathbf{v}_{\perp} modes, which saturate to $1 \leq \langle E_{\text{mag}} \rangle_{\nu} / \langle E_{\text{kin},\perp} \rangle_{\nu} \leq 10$ (equipartition and beyond). Hence, the turbulence is sub-to-trans-Alfvénic with respect to \mathbf{v}_{\parallel} modes, which means that, for example, shocked gas will not be able to significantly change the morphology of the magnetic field due to the fact that $|\nabla \cdot (\mathbf{b} \otimes \mathbf{b}) + \nabla b^2| \gg |\nabla \cdot (\rho \mathbf{v}_{\parallel} \otimes \mathbf{v}_{\parallel})|$. This has been recently shown to be the case even in the kinematic stage of the supersonic dynamo (Kriel et al. 2025), but we find it happens here in a more extreme manner with decreasing $P\nu$, highlighting the importance of treating the \mathbf{v}_{\parallel} and \mathbf{v}_{\perp} modes separately in the supersonic dynamo problem.

5.2 Volume integrated growth terms

We compute the growth rate $2\gamma_1$ in units of t_0^{-1} by fitting a log-linear model in the dark violet region of the $\langle E_{\text{mag}} \rangle_{\nu} / \langle E_{\text{kin}} \rangle_{\nu}$ data, which we show in Figure 5. We show the fits with a grey dashed line. This corresponds to the kinematic stage of the dynamo, which we conservatively define with the range $10 \leq t/t_0 \leq 30$. We tabulate all of these values in Table 1, along with the \mathcal{M} averaged over the kinematic regime.

Similar to the $t \rightarrow \infty$ saturation, for moderate $P\nu$, γ_1 is quite insensitive to the bulk viscosity. The values range between $2\gamma_1 t_0 = 1.40 \pm 0.02 - 1.48 \pm 0.03$, i.e., every $1.4t_0$ (e -fold time), the field grows by $\approx e^n \langle E_{\text{mag},0} \rangle_{\nu}$, where n is the number of e -fold times. This suggests that the high- k compressible modes that are being decayed do not have a strong influence on small-scale shear viscous velocities, which are responsible for growing the magnetic field (Schekochihin et al. 2004c; Kriel et al. 2022; Galishnikova et al. 2022).

However, once the simulations become significantly bulk viscous, such that the decay time from our input ν_{bulk} becomes faster than the dynamical timescale on the turbulent outer-scale $t_{\nu_{\text{bulk}}} \sim (\ell_0^2 / \nu_{\text{bulk}})^{-1} \sim t_0$, which happens at $\text{Re}_{\text{bulk}} \leq 10$, $P\nu \leq 0.01$ at our \mathcal{M} , then γ_1 becomes significantly affected. It directly follows that it is the low- k compressible modes that affect the dynamo process, since the decay timescale has to become comparable to ℓ_0 to have an impact. The fact that there is an impact at all suggests that either ν_{bulk} plays a direct role in the exponential stage of the dynamo processes, directly by suppressing the growth processes, or that it plays an indirect role by coupling to viscous incompressible modes (as hypothesised in Toubert 2019), which are the modes responsible for growing the field in $\text{Pm}_{\text{shear}} \geq 1$ turbulent plasmas (e.g., Brandenburg et al. 1995; Schekochihin et al. 2004c; Federrath et al. 2011; Kriel et al. 2022, 2025). Curiously, this is the opposite of the effect that one observes when increasing \mathcal{M} , or enhancing the injection of compressibility in the forcing function (Federrath et al. 2011; Achikanath Chirakkara et al. 2021; Seta & Federrath 2021; Sur & Subramanian 2023; Kriel et al. 2025). We will show in Section 6.3 that we can explain this phenomena through $k_{\nu_{\text{bulk}}} - k_{\nu_{\text{shear}}}$ coupling, and that changing ν_{bulk} (modifying the high- k modes) and changing \mathcal{M} (modifying the low- k modes) is not equivalent, hence there is no tension with these previous studies. Now we turn to the growth terms derived in Section 3.

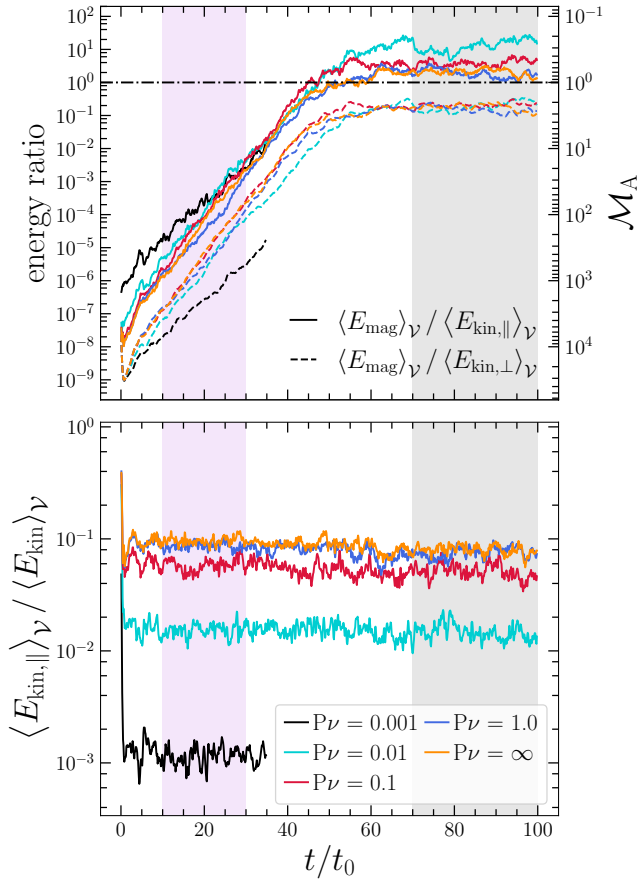


Figure 6. Top: the same as the top panel in Figure 5, but separated into incompressible (solid) and compressible (dashed) components of E_{kin} . The final saturated state for the incompressible modes is below equipartition $\langle E_{\text{kin},\parallel} \rangle_{\nu} / \langle E_{\text{mag}} \rangle_{\nu} < 1$, whereas it is significantly above equipartition for the compressible modes $\langle E_{\text{kin},\parallel} \rangle_{\nu} / \langle E_{\text{mag}} \rangle_{\nu} > 1$. **Bottom:** the integral compressible kinetic energy $\langle E_{\text{kin},\parallel} \rangle_{\nu}$ ratios with respect to the total kinetic energy $\langle E_{\text{kin}} \rangle_{\nu}$. We plot only $\langle E_{\text{kin},\parallel} \rangle_{\nu} / \langle E_{\text{kin}} \rangle_{\nu}$ because $\langle E_{\text{kin},\perp} \rangle_{\nu} / \langle E_{\text{kin}} \rangle_{\nu} \approx 1$ for all simulations. As $P\nu$ decreases, the total energy contained within the compressible component of the kinetic energy significantly decreases from $\langle E_{\text{kin},\parallel} \rangle_{\nu} / \langle E_{\text{kin}} \rangle_{\nu} \approx 10^{-1}$ to $\langle E_{\text{kin},\parallel} \rangle_{\nu} / \langle E_{\text{kin}} \rangle_{\nu} \approx 10^{-3}$, roughly following $\langle E_{\text{kin},\parallel} \rangle_{\nu} / \langle E_{\text{kin}} \rangle_{\nu} \sim P\nu$ for $P\nu < 1$.

In Figure 7 we plot the temporal probability distribution functions of each of the three volume-averaged growth terms in Equation 35, indicated by changing the line style of the distribution function. In the top plot, we show the distributions in the kinematic stage, and the bottom plot, the saturated stage, maintaining the same time window as we did in the previous section and shown in Figure 5. Furthermore, we show the complementary cumulative density function (CDFs),

$$\mathbb{P}(x > X) = 1 - \int_{-\infty}^X dx p(x), \quad (52)$$

for the $x = \langle (\mathbf{b} \otimes \mathbf{b}) : \mathbb{S} \rangle_{\nu} / \langle b^2 \rangle_{\nu}$ (top rows) and $x = \langle (\mathbf{b} \otimes \mathbf{b}) : (\nabla \cdot \mathbf{v}) \mathbb{I} \rangle_{\nu} / (6 \langle b^2 \rangle_{\nu})$ (bottom rows) for each simulation in the kinematic stage (left columns) and saturated stage (right columns) in Figure 8.

Let us begin in the kinematic stage, focusing on the top

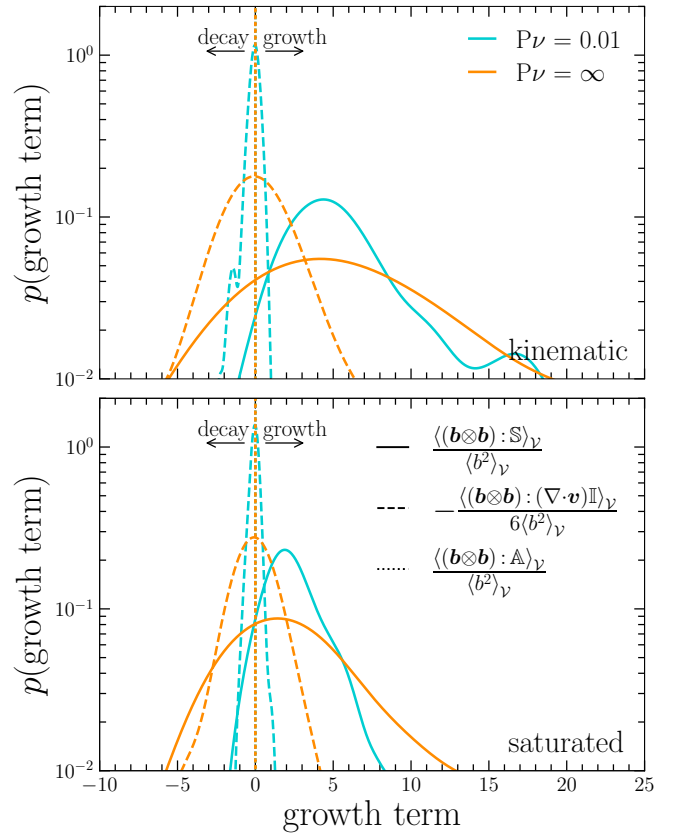


Figure 7. The temporal probability distribution functions of the stretching, winding and compression terms in the magnetic growth, Equation 35 (shown with different line styles), in the kinematic stage of the dynamo (top), and the saturated stage (bottom), coloured by $P\nu$, showing only the two $P\nu$ extremes ($P\nu = 0.001$ and $P\nu = \infty$). Each distribution function is constructed through kernel density estimation using a Gaussian function basis. For both stages, the winding term is zero (as predicted by Equation 36, i.e., the rate of rotation Equation 10, an antisymmetric tensor, is everywhere orthogonal to the magnetic field, a symmetric tensor). The growth rate is therefore an interplay between the compression term ($\langle (\mathbf{b} \otimes \mathbf{b}) : (\nabla \cdot \mathbf{v}) \mathbb{I} \rangle_{\nu} / (6 \langle b^2 \rangle_{\nu})$; dashed line style; which is suppressed for large bulk viscosities) and the stretching term ($\langle (\mathbf{b} \otimes \mathbf{b}) : \mathbb{S} \rangle_{\nu} / \langle b^2 \rangle_{\nu}$; solid line style). In both stages (kinematic and saturated) the stretching term is on average positive (net growth) and dominant over the compression. The compression approximately opposes and enhances growth in equal amounts, with a small tendency towards opposing growth, which is shown in more detail for all simulations in Figure 8.

panel of Figure 7. Firstly, both simulations show that the $\langle (\mathbf{b} \otimes \mathbf{b}) : \mathbb{A} \rangle_{\nu} / \langle b^2 \rangle_{\nu}$ distribution function (dotted line) is identically zero, as we predicted from Equation 36. This means that the tensors are on average orthogonal to one another. Because the contribution from the winding term is therefore zero, we ignore it for the remainder of the study and focus on the other two tensor projections.

The next largest contribution to the growth rate is $\langle (\mathbf{b} \otimes \mathbf{b}) : (\nabla \cdot \mathbf{v}) \mathbb{I} \rangle_{\nu} / (6 \langle b^2 \rangle_{\nu})$, which is almost symmetric about zero (but very slightly negatively skewed; all CDFs cross zero at $\mathbb{P} < 0.5$ in the bottom panel of Figure 8). This means, on average, in the kinematic stage, compressions make small, negative contributions to the growth rate at

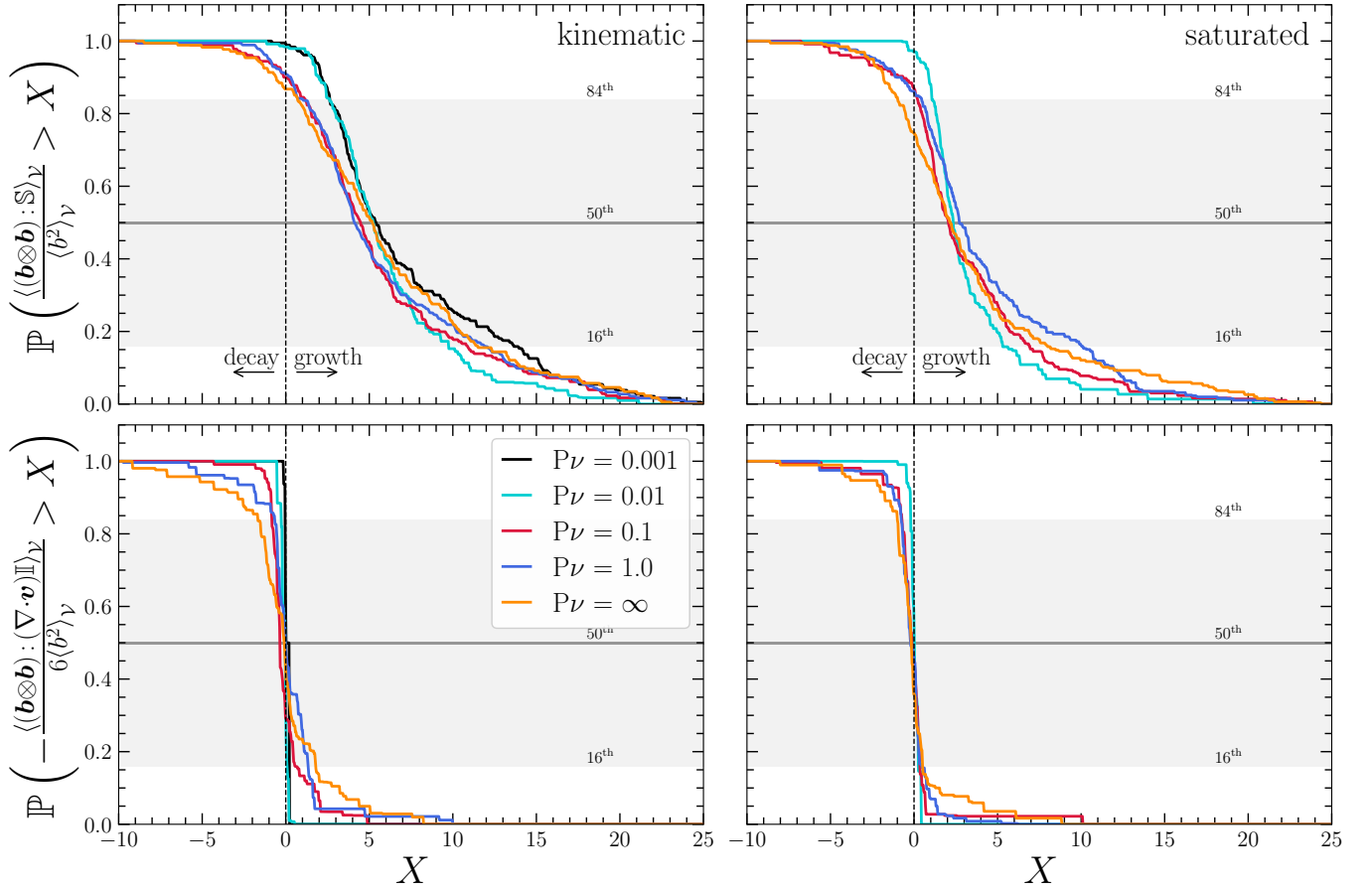


Figure 8. The complementary cumulative density functions Equation 52 for the stretching growth term $\langle(\mathbf{b} \otimes \mathbf{b}) : \mathbb{S}\rangle_V / \langle b^2 \rangle_V$; top panels) and the compression growth term $\langle(\mathbf{b} \otimes \mathbf{b}) : (\nabla \cdot \mathbf{v})\mathbb{I}\rangle_V / (6\langle b^2 \rangle_V)$; bottom panels), respectively, throughout the kinematic stage (left column) and saturated state (right column) of the dynamo, binned by the t/t_0 ranges in Figure 5. We use vertical, dashed, black lines to separate the values into growth and decay states, as we did in Figure 7, as well as adding horizontal lines to highlight the 16th, 50th and 84th percentiles of a standard Gaussian distribution function. We find that the stretching terms dominate the growth states, growing the field for all quantiles above the 16th percentile, while the compression terms are slightly more predisposed to decay states. Both growth terms contract at the onset of saturation (become closer to Heaviside functions), and the stretching term shifts towards $X = 0$ by a factor of ≈ 2 , recovering the result that growth terms are suppressed during the onset of saturation (e.g., Schekochihin et al. 2004b; Seta & Federrath 2021; Sur & Subramanian 2023).

our \mathcal{M} ⁷. However, temporal fluctuations, which are approximately Gaussian, ensure that the compressions make contributions to both growing the $\langle E_{\text{mag}} \rangle_V$ and decaying $\langle E_{\text{mag}} \rangle_V$ in approximately equal amounts. This highlights the dual role that compressible modes have in the dynamo problem – almost equally decaying and growing the field at $\mathcal{M} \approx 1$. As $P\nu$ gets smaller (and Re_{bulk} gets smaller), the fluctuations of the

compressions reduce (the CDFs become closer to Heaviside functions in Figure 8), but the time-average is maintained close to zero. This describes a process similar to what Chen et al. (2019) found for the effects of bulk viscosity on the spatial $\nabla \cdot \mathbf{v}$ distribution function – a somewhat symmetric contraction of the $\nabla \cdot \mathbf{v}$ distribution function that maintains the 1st moment. Hence, as the bulk viscosity increases, any fluctuations in the growth rate caused by either strong compression or rarefaction events diminish, but the average contribution of the compressions is maintained, hence the relatively weak dependence upon the growth rate for moderate Re_{bulk} . This is a key result from this analysis.

To understand why at very low Re_{bulk} we find that γ_1 changes quite dramatically, we turn our attention to the growth rate associated with stretching $\langle(\mathbf{b} \otimes \mathbf{b}) : \mathbb{S}\rangle_V / \langle b^2 \rangle_V$. Because the distribution function (solid line in Figure 7) is on average positive, the interaction between the magnetic field and the \mathbb{S} structures on average grow the field exponentially from Equation 30. As is evident in Figure 8, its

⁷ A natural hypothesis to explain the growth rates and $\langle E_{\text{mag}} \rangle_V / \langle E_{\text{kin}} \rangle_V$ saturation in Federrath et al. (2011) and more recently Sur & Subramanian (2023) and Kriel et al. (2025), at least from a mathematical perspective, is that changing \mathcal{M} shifts $\langle(\mathbf{b} \otimes \mathbf{b}) : (\nabla \cdot \mathbf{v})\mathbb{I}\rangle_V / (6\langle b^2 \rangle_V)$ towards more negative values due to the increasing skewness, $\langle(\nabla \cdot \mathbf{v})^3\rangle_V$, as the strongest, positive divergence structures becomes less and less space-filling, further inhibiting the growth and saturation, on average. In our study, we focus on a single \mathcal{M} and the effects of bulk viscosity, so we leave testing this hypothesis for future studies that utilise our decomposition.

not only the average, but as low as the 16th percentile of $\langle (\mathbf{b} \otimes \mathbf{b}) : \mathbb{S} \rangle_{\nu} / \langle b^2 \rangle_{\nu}$ that is able to grow the magnetic field. This is completely consistent with the key idea behind kinematic turbulent dynamo theories – stretching plays the dominant growth role in the kinematic stage of the dynamo (e.g., Moffatt & Saffman 1964; Haugen et al. 2004a; Zel’dovich et al. 1984; Brandenburg et al. 1995), which we show is even the case for the supersonic dynamo. This is why Kriel et al. (2025) was able to show numerically that the $k_{\eta}/k_{\nu_{\text{shear}}} \sim \text{Pm}_{\text{shear}}^{1/2}$ relation holds even in $\mathcal{M} > 1$ fluids.

Finally, we turn to the bottom panel of Figure 7 and the right column in Figure 8 to explore the differences between the kinematic and saturated stages of the dynamo under these tensorial decompositions. Compared to the kinematic stage, the $\langle (\mathbf{b} \otimes \mathbf{b}) : \mathbb{S} \rangle_{\nu} / \langle b^2 \rangle_{\nu}$ terms both shift on average, with the 50th percentiles moving towards zero, reducing by ≈ 2 across all $\text{P}\nu$, and contract, best shown in the bottom panel of Figure 7. The $\langle (\mathbf{b} \otimes \mathbf{b}) : (\nabla \cdot \mathbf{v}) \mathbb{I} \rangle_{\nu} / (6 \langle b^2 \rangle_{\nu})$ term similarly contracts in the saturated stage. Seta & Federrath (2021) found a similar trend, but their \mathcal{M} was significantly higher than ours and the difference between the saturated and kinematic stage statistics were not as significant (we find a reduction of roughly a factor of two in the 1st moments for $\langle (\mathbf{b} \otimes \mathbf{b}) : \mathbb{S} \rangle_{\nu} / \langle b^2 \rangle_{\nu}$). In their decomposition, at $\mathcal{M} = 3$, Sur & Subramanian (2023) also find a factor of ≈ 2 reduction in the 1st moments between the kinematic and the saturated stages. This highlights that our decomposition retains the well-known result that the growth terms are suppressed in the dynamo saturation.

6 KINETIC ENERGY SPECTRA

6.1 Total spectra

We plot the total kinetic energy spectra in the top panel of Figure 9, coloured in the same fashion as the previous plots. At low- k , all simulations have similar spectral energy contained on those scales, which flattens under a $E_{\text{kin}}(k) \sim k^{-2}$ Burgers (1948) scaling as shown in the inset panel, as expected for supersonic turbulence dominated by singularities (Federrath 2013; Verma 2017; Federrath et al. 2021; Kriel et al. 2025). However, as expected for a viscosity-like process (a process that is scale-separated from the large-scales and starts by influencing the small-scale dynamics), there is a significant difference between simulations in the high- k modes. Because 2nd moments have integrals dominated by low- k modes (Beattie et al. 2022a), this highlights why the $\langle E_{\text{mag}} \rangle_{\nu} / \langle E_{\text{kin}} \rangle_{\nu}$ did not have a strong impact from the bulk viscosity in Section 5.

For both the $\text{P}\nu = 1.0$ and $\text{P}\nu = \infty$ simulation, we observe an excess amount of power piling up at high- k , which could be qualitatively described as a bottleneck effect. This is what we would call the sub-shear-viscous range Equation 29, which ought to appear when $\text{P}\nu > 1$, as in the right panel of Figure 1. However, as $\text{P}\nu$ decreases to ≤ 0.1 , the sub-shear-viscous range and bottleneck completely disappear and we are left with a smooth, rather featureless decay into dissipatively-dominated, low-power Fourier energy modes, as expected from the left panel of Figure 1. That is, once the bulk viscosity is large enough (Re_{bulk} and $\text{P}\nu$ are low enough, which ought to be $\text{P}\nu \approx 1/3$ based on our definition; see foot-

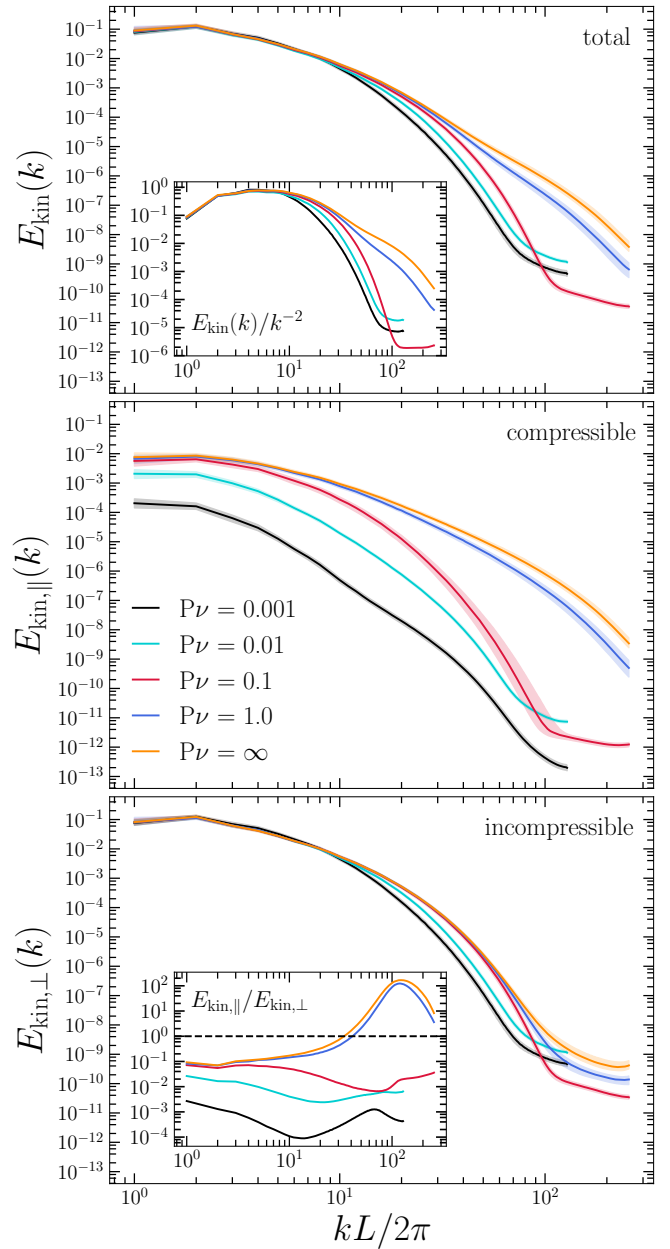


Figure 9. The shell-integrated kinetic energy spectra averaged over the kinematic stage of the dynamo. **Top:** The total kinetic energy spectrum, coloured by $\text{P}\nu$, averaged over the kinematic regime (see Figure 5), with inset showing flattening of the spectra under the Burgers (1948) scaling, $E_{\text{kin}}(k) \sim k^{-2}$. The bulk viscosity acts to suppress the high- k mode structure in the total energy, suggestive that compressible modes occupy significant energies on the smallest scales, contributing to a bottleneck effect. **Middle:** The compressible (longitudinal) kinetic energy spectrum, demonstrating that for $\text{P}\nu > 1$, the dissipation in the compressible modes is not resolved or controlled. **Bottom:** The incompressible (transverse) kinetic energy spectrum with the ratio of the $E_{\text{kin},||}(k)$ and $E_{\text{kin},\perp}(k)$ in the inset. For fixed Re_{shear} , reducing $\text{P}\nu$ suppresses the high- k compressible modes, acting more strongly on the compressible spectrum for lower $\text{P}\nu$. The incompressible spectrum is also influenced, with much less of an effect, with coupling starting deep in the viscous scales, but slowly moving to lower k modes as the decay timescale, $t_{\nu_{\text{bulk}}}$, becomes shorter.

note 5), the physical dissipation of them allows them to be removed faster than they are able to move down the cascade (which is fast $E_{\text{kin}}(k) \sim k^{-2}$; Seta & Federrath 2021; Federrath 2013; Federrath et al. 2021; Kriel et al. 2025), and hence the bottleneck and sub-shear-viscous range is destroyed.

6.2 Helmholtz decomposed spectra

As we did with the integral statistics, to truly observe the $P\nu$ effect on the plasma we plot the Helmholtz decomposed spectra in the middle (compressible) and bottom (incompressible) panels in Figure 9, also showing the ratio between the two spectra in the inset in the bottom panel. Confirming what we discussed in the previous section, for $P\nu > 1$, $E_{\text{kin},\parallel}(k)/E_{\text{kin},\perp}(k)$ varies from $E_{\text{kin},\parallel}(k)/E_{\text{kin},\perp}(k) \approx 10^{-1}$ on large-scales, to $E_{\text{kin},\parallel}(k)/E_{\text{kin},\perp}(k) \approx 10^2$ on small-scales, highlighting how energised the compressible modes become in the sub-shear-viscous range when $P\nu$ is large. Once $P\nu < 1$, the apparent bottleneck and sub-shear-viscous range disappear, and $E_{\text{kin},\parallel}(k)/E_{\text{kin},\perp}(k)$ becomes relatively scale invariant, with some systematic shallowing from large to small scales, indicating a faster cascade in the compressible modes. Now we turn to the individual $E_{\text{kin},\parallel}(k)$ and $E_{\text{kin},\perp}(k)$ spectra.

As expected, the $E_{\text{kin},\parallel}(k)$ spectrum (middle panel of Figure 9) is strongly influenced by $P\nu$, with the dissipative effects beginning at high- k and moving towards low- k as the $P\nu$ decreases. This is expected since $\nu_{\text{bulk}} \nabla \cdot (\nabla \cdot \mathbf{v}) \mathbb{I} = \nu_{\text{bulk}} \nabla \cdot (\nabla \cdot \mathbf{v}_{\parallel}) \mathbb{I} = \nu_{\text{bulk}} \nabla^2 \mathbf{v}_{\parallel}$ ends up having the local properties of a Laplacian operator on the \mathbf{v}_{\parallel} modes in the momentum flux. As discussed in Section 3.2, in the lowest $P\nu$, where $t_{\nu_{\text{bulk}}} \sim t_0$, the low- k modes are significantly suppressed by roughly 10^2 in total power compared to the $P\nu = \infty$ simulation. Because these are the simulations that actually modify the growth and saturation (see Figure 5 and Figure 6), it is clear that as we hypothesised earlier, it is predominately the low- k compressible modes that change the characteristics of the dynamo, in stark contrast with the high- k incompressible modes that are responsible for all of the dynamo action via $\nu_{\text{shear}}/\ell_{\nu_{\text{shear}}}$ stretching.

In Figure 7 and Figure 8, we saw that the 2nd moments of both the shear and compression growth terms, Equation 35, contracted and the CDFs steepened under the impact of the bulk viscosity. We hypothesised that this may be due to the correlation between compressible and incompressible modes. We now see another signature of mode correlation via $E_{\text{kin},\perp}(k)$ (bottom panel of Figure 9), where a Laplacian-like viscosity (starting at high- k) encroaches upon the spectra, and more strongly as $P\nu$ decreases. This corresponds to a growing sub-bulk-viscous range of k , as we illustrated in Figure 1. It is suggestive that in this $P\nu < 1$ regime $k_{\nu_{\text{shear}}} \sim k_{\nu_{\text{bulk}}}$, and⁸ that the most viscous $\mathbf{v}_{\parallel}(k)$ and $\mathbf{v}_{\perp}(k)$ modes are becoming increasingly coupled as the sub-bulk-viscous range increases in size. This is similar to the results found in two dimensions in Touber (2019), where they found that in the viscous limit bulk viscosity would suppress vor-

ticity production. We explore this correlation in more detail in the following section.

6.3 The coupling of incompressible and compressible modes

6.3.1 Measuring mode coupling

There are a number of different probes for measuring mode coupling. For example, the bispectrum measures the coupling of the mode phases (Burkhart et al. 2009; Burkhart 2021) and the turbulence transfer functions measure the energy flux (or any kind of flux) moving between different modes (e.g., Mininni et al. 2005; Grete et al. 2017; Schmidt & Grete 2019; Grete et al. 2020; Squire et al. 2023). We choose a simple measure to probe the linear coupling between the Fourier amplitudes, namely the cross-correlation \mathcal{C} between each wave mode pair, (k, k') , across the time-evolving $E_{\text{kin},\parallel}(k, t)$ and $E_{\text{kin},\perp}(k, t)$ spectra. We define it,

$$\mathcal{C}(k, k', t') = \int_{-\infty}^{\infty} dt \overline{E_{\text{kin},\perp}(k, t)} \overline{E_{\text{kin},\parallel}(k', t')}, \quad (53)$$

where $t' = t + \Delta t$ such that Δt is an arbitrary time lag, and the overline indicates a transform of

$$\overline{X} = \frac{X - \langle X \rangle_{t/t_0}}{\langle X \rangle_{t/t_0}^2 - \langle X^2 \rangle_{t/t_0}}, \quad (54)$$

to normalise each k mode by both the mean energy (a function of where the k modes exists in the cascade) and the size-scale of the temporal fluctuations, which we may change by orders of magnitude between each of the spectra ($E_{\text{kin},\parallel}(k)$ temporal intermittency need not be the same as $E_{\text{kin},\perp}(k)$ temporal intermittency), as demonstrated by comparing the 1σ bands for the spectra in Figure 9.

We plot the $\mathcal{C}(k, k', \underline{t}')$ surfaces for $P\nu = \infty$ (top panel), $P\nu = 0.1$ (middle panel) and $P\nu = 0.001$ (bottom panel) in Figure 10, showing only \underline{t}' that maximises the $|\mathcal{C}(k, k', \underline{t}')|$ function, \underline{t}' , i.e., maximises the strength of the mode coupling. In general, across the viscous modes we find that $\underline{t}' = 0$ maximises the correlation, which is a repercussion of the parabolic, non-causal diffusion operators. Here k on the y axis corresponds to $E_{\text{kin},\perp}(k)$ modes, and k' on the x axis corresponds to $E_{\text{kin},\parallel}(k)$ modes, as indicated by Equation 53.

Firstly, a generic feature for all simulations is that the lowest k modes have the weakest coupling with all other modes in the simulations. These are, of course, the driving modes, where we inject Gaussian increments into turbulence that are correlated in time. These modes are the most orthogonal, in the sense that the fluctuations there are not strongly coupled on large-scales. However, as we move to higher- k modes, we begin to see stronger correlations develop, which we highlight with the red quadrilaterals over the most strongly correlated modes. Let us now explore why this is the case.

6.3.2 Viscously coupled modes

The strongest correlations are at the highest- k modes, where the plasma is dominated by both types of viscosities (yellow regions in Figure 10, highlighted with red rectangles), i.e., in the expanding sub-bulk-viscous range, as illustrated in Figure 1. This region starts small, but as $P\nu$ decreases, more and more v_{\perp} modes become coupled with the v_{\parallel} models, until at $P\nu = 0.001$, the correlation is strong and persistent up to

⁸ In that $k_{\nu_{\text{shear}}}$ depends upon $k_{\nu_{\text{bulk}}}$, and the dependence does not need to be linear. However, we leave the determination of such relations for future works.

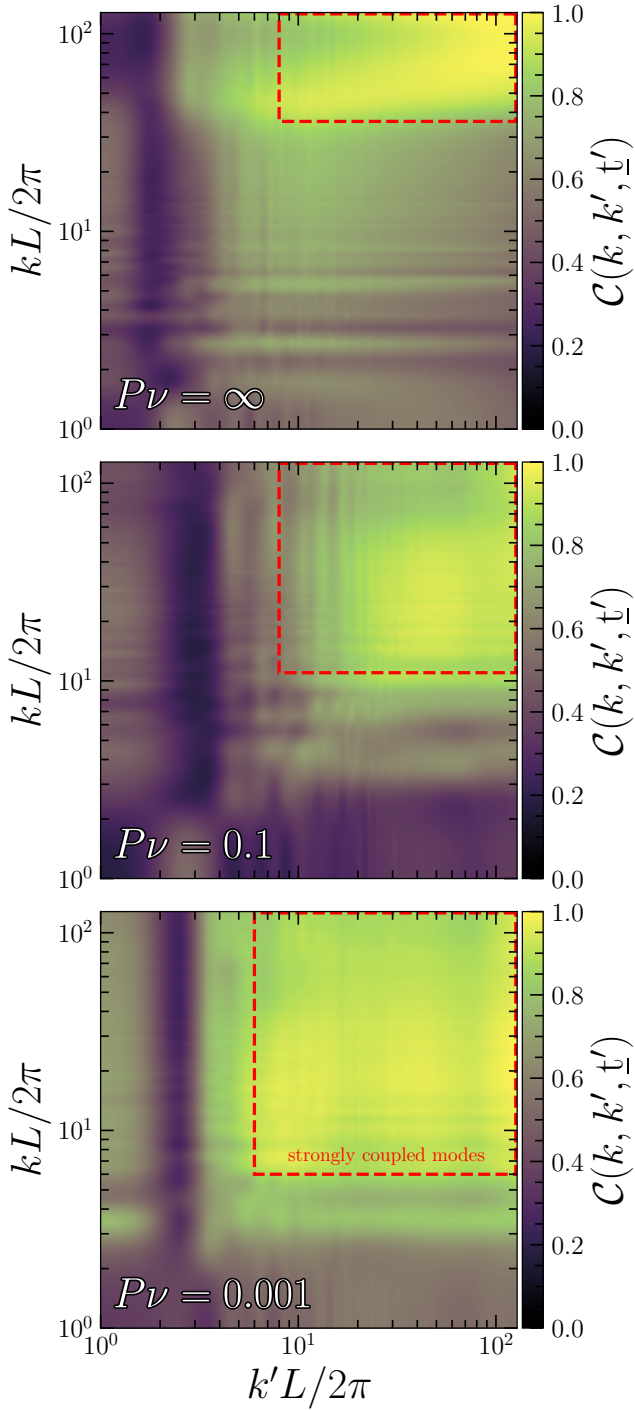


Figure 10. The cross correlation function $C(k, k', t')$ given by Equation 53, between the incompressible $E_{\text{kin},\perp}(k)$ modes and the compressible $E_{\text{kin},\parallel}(k')$ modes, shown at $t' = \underline{t}'$, where \underline{t}' is the lag that maximises the magnitude of the correlation function, i.e., the maximum linear mode coupling. Each panel shows a different simulation, as annotated in the panel, where $P\nu = \infty$ (top panel) has no bulk viscosity, $P\nu = 0.1$ (middle panel) has enough bulk viscosity to \sim balance the shear viscosity and $P\nu = 0.001$ is dominated by bulk viscosity ($\text{Re}_{\text{bulk}} = 1$). We show the regions of strong correlation with the red, dashed rectangles, highlighting that as the bulk viscosity increases, the incompressible modes become increasingly coupled within the expanding sub-bulk-viscous range (see Figure 1).

$k \lesssim 10$, consistent with the shallowing incompressible spectrum in Figure 9. Let us consider what form this coupling may take in the kinetic energy equations.

In the Stokes regime, where $\text{Re}_{\text{shear}} \sim \text{Re}_{\text{bulk}} \rightarrow 0$, relevant to the most dissipative k modes in Figure 9, we can construct the dimensionless (following Section 2.2) 1st moment kinetic energy evolution equation for each of the modes, noting that $\mathbf{v}_{\parallel} \cdot \mathbf{v} = \mathbf{v}_{\parallel} \cdot (\mathbf{v}_{\parallel} + \mathbf{v}_{\perp}) = \mathbf{v}_{\parallel} \cdot \mathbf{v}_{\parallel} + \mathbf{v}_{\parallel} \cdot \mathbf{v}_{\perp} = v_{\parallel}^2$, by construction, and similarly $\mathbf{v}_{\perp} \cdot \mathbf{v} = v_{\perp}^2$. They are,

$$\frac{\partial \langle E_{\text{kin},\perp} \rangle_{\mathcal{V}}}{\partial t} = \overbrace{\text{Re}_{\text{shear}}^{-1} \langle \mathbf{v}_{\perp} \cdot \nabla^2 \mathbf{v}_{\perp} \rangle_{\mathcal{V}}}^{\text{incomp. viscosity}} + \underbrace{\left(\frac{4\text{Re}_{\text{shear}}^{-1}}{3} + \text{Re}_{\text{bulk}}^{-1} \right) \langle \mathbf{v}_{\perp} \cdot \nabla^2 \mathbf{v}_{\parallel} \rangle_{\mathcal{V}}}_{\text{comp. mode \& incomp. viscosity coupling}}, \quad (55)$$

$$\frac{\partial \langle E_{\text{kin},\parallel} \rangle_{\mathcal{V}}}{\partial t} = \overbrace{\text{Re}_{\text{shear}}^{-1} \langle \mathbf{v}_{\parallel} \cdot \nabla^2 \mathbf{v}_{\perp} \rangle_{\mathcal{V}}}^{\text{comp. mode \& incomp. viscosity coupling}} + \underbrace{\left(\frac{4\text{Re}_{\text{shear}}^{-1}}{3} + \text{Re}_{\text{bulk}}^{-1} \right) \langle \mathbf{v}_{\parallel} \cdot \nabla^2 \mathbf{v}_{\parallel} \rangle_{\mathcal{V}}}_{\text{shear enhanced bulk viscosity}}, \quad (56)$$

similar to Equations 4.15-4.16 in Wang et al. (2018b) but we have expanded the viscous term $\langle D \rangle_{\mathcal{V}}$ and included bulk viscosity. Hence, not only do both energy equations support Laplacian-like dissipation operators for each of the modes projected onto either the compressible or incompressible velocity, but through the definition of the bulk viscosity (see footnote 5), the $\nabla^2 \mathbf{v}_{\parallel}$ terms are also scaled by $\text{Re}_{\text{shear}}^{-1}$. Through both the projections, and the mixing of Reynolds numbers, clearly within the Stokes regime (corresponding to the sub-bulk-viscous range of scales) the modes become coupled.

Because we are keeping Re_{shear} constant, and we are interested in the correlations from the compressible modes in the Equation 55, we are able to determine that the correlation of interest is the second term of Equation 55. The strength of this term relative to the regular incompressible diffusion. It is

$$\frac{\left(\frac{4}{3} \text{Re}_{\text{shear}}^{-1} + \text{Re}_{\text{bulk}}^{-1} \right) \langle \mathbf{v}_{\perp} \cdot \nabla^2 \mathbf{v}_{\parallel} \rangle_{\mathcal{V}}}{\text{Re}_{\text{shear}}^{-1} \langle \mathbf{v}_{\perp} \cdot \nabla^2 \mathbf{v}_{\perp} \rangle_{\mathcal{V}}} = \left(\frac{4}{3} + \frac{1}{P\nu} \right) \frac{\langle \mathbf{v}_{\perp} \cdot \nabla^2 \mathbf{v}_{\parallel} \rangle_{\mathcal{V}}}{\langle \mathbf{v}_{\perp} \cdot \nabla^2 \mathbf{v}_{\perp} \rangle_{\mathcal{V}}} \sim \frac{1}{P\nu}, \quad (57)$$

which shows that the strength of the coupling relative to the incompressible diffusion scales with $P\nu^{-1}$. hence, as we show in Figure 10, the viscous mode coupling increases with decreasing $P\nu$, which is the key result from this section.

6.3.3 Coupling in the cascade

In principle, $\nabla \cdot (\rho \mathbf{v} \otimes \mathbf{v})$ will provide further correlations in the cascade, since $\nabla \cdot (\rho \mathbf{v} \otimes \mathbf{v}) = \nabla \cdot (\rho [\mathbf{v}_{\parallel} + \mathbf{v}_{\perp}] \otimes [\mathbf{v}_{\parallel} + \mathbf{v}_{\perp}])$ has interaction terms in the cascade $\sim \nabla \cdot (\rho \mathbf{v}_{\parallel} \otimes \mathbf{v}_{\perp} + \rho \mathbf{v}_{\perp} \otimes \mathbf{v}_{\parallel})$ which facilitate the conversion of compressible mode momentum flux into incompressible modes $\nabla \cdot (\rho \mathbf{v}_{\parallel} \otimes \mathbf{v}_{\perp})$, and vice versa $\nabla \cdot (\rho \mathbf{v}_{\perp} \otimes \mathbf{v}_{\parallel})$. However, our simulations do not

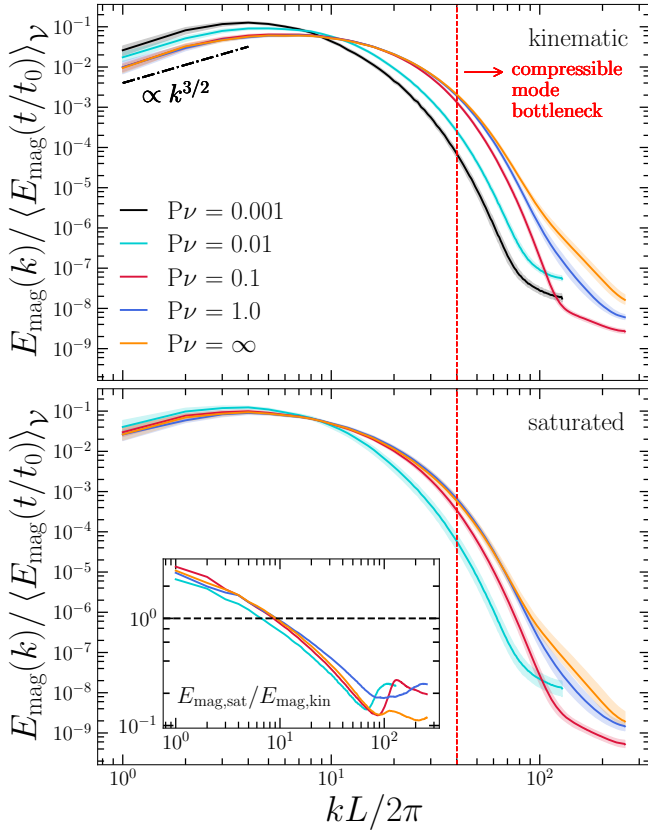


Figure 11. The same as Figure 9, but for the magnetic energy spectrum normalised by time-dependent integral magnetic energy. **Top:** The normalised magnetic energy spectra shown in the kinematic stage of the dynamo. We show the Kazantsev (1968) $E_{\text{mag}}(k) \sim k^{3/2}$ power law in the top panel, which all simulations, regardless of $P\nu$, exhibit up until the peak of the energy spectra. **Bottom:** The same as the top panel but for the saturated stage of the dynamo. In the inset panel we show the ratio between the normalised saturated and kinematic magnetic field spectra, highlighting the different spectral distributions of energy in each of the regimes (more large-scale in the saturated stage, and vice-versa in the kinematic stage). With a red dashed, vertical line, we show the extent of the apparent compressible mode bottleneck (the sub-shear-viscous range) from the inset in Figure 9 (only present in simulations with $P\nu > 0.1$). This shows that the suppression of the bottleneck and the sub-shear-viscous range through the bulk viscosity results in a suppression of high- k modes in $E_{\text{mag}}(k)$.

have a particularly extended cascade, with $\text{Re}_{\text{shear}} = 1000$, and $\ell_0 \sim \text{Re}_{\text{shear}}^{2/3} \ell_{\nu\text{shear}} \sim 0.1(1000)^{2/3} \ell_{\nu\text{shear}}$, only supporting a factor ~ 10 separation⁹ between ℓ_0 and $\ell_{\nu\text{shear}}$. This means $2 \lesssim k \lesssim 20$ is approximately where the cascade should be, noting that there can be contamination from the driving modes over a much larger bandwidth than just exactly where the energy is being injected (Federrath et al. 2021; Grete et al. 2023). We therefore are unable to probe the coupling within

⁹ Proportionality constant from Figure 6 in Kriel et al. (2025) and the $\text{Re}_{\text{shear}}^{2/3}$ relation is for Burgers (1948) turbulence with $E_{\text{kin}}(k) \sim k^{-2}$ (Schober et al. 2012), which surprisingly works for the total spectrum and not just the decomposed spectrum, as shown in Kriel et al. (2025).

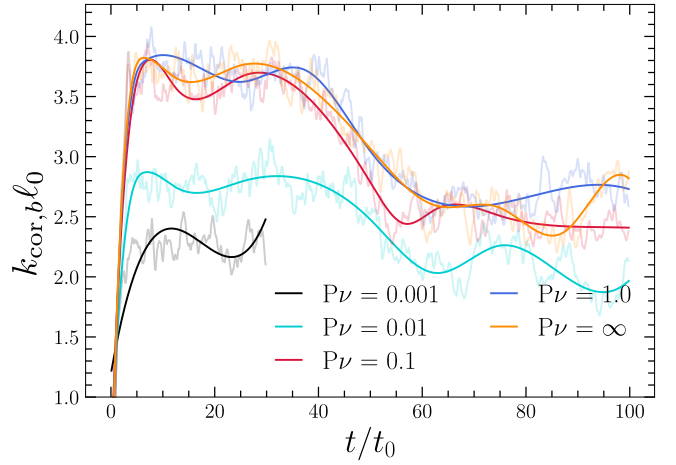


Figure 12. The integral scale of the magnetic field $k_{\text{cor},b}$ in units of the driving scale ℓ_0 , coloured by $P\nu$. As has been shown before, the kinematic stage of the dynamo quickly builds a small-scale field ($k_{\text{cor},b}\ell_0 > 1$), likely through magnetic field-folding, which is present in both $\mathcal{M} < 1$ and $\mathcal{M} > 1$ dynamos (Schekochihin et al. 2004c; Kriel et al. 2025). However, as the nonlinear stage approaches $\sim 20t_0$ the integral scale shifts to lower modes (larger scales) before becoming stationary again at those larger scales in the saturated stage. The effect of the bulk viscosity suppresses the small-scale field in the kinematic stage of the dynamo, by correlating to the viscous solenoidal modes $k \sim k_{\nu\text{shear}}$ responsible for growing the magnetic field.

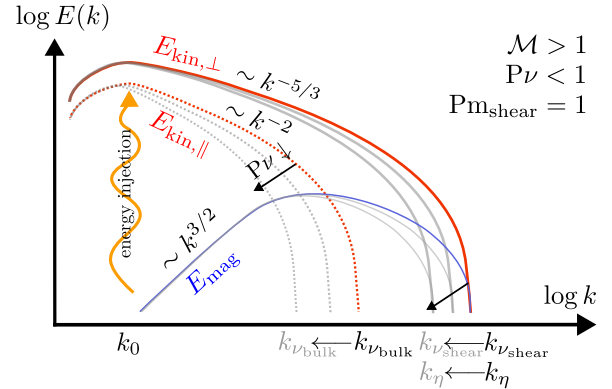


Figure 13. The same as the left panel of the spectrum schematic in Figure 1, but showing that in the $P\nu < 1$ regime, as $P\nu$ decreases, $k_{\nu\text{bulk}}$ shifts to lower k modes, and through the viscosity correlations in the sub-bulk-viscous range, $k_{\nu\text{bulk}}$ drags $k_{\nu\text{shear}}$ with it, which then shifts k_η , since k_η is depends upon the exact placement of $k_{\nu\text{shear}}$, $k_\eta \sim \text{Pm}_{\text{shear}}^{1/2} k_{\nu\text{shear}}$ (for latest numerical confirmation, see, e.g., Kriel et al. 2022, 2025).

the cascade (or even the cascade exponents themselves), in detail, with our simulations. However, we can see faint stripes through $2 \lesssim k \lesssim 20$ in both $P\nu = \infty$ and $P\nu = 0.1$ simulations, where weakly-correlated, non-local fluctuations move across both the incompressible k and compressible k' modes.

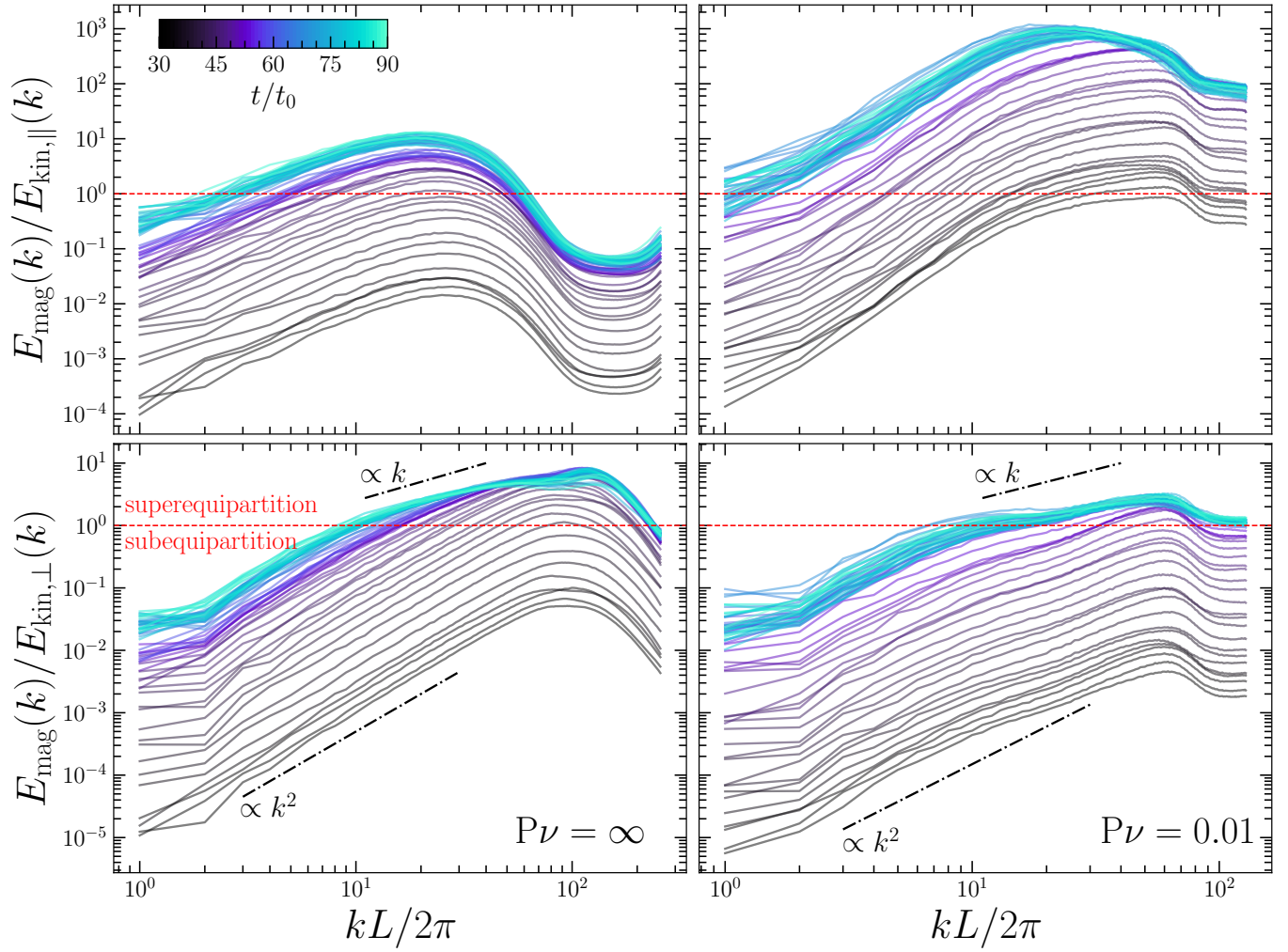


Figure 14. The magnetic $E_{\text{mag}}(k)$, compressible ($E_{\text{kin},\parallel}(k)$; top) and incompressible ($E_{\text{kin},\perp}(k)$; bottom) kinetic energy ratios as a function of k for $P\nu = \infty$ (no bulk viscosity; left column) and $P\nu = 0.01$ (strong bulk viscosity; right column), coloured by t/t_0 (indicated in the top left panel). We start at $t/t_0 = 30$, at the end of the kinematic stage (black), and evolve to $t/t_0 = 90$, well within the saturated stage (aqua; see Figure 5 for how t/t_0 corresponds to the different stages). Each panel has the equipartition $E_{\text{mag}}(k) = E_{\text{kin}}(k)$ drawn in red. **Compressible modes (top row):** for $P\nu = \infty$, the saturated state for the compressible modes is in subequipartition ($E_{\text{mag}}(k)/E_{\text{kin},\parallel}(k) < 1$) at low and high- k . The high- k mode subequipartition energy is associated with the sub-shear-viscous range, outlined in Figure 1. However, for $P\nu = 0.01$, the sub-shear-viscous range is destroyed through the bulk viscosity, and only the low- k modes are left in subequipartition, meaning that all but the lowest compressible k modes ought to be dominated by the effects of the magnetic field. **Incompressible modes (bottom row):** during the kinematic stage, $E_{\text{mag}}(k) \sim k^2 E_{\text{kin},\perp}(k)$ up to the peak scale of the spectral energy ratio, previously shown in Beattie et al. (2023). As the dynamo saturates, the energy ratio flattens to roughly $E_{\text{mag}}(k) \sim k E_{\text{kin},\perp}(k)$ for superequipartition k modes ($E_{\text{mag}}(k)/E_{\text{kin},\perp}(k) < 1$), potentially due in part to $\nabla \cdot (\mathbf{b} \otimes \mathbf{b})$ suppressing the field-line stretching term in Equation 35.

7 MAGNETIC ENERGY SPECTRA

We plot the magnetic spectra normalised by the integral, and averaged over time, in Figure 11, showing the kinematic stage spectra in the top panel, and the saturated spectra in the bottom panel, along with the ratio between the spectra in the inset plot. Firstly, it is apparent that the magnetic fields for the low $P\nu$ simulations are becoming more large-scale (high- k modes are being suppressed), during both the kinematic stage, where they follow the Kazantsev (1968) $k^{3/2}$ power law, and in the saturated stage. We can quantify this more precisely by computing the magnetic integral (or correlation)

scale. For $E_{\text{mag}}(k)$, it is

$$k_{\text{cor},b}\ell_0 = \frac{L}{2} \left(\frac{\int dk k^{-1} E_{\text{mag}}(k)}{\int dk E_{\text{mag}}(k)} \right)^{-1}, \quad (58)$$

which we compute for each time realisation, for each of our simulations, and plot across time in Figure 12, fitting cubic splines to the data to extract the general low-frequency trends. We see the well-established trend that the field is small-scale ($k_{\text{cor},b}\ell_0 < 1$) in the kinematic stage, before becoming correlated on large-scales, reducing $k_{\text{cor},b}\ell_0$ through the nonlinear and finally settling on $k_{\text{cor},b}\ell_0 \approx 2.5$ in the saturated stage (Schekochihin et al. 2004c; Rincon 2019; Seta

& Federrath 2021; Galishnikova et al. 2022; Beattie et al. 2023). The energy redistribution can be seen on a mode-by-mode basis in the inset plot in the bottom panel of Figure 11, where there is now a factor of ≈ 2 more energy concentrated at low- k , and an order of magnitude less at high- k . For $P\nu < 1$, the magnetic fields lose energy on high- k , potentially through the suppression of the sub-shear-viscous modes and compressible mode bottleneck, which could in principle grow the field through compressions, but these will be highly-inefficient since flux freezing will be violated strongly on these scales (resistivity becomes comparable to induction at high- k), at least in our simulations where a sub-shear-viscous range is generated. We annotate the rough extent of this range with red in Figure 11. Furthermore, as expected from Figure 11, we find that for $P\nu < 0.01$, where we know the compressible/incompressible mode coupling is strong, the correlation scales are pushed closer to ℓ_0 . This could be simply because $\ell_{\nu_{\text{shear}}}$ shifts to lower k modes through the coupling, which in turn reorganises the magnetic field for a fixed Pm_{shear} , since $k_\eta/k_{\nu_{\text{shear}}} \sim \text{Pm}_{\text{shear}}^{1/2}$ (Schekochihin et al. 2002c; Kriel et al. 2022, 2025), and as we have discussed in Section 6.2, $k_{\nu_{\text{shear}}} \sim k_{\nu_{\text{bulk}}}$ for low Re_{bulk} . The key takeaway is that the bulk viscosity suppresses magnetic energy in the high- k modes due to the suppression of the sub-shear-viscous range through direct correlations between $k_{\nu_{\text{shear}}}$ and $k_{\nu_{\text{bulk}}}$ (shown in Section 6.3), in both the stages of the dynamo. We annotate how this may work in Figure 13, where we show $k_{\nu_{\text{bulk}}}$ shifting to lower k modes, which in turn moves $k_{\nu_{\text{shear}}}$, shifting k_η , destroying the high- k magnetic modes (Kriel et al. 2025). The net effect of this process is that magnetic fields are significantly more large-scale than the pure shear-viscous dynamo counterparts.

8 SPECTRAL RATIO FUNCTIONS

The final statistic we use to probe the role of bulk viscosity in the compressible turbulent dynamo are the ratios between the magnetic and compressible and incompressible kinetic energies as a function of time, Figure 14, revealing scale-by-scale information about the transition between the stages of the dynamo (see Section 1), as previously done in Beattie et al. (2023). To further build upon Beattie et al. (2023), we split the saturation into compressible $E_{\text{kin},\parallel}(k)/E_{\text{mag}}(k)$ (top panels) and incompressible $E_{\text{kin},\perp}(k)/E_{\text{mag}}(k)$ (bottom panels), with the columns organised by $P\nu$, with $P\nu = \infty$ (left) and $P\nu = 0.01$ (right). We take the spectral ratios from $t/t_0 = 30$, which is within the kinematic stage, to $t/t_0 = 90$, which is well and truly saturated (see Figure 5). The intermediate purple stage is within the nonlinear, transition stage between the kinematic and saturation. We draw a dashed, red line at equipartition, $E_{\text{kin}}(k)/E_{\text{mag}}(k) = 1$, which defines an energy equipartition scale, k_{eq} such that $E_{\text{kin}}(k_{\text{eq}})/E_{\text{mag}}(k_{\text{eq}}) = 1$, which has gone by a number of names in the literature, e.g., tearing scale (Galishnikova et al. 2022, and references therein), or stretching scale (Schekochihin et al. 2004c), to describe the onset of saturation (as shown in Equation 38).

Let us first focus on the left column for the $P\nu = \infty$ simulations. The bottom panel shows the onset of the $E_{\text{mag}}(k)$ saturation w.r.t, the incompressible modes, which we can directly compare with the incompressible, $\text{Pm}_{\text{shear}} = 1$ simulations in Beattie et al. (2023). As Beattie et al. (2023) showed previ-

ously, in the kinematic stage there is an extended power law $E_{\text{mag}}(k) \sim k^2 E_{\text{kin},\perp}(k)$ up to the peak of $E_{\text{mag}}(k)/E_{\text{kin},\perp}(k)$. Throughout the nonlinear stage, the modes $k > k_{\text{eq}}$ are suppressed, in that $E_{\text{mag}}(k) \sim k^2 E_{\text{kin},\perp}(k)$ becomes significantly shallower, close to $E_{\text{mag}}(k) \sim k E_{\text{kin},\perp}(k)$. Based on our analysis in Section 3.2, this must be when the field growth is suppressed when the stretching is being suppressed, which is presumably happening on these scales. As the dynamo saturates, k_{eq} progressively moves from the peak of $E_{\text{mag}}(k)/E_{\text{kin},\perp}(k)$, $k \approx 100$, to $k \approx 10$, where it settles. $\hat{\mathbf{b}} \otimes \hat{\mathbf{b}} : \nabla \otimes \mathbf{v}$ should still be operational on these subequipartition scales, but now the stretching is slow, since the stretching time scale $t_k \sim 1/(k v_{\perp,k})$ becomes larger towards lower k modes (Schekochihin et al. 2004b). In the top panel, we see the same spectral ratio shape and final saturated state is not retained in the compressible modes, as we expect based on our integral statistics in Section 5.

Firstly, whilst $E_{\text{mag}}(k)/E_{\text{kin},\parallel}(k)$ retains similar power-law like structure into the peak as $E_{\text{mag}}(k)/E_{\text{kin},\perp}(k)$, the peak of $E_{\text{mag}}(k)/E_{\text{kin},\parallel}(k)$ is shifted to much smaller modes $k \approx 30$, and now a significant range of scales, the sub-shear-viscous scales, emerge at high- k with $E_{\text{mag}}(k)/E_{\text{kin},\parallel}(k) \approx 0.1$. Moreover, there is no clear change in the shape of $E_{\text{mag}}(k)/E_{\text{kin},\parallel}(k)$ as the dynamo saturates, in contrast to the suppression we see in the bottom panel. Naturally, there are two k_{eq} , the low- k k_{eq} corresponding to the transition between compressible modes that are in subequipartition, and hence strong enough to influence the field, and then the high- k k_{eq} , corresponding to the onset of the sub-shear-viscous range. Sandwiched in between are a range of scales that are in superequipartition, making the scale-by-scale saturation quite complex in the compressible modes of the $P\nu \gg 1$ plasmas.

Finally, we turn to the $P\nu = 0.01$ simulations in the right panels of Figure 14. For $E_{\text{mag}}(k)/E_{\text{kin},\perp}(k)$, a similar $k^2 \rightarrow k$ transition is found through the evolution from the kinematic to saturated state. From Figure 9, we showed that $E_{\text{kin},\perp}(k)$ modes $k \gtrsim 10$ are influenced by viscosity coupling. Compared to the $P\nu = \infty$ simulation, these modes are suppressed, with $E_{\text{mag}}(k)/E_{\text{kin},\perp}(k) \approx 2$ at the peak energy scale in saturation. It is also clear that k_{eq} takes a slower journey towards the low- k modes, albeit saturating to a similar value, which is probably the reason why that even at this low $P\nu$, the integral statistics shown in Section 5 do not vary significantly from the $P\nu = \infty$ case. Because $P\nu$ is small, the $E_{\text{mag}}(k)/E_{\text{kin},\parallel}(k)$ ratio is notably different from the incompressible counterpart. No sub-shear-viscous range exists, and hence the high- k modes are highly magnetised with respect to the compressible modes, finding values of $E_{\text{mag}}(k)/E_{\text{kin},\parallel}(k) \approx 10^3$. Furthermore, k_{eq} saturates to $k_{\text{eq}} \approx 1$. Intuitively, based on our previous findings, this means that all but the lowest compressible k modes are able to participate in the saturated state. As we commented upon previously, the key take away is that both the journey towards and the role in the saturation of the dynamo varies significantly for the compressible and incompressible velocity modes.

9 SUMMARY AND CONCLUSIONS

We perform three-dimensional, visco-resistive direct numerical simulations of trans-sonic, magnetohydrodynamic turbulence undergoing magnetic field amplification and satura-

tion through the small-scale dynamo, including viscous effects from both the shear and bulk viscosity. We list the conclusions below.

9.1 Bulk viscosity in the turbulent dynamo

To appropriately place bulk viscosity into a small-scale dynamo framework, we derive and define two new dimensionless numbers to study the role of bulk (volume) viscosity, the “bulk viscous Reynolds number” Re_{bulk} , Equation 20, which is the ratio between Reynolds stress and the bulk viscosity, as well as the “viscous Prandtl number” $\text{P}\nu$, Equation 21, which is the ratio between the bulk and shear viscosities (or equivalently, Reynolds numbers). For $\text{P}\nu < 1$, $\text{P}\nu$ defines the size of a sub-bulk-viscous range, $k_{\nu_{\text{shear}}} > k > k_{\nu_{\text{bulk}}}$, and for $\text{P}\nu > 1$, the sub-shear-viscous range, $k_{\nu_{\text{bulk}}} > k > k_{\nu_{\text{shear}}}$, which we illustrate in Figure 1. Intuitively, the bulk viscosity acts like a Laplacian-like viscosity operator that primarily affects the compressible modes, starting at high- k and shifting to low- k as $\text{P}\nu$ decreases.

In the $\text{P}\nu > 1$ regime, which simulations without explicit bulk viscosity will be in ($\text{P}\nu = \infty$), have a strong, high- k build-up of compressible modes that appear as a bottleneck in the total kinetic energy spectrum. For $\text{Pm}_{\text{shear}} = 1$ plasmas (Equation 25), where $k_{\nu_{\text{shear}}} = k_{\eta}$, this results in low-levels of magnetisation and high-levels of compressible kinetic energy building up on these scales. Whether or not this is desirable behaviour for simulations of astrophysical plasmas is therefore sensitive to the exact nature of bulk viscosity in the plasma of interest, but in general, the nature of bulk viscosity is largely unknown with a very limited amount of exploration in the literature both in the laboratory and in simulation. What is clear is that if one wants to do a compressible DNS where all viscous scales are resolved, one needs to use both ν_{bulk} and ν_{shear} , with $\text{P}\nu \sim 1$, otherwise the grid controls the dissipation of the compressible modes.

In the $\text{P}\nu < 1$ regime, the compressible and incompressible modes become coupled through the viscosity operators in the sub-bulk-viscous range. This means that as $k_{\nu_{\text{bulk}}}$ shifts to low- k , $k_{\nu_{\text{shear}}}$ shifts with it, which for fixed Pm_{shear} also brings k_{η} to lower k modes. When $\text{P}\nu$ is very low, such that $t_{\nu_{\text{bulk}}} \sim t_0$, there are significant changes in the shape of all energy spectra, dynamo integral energy statistics, and of course, an extremely strong suppression of compressible modes. If $\text{P}\nu$ is closer to one, the impact the bulk viscosity has on the dynamo is only in the high- k modes, and such, integral energies, growth rates, and saturations are largely unaffected. Future work is required to determine the relations for the scaling between $k_{\nu_{\text{bulk}}}$, $k_{\nu_{\text{shear}}}$ and k_{η} in the $\text{P}\nu < 1$ regime, where the coupling is strong.

9.2 Compressibility in the turbulent dynamo

To understand the role of compressible modes in the kinematic and saturated dynamo stages, we derive the 1st moment magnetic energy equation that separates out the effects of compressible and incompressible modes, in the sense that they are truly orthogonal contributions to the growth rate and saturation. This includes three main terms: volume-preserving stretching, volume-preserving winding and volume-changing compressions (Equation 7–9, respectively).

Winding is orthogonal to the magnetic field tensor, hence one cannot locally wind a turbulent magnetic field to grow it (see Equation 36). By directly computing the growth terms (Figure 7), we find that stretching is always the most dominant pathway for growing the magnetic field, even in the supersonic dynamo, and irrespective of the phase of the dynamo. This explains why $\ell_{\nu_{\text{shear}}}/\ell_{\eta} \sim \text{Pm}_{\text{shear}}^{1/2}$, (the stretching rate at $\ell_{\nu_{\text{shear}}}$ balances with resistive dissipation rate) is true for the compressible regime, which was recently found in Kriel et al. (2025). This is in tension with some recent results i.e., Sur & Subramanian (2023), but the tension is removed if they carefully remove the trace of \mathbb{S} in their decomposition (see footnote 4). Compression plays a dual, almost symmetric (at least at $\mathcal{M} = 1$) role, in both growing and decaying the magnetic field through compressions and dilatations. There is however a slight negative skew in the compression growth term, which means on average the compressions oppose the growth, resulting slightly slower growth rates and lower saturations than for the incompressible dynamo counterparts. At low- \mathcal{M} , these are however small effects. The largest effect on the growth rates are through correlations between the viscous dissipation scales (indeed in Section 6.3 we show that the viscous operators become correlated with $\sim 1/\text{P}\nu$). This means that the bulk viscosity ends up changing the growth rate by changing the shear viscous scale. This has flow on effects in the magnetic field structure.

By splitting the velocity field into compressible and incompressible modes, and analysing the saturation across k space, we come to the conclusion that at least for our parameter range it is only the very low- k compressible modes that are strong enough to influence the field through the nonlinear stage and saturation. Moreover, it is the low- k modes that dominate the integral energies, hence this is why changing the compressibility through various, large-scale parameterisations (changing \mathcal{M} , changing the compressible mode energy at the driving scale) is able to change the integral statistics and saturation energies in the turbulent dynamo.

9.3 Beyond the fluid continuum limit

Our study is embedded within the context of fluid plasma theory, where $\lambda_{\text{mfp}}/L \ll 1$, and λ_{mfp} is the molecular mean-free-path¹⁰. We have studied the implications of bulk viscosity $\sim \nabla \cdot (\nabla \cdot \mathbf{v})\mathbb{I}$ in $\mathcal{M} \approx 1$, turbulent dynamos, where shocks are able to permeate through the fluid medium. However, for collisionless $\lambda_{\text{mfp}}/L \gg 1$, weakly collisional $\lambda_{\text{mfp}}/L \sim 1$ and Braginskii (1965)-MHD the viscous properties of the plasma are significantly different from the vanilla MHD fluid form (Equation 11; St-Onge et al. 2020; Squire et al. 2023). For example, in Braginskii (1965)-MHD, which is important for plasmas in the intracluster medium (Berlok et al. 2020), particle collisions are rare, in turn preventing the pressure tensor from isotropising. This creates anisotropic viscous stress $\sim (\hat{\mathbf{b}} \otimes \hat{\mathbf{b}}) : \nabla \mathbf{v}$ along \mathbf{b} , taking the same form as our

¹⁰ For the interstellar medium, the cold neutral medium has an electron mean-free-path $\lambda_e \sim 5R_{\oplus}$, the warm neutral medium $\lambda_e \sim 1.3\text{AU}$, the warm ionised medium $\lambda_e \sim 0.17\text{AU}$ and the hot ionised medium $\lambda_e \sim 0.3\text{pc}$, with L varying between 10 to 100 pc (Ferrière 2020), hence the interstellar medium really is very well-approximated by a fluid.

dynamo growth terms Equation 35, making the competition for dynamo growth and viscous diffusion more fierce in this regime (St-Onge et al. 2020; Squire et al. 2023). As Squire et al. (2023) points out, whether or not either of these terms, $\sim \nabla \cdot \hat{\mathbf{b}} \otimes \hat{\mathbf{b}} [(\hat{\mathbf{b}} \otimes \hat{\mathbf{b}}) : \nabla \mathbf{v}]$ (Braginskii viscosity) or $\sim \nabla \cdot (\nabla \cdot \mathbf{v}) \mathbb{I}$ (bulk viscosity), are viscous dissipative or non-dissipative (i.e., akin to the thermal response of ∇p), depends strongly upon the aforementioned plasma regime (see footnote on page 10 in Squire et al. 2023 for a longer discussion). Interestingly, if we use our decomposition in Equation 35 for the Braginskii-MHD viscosity, we find that there is a bulk-viscous-type term $\sim (\hat{\mathbf{b}} \otimes \hat{\mathbf{b}}) : \mathbb{B}$, which will act to preferentially damp fast and slow magnetosonic waves along $\hat{\mathbf{b}}$. Furthermore, it has been seen in controlled laboratory astrophysics experiments that kinetic instabilities of the Weibel (1959)-type can play a critical role in the formation of collisionless shocks (Fox et al. 2013; Huntington et al. 2015). Whether such mechanisms can be parameterised at all in terms of viscosity coefficients remains an open question. We leave the detailed exploration of these bulk viscous-type operators in the context of these different plasma regimes for future studies.

ACKNOWLEDGEMENTS

We thank Bart Ripperda, Aditya Vijaykumar, Janosz Dewberry, Elias Most, Philip K.S. Kempster, Amit Seta, Mark Krumholz, Chris Thompson and Drummond Fielding for the helpful discussions. J. R. B. acknowledges financial support from the Australian National University, via the Deakin PhD and Dean’s Higher Degree Research (theoretical physics) Scholarships and the Australian Government via the Australian Government Research Training Program Fee-Offset Scholarship and the Australian Capital Territory Government funded Fulbright scholarship. C. F. acknowledges funding provided by the Australian Research Council (Future Fellowship FT180100495 and Discovery Project DP230102280), and the Australia-Germany Joint Research Cooperation Scheme (UA-DAAD). A. B. and J. R. B. also acknowledge the support from NSF Award 2206756. We further acknowledge high-performance computing resources provided by the Leibniz Rechenzentrum and the Gauss Centre for Supercomputing (grants pr32lo, pr48pi and GCS Large-scale project 10391), the Australian National Computational Infrastructure (grant ek9) and the Pawsey Supercomputing Centre (project pawsey0810) in the framework of the National Computational Merit Allocation Scheme and the ANU Merit Allocation Scheme.

The simulation software, FLASH, was in part developed by the FLASH Centre for Computational Science at the Department of Physics and Astronomy of the University of Rochester. We utilise the TURBGEN code for the turbulent forcing function, \mathbf{f} Federrath et al. (2022). Data analysis and visualisation software used in this study: C++ (Stroustrup 2013), NUMPY (Oliphant 2006; Harris et al. 2020), MATPLOTLIB (Hunter 2007), CYTHON (Behnel et al. 2011), VISIT (Childs et al. 2012), SCIPY (Virtanen et al. 2020), SCIKIT-IMAGE (van der Walt et al. 2014), CMASHER (van der Velden 2020).

DATA AVAILABILITY

The data underlying this article will be shared on reasonable request to the corresponding author.

REFERENCES

- Achikanath Chirakkara R., Federrath C., Trivedi P., Banerjee R., 2021, *Phys. Rev. Lett.*, **126**, 091103
- Aguilera-Miret R., Palenzuela C., Carrasco F., Viganò D., 2023a, *arXiv e-prints*, p. [arXiv:2307.04837](#)
- Aguilera-Miret R., Palenzuela C., Carrasco F., Viganò D., 2023b, *Phys. Rev. D*, **108**, 103001
- Batchelor G. K., 1950, *Proceedings of the Royal Society of London. Series A. Mathematical and Physical Sciences*, **201**, 405
- Beattie J. R., Federrath C., 2020, *MNRAS*, **492**, 668
- Beattie J. R., Federrath C., Klessen R. S., Schneider N., 2019, *MNRAS*, **488**, 2493
- Beattie J. R., Federrath C., Seta A., 2020, *MNRAS*, **498**, 1593
- Beattie J. R., Krumholz M. R., Federrath C., Sampson M. L., Crocker R. M., 2022a, *Frontiers in Astronomy and Space Sciences*, **9**, 900900
- Beattie J. R., Krumholz M. R., Sklidis R., Federrath C., Seta A., Crocker R. M., Mocz P., Kriel N., 2022b, *MNRAS*, **515**, 5267
- Beattie J. R., Mocz P., Federrath C., Klessen R. S., 2022c, *MNRAS*, **517**, 5003
- Beattie J. R., Federrath C., Kriel N., Mocz P., Seta A., 2023, *MNRAS*, **524**, 3201
- Beattie J. R., Federrath C., Klessen R. S., Cielo S., Bhat-tacharjee A., 2024, *arXiv e-prints*, p. [arXiv:2405.16626](#)
- Beck R., Wielebinski R., 2013, *Magnetic Fields in Galaxies*. p. 641, [doi:10.1007/978-94-007-5612-0_13](#)
- Behnel S., Bradshaw R., Citro C., Dalcin L., Seljebotn D. S., Smith K., 2011, *Computing in Science & Engineering*, **13**, 31
- Berlok T., Pakmor R., Pfrommer C., 2020, *MNRAS*, **491**, 2919
- Bott A. F. A., et al., 2021, *Phys. Rev. Lett.*, **127**, 175002
- Bouchut F., Klingenberg C., Waagan K., 2010, *Numerische Mathematik*, **115**, 647
- Braginskii S. I., 1965, *Reviews of Plasma Physics*, **1**, 205
- Brandenburg A., Ntormousi E., 2023, *ARA&A*, **61**, 561
- Brandenburg A., Subramanian K., 2005, *Phys. Rep.*, **417**, 1
- Brandenburg A., Procaccia I., Segel D., 1995, *Physics of Plasmas*, **2**, 1148
- Brandenburg A., Rogachevskii I., Schober J., 2023, *MNRAS*, **518**, 6367
- Brzycki B., ZuHone J., 2019, *The Astrophysical Journal*, **883**, 118
- Burgers J., 1948, *Advances in Applied Mechanics*, **1**, 171
- Burkhart B., 2021, *PASP*, **133**, 102001
- Burkhart B., Falceta-Gonçalves D., Kowal G., Lazarian A., 2009, *ApJ*, **693**, 250
- Camelio G., Gavassino L., Antonelli M., Bernuzzi S., Haskell B., 2023, *Phys. Rev. D*, **107**, 103031
- Chabanov M., Rezzolla L., 2023, *arXiv e-prints*, p. [arXiv:2307.10464](#)
- Chabanov M., Tootle S. D., Most E. R., Rezzolla L., 2023, *ApJ*, **945**, L14

- Chen S., Wang X., Wang J., Wan M., Li H., Chen S., 2019, *Physics of Fluids*, 31
- Childs H., et al., 2012, in , High Performance Visualization—Enabling Extreme-Scale Scientific Insight. Taylor & Francis, pp 357–372
- Choudhuri A. R., 1998, The physics of fluids and plasmas : an introduction for astrophysicists /
- Czajka A., Dasgupta K., Gale C., Jeon S., Misra A., Richard M., Sil K., 2019, *Journal of High Energy Physics*, 2019, 145
- Davidovits S., Federrath C., Teyssier R., Raman K. S., Collins D. C., Nagel S. R., 2022, *Phys. Rev. E*, 105, 065206
- Dubey A., et al., 2008, in Pogorelov N. V., Audit E., Zank G. P., eds, Astronomical Society of the Pacific Conference Series Vol. 385, Numerical Modeling of Space Plasma Flows. p. 145
- Emanuel G., 1990, *Physics of Fluids A: Fluid Dynamics*, 2, 2252
- Federrath C., 2013, *MNRAS*, 436, 1245
- Federrath C., 2016, *Journal of Plasma Physics*, 82, 535820601
- Federrath C., Banerjee S., 2015, *MNRAS*, 448, 3297
- Federrath C., Klessen R. S., 2012, *ApJ*, 761
- Federrath C., Roman-Duval J., Klessen R., Schmidt W., Mac Low M. M., 2010, *A&A*, 512
- Federrath C., Chabrier G., Schober J., Banerjee R., Klessen R. S., Schleicher D. R. G., 2011, *Phys. Rev. Lett.*, 107, 114504
- Federrath C., Schober J., Bovino S., Schleicher D. R. G., 2014, *ApJ*, 797, L19
- Federrath C., et al., 2016, *ApJ*, 832, 143
- Federrath C., Klessen R. S., Iapichino L., Beattie J. R., 2021, *Nature Astronomy*
- Federrath C., Roman-Duval J., Klessen R. S., Schmidt W., Mac Low M. M., 2022, TG: Turbulence Generator, Astrophysics Source Code Library, record ascl:2204.001 (ascl:2204.001)
- Ferrand R., Galtier S., Sahraoui F., Federrath C., 2020, *ApJ*, 904, 160
- Ferrière K., 2020, *Plasma Physics and Controlled Fusion*, 62, 014014
- Fox W., Fiksel G., Bhattacharjee A., Chang P.-Y., Germaschewski K., Hu S. X., Nilson P. M., 2013, *Phys. Rev. Lett.*, 111, 225002
- Frisch U., 1995, Turbulence. The legacy of A. N. Kolmogorov.
- Fryxell B., et al., 2000, *ApJS*, 131, 273
- Gaensler B. M., et al., 2011, *Nature*, 478, 214
- Galishnikova A. K., Kunz M. W., Schekochihin A. A., 2022, *Physical Review X*, 12, 041027
- Gent F. A., Mac Low M.-M., Korpi-Lagg M. J., Singh N. K., 2023, *ApJ*, 943, 176
- Grete P., O’Shea B. W., Beckwith K., Schmidt W., Christlieb A., 2017, *Physics of Plasmas*, 24, 092311
- Grete P., O’Shea B. W., Beckwith K., 2020, *ApJ*, 889, 19
- Grete P., O’Shea B. W., Beckwith K., 2023, *ApJ*, 942, L34
- Harris C. R., et al., 2020, *Nature*, 585, 357
- Haugen N. E. L., Brandenburg A., Dobler W., 2004a, *Phys. Rev. E*, 70, 016308
- Haugen N. E. L., Brandenburg A., Mee A. J., 2004b, *MNRAS*, 353, 947
- Hew J. K. J., Federrath C., 2023, *MNRAS*, 520, 6268
- Hopkins P. F., 2013, *MNRAS*, 430, 1880
- Hunter J. D., 2007, *Computing in Science & Engineering*, 9, 90
- Huntington C. M., et al., 2015, *Nature Physics*, 11, 173
- Jacquemin-Ide J., Rincon F., Tchekhovskoy A., Liska M., 2023, *arXiv e-prints*, p. arXiv:2311.00034
- Kazantsev A. P., 1968, Soviet Journal of Experimental and Theoretical Physics, 26, 1031
- Kempski P., Fielding D. B., Quataert E., Galishnikova A. K., Kunz M. W., Philippov A. A., Ripperda B., 2023, *MNRAS*, 525, 4985
- Klessen R. S., 2011, in Charbonnel C., Montmerle T., eds, EAS Publications Series Vol. 51, EAS Publications Series. pp 133–167 (arXiv:1109.0467), doi:10.1051/eas/1151009
- Kolmogorov A. N., 1941, *Doklady Akademii Nauk Sssr*, 30, 301
- Kriel N., Beattie J. R., Seta A., Federrath C., 2022, *MNRAS*, 513, 2457
- Kriel N., Beattie J. R., Federrath C., Krumholz M. R., Hew J. K. J., 2025, *MNRAS*, 537, 2602
- Kritsuk A. G., Norman M. L., Padoan P., Wagner R., 2007, *ApJ*, 665, 416
- Krumholz M. R., Federrath C., 2019, *Frontiers in Astronomy and Space Sciences*, 6, 7
- Krumholz M. R., Crocker R. M., Xu S., Lazarian A., Rosevear M. T., Bedwell-Wilson J., 2020, *MNRAS*, 493, 2817
- Landau L., Lifshitz E., 1959, Fluid Mechanics: Landau and Lifshitz: Course of Theoretical Physics. Butterworth-Heinemann
- Lehmann A., Federrath C., Wardle M., 2016, *MNRAS*, 463, 1026
- Lemoine M., 2023, *Journal of Plasma Physics*, 89, 175890501
- Lithwick Y., Goldreich P., 2001, *ApJ*, 562, 279
- Malvadi Shivakumar L., Federrath C., 2023, *arXiv e-prints*, p. arXiv:2311.10350
- Mandal A., Federrath C., Körtgen B., 2020, *Monthly Notices of the Royal Astronomical Society*, 493, 3098
- Marder B., 1987, *Journal of Computational Physics*, 68, 48
- Mathew S. S., Federrath C., 2021, *MNRAS*, 507, 2448
- McKee C. F., Stacy A., Li P. S., 2020, *MNRAS*, 496, 5528
- Mee A. J., Brandenburg A., 2006, *MNRAS*, 370, 415
- Mininni P., Alexakis A., Pouquet A., 2005, *Phys. Rev. E*, 72, 046302
- Mocz P., Burkhart B., 2019, *ApJ*, 884, L35
- Moffatt H. K., Saffman P. G., 1964, *The Physics of Fluids*, 7, 155
- Molina F. Z., Glover S. C. O., Federrath C., Klessen R. S., 2012, *MNRAS*, 423, 2680
- Most E. R., Haber A., Harris S. P., Zhang Z., Alford M. G., Noronha J., 2022a, *arXiv e-prints*, p. arXiv:2207.00442
- Most E. R., et al., 2022b, *MNRAS*, 509, 1096
- Nolan C. A., Federrath C., Sutherland R. S., 2015, *MNRAS*, 451, 1380
- Oliphant T., 2006, NumPy: A guide to NumPy, USA: Trelgol Publishing, <http://www.numpy.org/>
- Orkisz J. H., et al., 2017, *A&A*, 599, A99
- Padoan P., Nordlund Å., 2011, *ApJ*, 730, 40
- Pakmor R., Marinacci F., Springel V., 2014, The Astrophysical Journal Letters, 783, L20
- Pakmor R., et al., 2017, Monthly Notices of the Royal Astronomical Society, 469, 3185
- Pan S., Johnsen E., 2017, *Journal of Fluid Mechanics*, 833, 717–744

- Park J., Ryu D., 2019, *ApJ*, **875**, 2
- Passot T., Vázquez-Semadeni E., 1998, *Phys. Rev. E*, **58**, 4501
- Pfrommer C., Werhahn M., Pakmor R., Girichidis P., Simpson C. M., 2022, Monthly Notices of the Royal Astronomical Society, 515, 4229
- Rincon F., 2019, *Journal of Plasma Physics*, **85**, 205850401
- Ruzmaikin A. A., Sokolov D. D., 1981, *Pisma v Astronomicheskii Zhurnal*, **7**, 701
- Sampson M. L., Beattie J. R., Krumholz M. R., Crocker R. M., Federrath C., Seta A., 2023, *MNRAS*, **519**, 1503
- Schekochihin A. A., Cowley S. C., Hammett G. W., Maron J. L., McWilliams J. C., 2002a, *New Journal of Physics*, **4**, 84
- Schekochihin A. A., Boldyrev S. A., Kulsrud R. M., 2002b, *ApJ*, **567**, 828
- Schekochihin A. A., Boldyrev S. A., Kulsrud R. M., 2002c, *ApJ*, **567**, 828
- Schekochihin A. A., Cowley S. C., Maron J. L., McWilliams J. C., 2004a, *Physical review letters*, **92**, 054502
- Schekochihin A. A., Cowley S. C., Taylor S. F., Hammett G. W., Maron J. L., McWilliams J. C., 2004b, *Phys. Rev. Lett.*, **92**, 084504
- Schekochihin A. A., Cowley S. C., Taylor S. F., Maron J. L., McWilliams J. C., 2004c, *The Astrophysical Journal*, **612**, 276
- Schmidt W., Grete P., 2019, *Phys. Rev. E*, **100**, 043116
- Schmidt W., Federrath C., Klessen R., 2008, *Phys. Rev. Lett.*, **101**, 194505
- Schmidt W., Federrath C., Hupp M., Kern S., Niemeyer J. C., 2009, *A&A*, **494**, 127
- Schober J., Schleicher D., Federrath C., Klessen R., Banerjee R., 2012, *Phys. Rev. E*, **85**, 026303
- Schober J., Schleicher D. R. G., Federrath C., Bovino S., Klessen R. S., 2015, *Phys. Rev. E*, **92**, 023010
- Seta A., Federrath C., 2020, *MNRAS*, **499**, 2076
- Seta A., Federrath C., 2021, *Physical Review Fluids*, **6**, 103701
- Seta A., Bhat P., Subramanian K., 2015, *Journal of Plasma Physics*, **81**, 395810503
- Seta A., Bushby P. J., Shukurov A., Wood T. S., 2020, *Physical Review Fluids*, **5**, 043702
- Shang J., Wu T., Wang H., Xu W., Ye C., Hu R., Tao J., He X., 2020, *IEEE Access*, **8**, 40909
- Sharma B., Kumar R., 2019, *Phys. Rev. E*, **100**, 013309
- Sharma B., Kumar R., 2023, *arXiv e-prints*, p. arXiv:2303.08400
- Skalidis R., Sternberg J., Beattie J. R., Pavlidou V., Tassis K., 2021, *A&A*, **656**, A118
- Squire J., Hopkins P. F., 2017, *MNRAS*, **471**, 3753
- Squire J., Kunz M. W., Arzamasskiy L., Johnston Z., Quataert E., Schekochihin A. A., 2023, *Journal of Plasma Physics*, **89**, 905890417
- St-Onge D. A., Kunz M. W., Squire J., Schekochihin A. A., 2020, *Journal of Plasma Physics*, **86**, 905860503
- Steinwandel U. P., Dolag K., Böss L., Marin-Gilabert T., 2023, *arXiv e-prints*, p. arXiv:2306.04692
- Stokes G. G., 1850, On the Effect of the Internal Friction of Fluids on the Motion of Pendulums. Cambridge University Press, p. 1–10, doi:10.1017/CBO9780511702266.002
- Stroustrup B., 2013, The C++ Programming Language, 4th edn. Addison-Wesley Professional
- Sur S., Subramanian K., 2023, *MNRAS*,
- Tisza L., 1942, *Phys. Rev.*, **61**, 531
- Tobias S., 2021, *Journal of Fluid Mechanics*, **912**, P1
- Touber E., 2019, *Journal of Fluid Mechanics*, **875**, 974–1003
- Uhlenbeck G. E., Ornstein L. S., 1930, *Physical Review*, **36**, 823
- Verma M. K., 2017, *Reports on Progress in Physics*, **80**, 087001
- Virtanen P., et al., 2020, *Nature Methods*, **17**, 261
- Waagan K., Federrath C., Klingenberg C., 2011, *Journal of Computational Physics*, **230**, 3331
- Wang J., Wan M., Chen S., Xie C., Chen S., 2018a, *Phys. Rev. E*, **97**, 043108
- Wang J., Wan M., Chen S., Chen S., 2018b, *Journal of Fluid Mechanics*, **841**, 581–613
- Weibel E. S., 1959, *Phys. Rev. Lett.*, **2**, 83
- White T. G., et al., 2019, *Nature Communications*, **10**, 1758
- Whittingham J., Sparre M., Pfrommer C., Pakmor R., 2021, Monthly Notices of the Royal Astronomical Society, 506, 229
- Whittingham J., Sparre M., Pfrommer C., Pakmor R., 2023, arXiv preprint arXiv:2301.13208
- Xu S., Lazarian A., 2016, *ApJ*, **833**, 215
- Yousef T. A., Rincon F., Schekochihin A. A., 2007, *Journal of Fluid Mechanics*, **575**, 111
- Zel'dovich Y. B., Ruzmaikin A. A., Molchanov S. A., Sokolov D. D., 1984, *Journal of Fluid Mechanics*, **144**, 1
- van der Velden E., 2020, *The Journal of Open Source Software*, **5**, 2004
- van der Walt S., et al., 2014, *PeerJ*, **2**, e453

APPENDIX A: NON-DISSIPATIVE PROPERTY OF \mathbb{A} , THE RATE OF ROTATION TENSOR

While the rate of strain tensor Equation 8 contributes to shearing deformation through isochoric transformations of fluid parcels, the rate of rotation tensor Equation 10, instead represents rigid body rotations about a point. The latter can be shown to neither grow nor dissipate energy¹¹. We show this by constructing the E_{kin} equation by left-multiplying $\mathbf{v} \cdot$ to the strong form of the MHD momentum equation Equation 41 with zero external forcing ($\rho \mathbf{f} = 0$),

$$\frac{\partial E_{\text{kin}}}{\partial t} + \mathbf{v} \cdot \nabla \cdot \left[\rho \mathbf{v} \otimes \mathbf{v} - \frac{1}{4\pi} \mathbf{b} \otimes \mathbf{b} + p \mathbb{I} - \rho \boldsymbol{\sigma} \right] = 0, \quad (\text{A1})$$

where p is the total (thermal and magnetic) pressure. We direct our attention solely to the term involving the fully decomposed viscous stress tensor with \mathbb{A} (indices explicitly shown for clarity),

$$\mathbf{v} \cdot \nabla \cdot (\rho \mathbb{A}) = v_i \mathbb{A}_{ij} \partial_j \rho + \rho v_i \partial_j \mathbb{A}_{ij}, \quad (\text{A2})$$

where $\rho v_i \partial_j \mathbb{A}_{ij} = -\rho v_i \partial_j \mathbb{A}_{ji}$ and $v_i \mathbb{A}_{ij} \partial_j \rho = -v_i \mathbb{A}_{ji} \partial_j \rho$, where we have applied the skew-symmetric property of \mathbb{A} ,

¹¹ Note that even though \mathbb{A} does not couple to $\partial_t b^2$, it does couple to $\partial_t \hat{\mathbf{b}}$ through $\hat{b}_i \mathbb{A}_{ij}$, where $\hat{\mathbf{b}}$ is the magnetic unit vector. So even though \mathbb{A} does not directly change the amplitude, it can change the orientation of the magnetic field, which is undoubtedly a key aspect of the turbulent dynamo (Seta & Federrath 2021; Sur & Subramanian 2023; Beattie et al. 2024).

i.e., $\mathbb{A}_{ij} = -\mathbb{A}_{ji}$. Expanding the sum of either $\rho v_i \partial_j \mathbb{A}_{ij}$ or $v_i \mathbb{A}_{ij} \partial_j \rho$, one then finds that due to the skew-symmetric property of \mathbb{A}_{ij} , each term has a corresponding term that cancels the other out, e.g.,

$$\rho v_i \partial_j \mathbb{A}_{ij} = \rho \left(\underbrace{v_x \partial_y \mathbb{A}_{xy} + v_y \partial_x \mathbb{A}_{yx}}_0 + \dots \right) = 0. \quad (\text{A3})$$

Therefore, \mathbb{A} has no contribution of the evolution (growth or dissipation) in the viscous stress term in the kinetic energy evolution, and hence need not be considered in the isotropic-deviatoric decomposition of the viscous stress tensor, [Equation 11](#).

APPENDIX B: EXPRESSING THE 1st MOMENT MAGNETIC ENERGY EQUATION IN TERMS OF TENSOR OPERATIONS

In our main study, we present [Equation 30](#), which is a compressible version of 1st moment of the magnetic equation shown in [Schekochihin et al. \(2004c\)](#). [Seta et al. \(2020\)](#) and [Sur & Subramanian \(2023\)](#) derive a similar 1st moment magnetic energy equation, but we explicitly derive it in terms of tensor products, unlike either of these studies, so that we can apply our $\nabla \otimes \mathbf{v}$ decomposition, [Equation 35](#). The non-relativistic induction equation with Ohmic dissipation is,

$$\frac{\partial \mathbf{b}}{\partial t} = \nabla \times (\mathbf{v} \times \mathbf{b}) + \eta \nabla^2 \mathbf{b}. \quad (\text{B1})$$

Now taking the scalar product with \mathbf{b} ,

$$\frac{\partial b^2}{\partial t} = 2\mathbf{b} \cdot \nabla \times (\mathbf{v} \times \mathbf{b}) + 2\eta \mathbf{b} \cdot \nabla^2 \mathbf{b}, \quad (\text{B2})$$

where

$$\nabla \times (\mathbf{v} \times \mathbf{b}) = \mathbf{b} \cdot \nabla \otimes \mathbf{v} - \mathbf{b}(\nabla \cdot \mathbf{v}) - \mathbf{v} \cdot \nabla \otimes \mathbf{b}, \quad (\text{B3})$$

and,

$$\mathbf{b} \cdot \nabla \times (\mathbf{v} \times \mathbf{b}) = \mathbf{b} \otimes \mathbf{b} : \nabla \otimes \mathbf{v} \quad (\text{B4})$$

$$- \mathbf{b} \otimes \mathbf{b} : (\nabla \cdot \mathbf{v}) \mathbb{I} - \mathbf{b} \otimes \mathbf{v} : \nabla \otimes \mathbf{b}. \quad (\text{B5})$$

The last term can be simplified,

$$\mathbf{b} \otimes \mathbf{v} : \nabla \otimes \mathbf{b} = \frac{1}{2} \nabla \cdot (\mathbf{v} b^2) - \frac{1}{2} \mathbf{b} \otimes \mathbf{b} : (\nabla \cdot \mathbf{v}) \mathbb{I}, \quad (\text{B6})$$

which means

$$\mathbf{b} \cdot \nabla \times (\mathbf{v} \times \mathbf{b}) = \mathbf{b} \otimes \mathbf{b} : \nabla \otimes \mathbf{v} \quad (\text{B7})$$

$$- \frac{1}{2} \mathbf{b} \otimes \mathbf{b} : (\nabla \cdot \mathbf{v}) \mathbb{I} - \frac{1}{2} \nabla \cdot (\mathbf{v} b^2). \quad (\text{B8})$$

The dissipation term is simply,

$$\mathbf{b} \cdot \nabla^2 \mathbf{b} = \mathbf{b} \cdot \nabla \cdot (\nabla \otimes \mathbf{b}). \quad (\text{B9})$$

Hence the dynamical equation for b^2 is

$$\begin{aligned} \frac{\partial b^2}{\partial t} = 2 \left[\mathbf{b} \otimes \mathbf{b} : \nabla \otimes \mathbf{v} - \frac{1}{2} \mathbf{b} \otimes \mathbf{b} : (\nabla \cdot \mathbf{v}) \mathbb{I} - \frac{1}{2} \nabla \cdot (\mathbf{v} b^2) \right] \\ + 2\eta [\mathbf{b} \cdot \nabla \cdot (\nabla \otimes \mathbf{b})], \end{aligned} \quad (\text{B10})$$

Now we take the 1st spatial moments of the equation and divide by 8π to put the time-derivative in our energy density

unit system,

$$\begin{aligned} \frac{\partial \langle E_{\text{mag}} \rangle_{\mathcal{V}}}{\partial t} = \frac{2}{8\pi} \left\langle \mathbf{b} \otimes \mathbf{b} : \nabla \otimes \mathbf{v} - \mathbf{b} \otimes \mathbf{b} : \frac{1}{2} (\nabla \cdot \mathbf{v}) \mathbb{I} \right\rangle_{\mathcal{V}} \\ + \frac{2\eta}{8\pi} \langle \mathbf{b} \cdot \nabla \cdot (\nabla \otimes \mathbf{b}) \rangle_{\mathcal{V}}, \end{aligned} \quad (\text{B11})$$

where $\langle \frac{1}{2} \nabla \cdot (\mathbf{v} b^2) \rangle_{\mathcal{V}} = 0$ because there is no net magnetic flux through the triply periodic boundary. This is in every way equivalent to [Seta et al. \(2020\)](#), but we retain the full $\nabla \otimes \mathbf{v}$, instead of just \mathbb{S} (see [Section 3.2](#) for more discussions on how $\nabla \otimes \mathbf{v}$ also contains tensorial compression effects), as we mentioned in the main text. We do not retain the advection term in the 1st moment, as in [Sur & Subramanian \(2023\)](#). Now we simplify the dissipation term to get to the form expressed in [Schekochihin et al. \(2004c\)](#). Firstly,

$$\langle \mathbf{b} \cdot \nabla \cdot (\nabla \otimes \mathbf{b}) \rangle_{\mathcal{V}} = \int_{\mathcal{V}} d\mathcal{V} \mathbf{b} \cdot \nabla \cdot (\nabla \otimes \mathbf{b}), \quad (\text{B12})$$

which by parts $\int u dv = uv - \int v du$, where $u = \mathbf{b}$, $du = \nabla \otimes \mathbf{b}$, $dv = \nabla \cdot (\nabla \otimes \mathbf{b})$, $v = \nabla \otimes \mathbf{b}$ is

$$\int_{\mathcal{V}} d\mathcal{V} \mathbf{b} \cdot \nabla \cdot (\nabla \otimes \mathbf{b}) = \mathbf{b} \cdot \nabla \otimes \mathbf{b} \Big|_{-\infty}^{\infty} \quad (\text{B13})$$

$$- \int_{\mathcal{V}} d\mathcal{V} (\nabla \otimes \mathbf{b}) : (\nabla \otimes \mathbf{b}), \quad (\text{B14})$$

where the first term in the integral goes to zero due to periodicity. Hence,

$$\langle \mathbf{b} \cdot \nabla \cdot (\nabla \otimes \mathbf{b}) \rangle_{\mathcal{V}} = - \langle (\nabla \otimes \mathbf{b}) : (\nabla \otimes \mathbf{b}) \rangle_{\mathcal{V}}. \quad (\text{B15})$$

Finally, we put this expression back into our evolution equation, and multiply and divide by the integral energy density to get

$$\begin{aligned} \frac{\partial \langle E_{\text{mag}} \rangle_{\mathcal{V}}}{\partial t} = \frac{2 \langle E_{\text{mag}} \rangle_{\mathcal{V}}}{\langle b^2 \rangle_{\mathcal{V}}} \left\langle (\mathbf{b} \otimes \mathbf{b}) : (\nabla \otimes \mathbf{v}) \right. \\ \left. - (\mathbf{b} \otimes \mathbf{b}) : \left(\frac{1}{2} (\nabla \cdot \mathbf{v}) \mathbb{I} \right) \right\rangle_{\mathcal{V}} \\ - \frac{2\eta \langle E_{\text{mag}} \rangle_{\mathcal{V}}}{\langle b^2 \rangle_{\mathcal{V}}} \langle (\nabla \otimes \mathbf{b}) : (\nabla \otimes \mathbf{b}) \rangle_{\mathcal{V}}, \end{aligned} \quad (\text{B16})$$

the 1st moment equations shown in [Equation 30](#).

APPENDIX C: RESOLUTION STUDY

In this section we provide a resolution study for our $P\nu = 1$ and $P\nu = 0.1$ simulations, showing both the integral energy statistics, as in [Figure 5](#), in [Figure C1](#) and [Figure C2](#), and the Helmholtz decomposed spectra in [Figure C3](#) and [Figure C4](#), for $P\nu = 1$ and $P\nu = 0.1$, respectively. All statistics are coloured by the grid resolution, $N_{\text{grid}}^3 = 128^3, 256^3, 512^3$ and (only for $P\nu = 1$) 1024^3 . Beyond 256^3 , the integral energy statistics show strong agreement, both in saturation and in growth rates (see [Table 1](#)), with very little deviation based on the grid resolution. As we have pointed out in the main text, this is because the energy integral statistics are always dominated by the low- k modes ([Beattie et al. 2022a](#)), so we expect them to converge quickly, and at low grid resolutions. Similarly for the growth rates, because we have only moderate

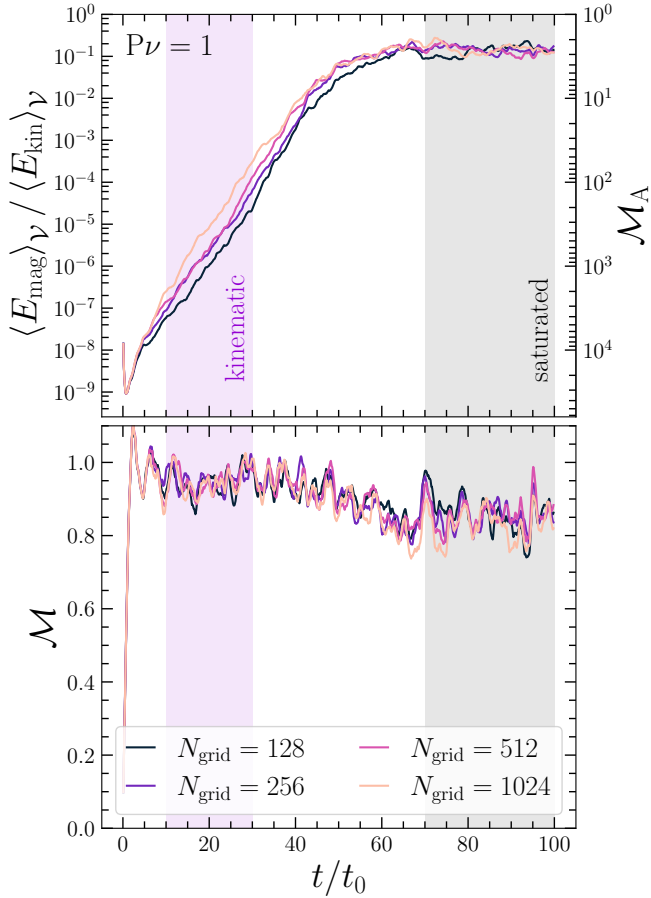


Figure C1. The same as Figure 5 but instead of colouring by $P\nu$, we fix $P\nu = 1$ and change grid resolution of the simulation, N_{grid} . We list the growth rate γ_1 and the final saturation of $\langle E_{\text{mag}} \rangle_{\nu} / \langle E_{\text{kin}} \rangle_{\nu}$ in Table 1, and find good convergence for both γ_1 and $\langle E_{\text{mag}} \rangle_{\nu} / \langle E_{\text{kin}} \rangle_{\nu}$ saturation at $N_{\text{grid}} \approx 256$.

$\text{Re}_{\text{shear}} = 1000$ the growth rates, which are sensitive to $\ell_{\nu_{\text{shear}}}$, also converge quickly.

Now we compare the decomposed kinetic energy spectra in Figure C3 and Figure C4. Firstly, we can confidently say that the $P\nu = 0.1$ simulation is converged on all scales at 512^3 . That is, the physical length scales associated with the bulk and shear viscosity are properly resolved in the domain, since both $E_{\text{kin},\parallel}(k)$ and $E_{\text{kin},\perp}(k)$ trace each other almost perfectly through all the k modes, and then truncate before the Nyquist frequency. Furthermore, as we expect from our definition of \mathbb{B} (bulk viscosity operator; see Equation 35), the overall structure of the two spectra are almost identical, i.e., $k_{\nu_{\text{shear}}} \approx k_{\nu_{\text{bulk}}}$ (which should be exact for $P\nu = 1/3$). However, for the $P\nu = 1$ simulation, $k_{\nu_{\text{shear}}}$ looks resolved between 256^3 and 512^3 (as expected from our growth rates), but $k_{\nu_{\text{bulk}}}$ does not, i.e., at $P\nu = 1$, we do not have sufficient resolution, even at 1024^3 , to resolve the entire sub-shear-viscous range, which we see growing in size in the $E_{\text{kin},\parallel}(k)/E_{\text{kin},\perp}(k)$ Figure C3 inset, reaching values up to $E_{\text{kin},\parallel}(k)/E_{\text{kin},\perp}(k) = 10^3$ within this range of scales. This would be a problem if in our study we focused on measuring precise viscous dissipation scales, and viscous scale relations. However, we focus on a mode-by-mode analysis, for the most part, and one can

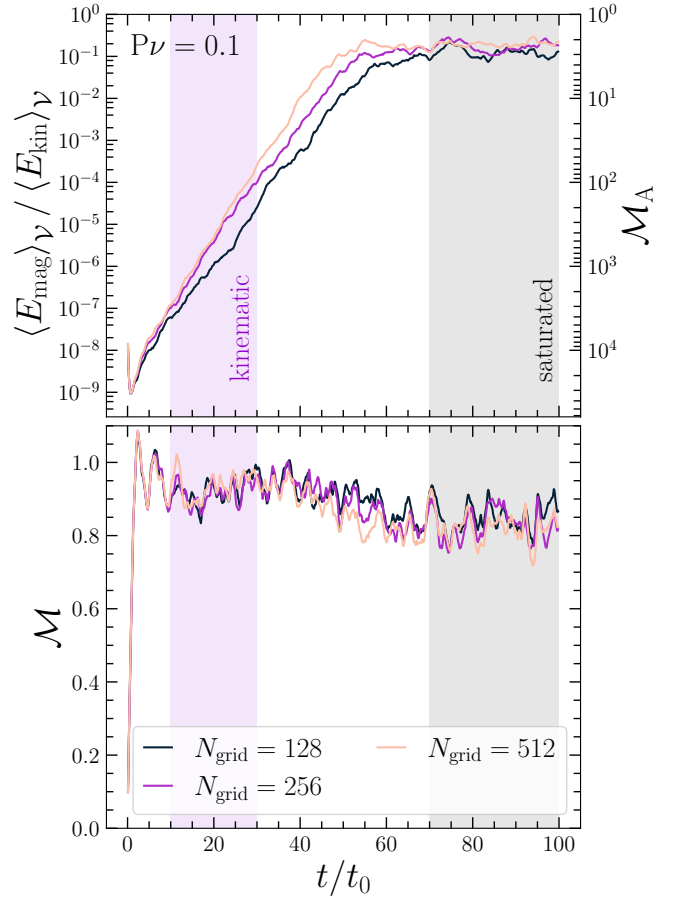


Figure C2. The same as Figure C1 but for $P\nu = 0.1$. At low $P\nu$, we similar convergence properties as the $P\nu = 1$ simulation, for both γ_1 and the $\langle E_{\text{mag}} \rangle_{\nu} / \langle E_{\text{kin}} \rangle_{\nu}$ saturation.

read off from Figure C3, that even though the physical $k_{\nu_{\text{bulk}}}$ is not resolved, we get relatively good convergence up to the $k \approx 100$ mode before there is significant deviation between the spectra due to numerical (compressible) viscosity. This is completely sufficient for our study. This also highlights that for *no* explicit \mathbb{B} viscosity ($P\nu = \infty$), we should not expect any convergence of the high- k compressible modes and $E_{\text{kin},\parallel}(k)/E_{\text{kin},\perp}(k)$ should grow unbounded as N_{grid}^3 increases, which exactly what one expects for an ILES.

APPENDIX D: COMPRESSIBLE AND INCOMPRESSIBLE 1st MOMENT ENERGY EQUATIONS

We stated the Stokes limit for the compressible and incompressible 1st moment kinetic equations in Section 6.3. Here we derive the full equations and take the Stokes limit to demonstrate how we got to Equation 56 and Equation 55. We start with the dimensionless isothermal momentum equation,

$$\begin{aligned} \frac{\partial \rho \mathbf{v}}{\partial t} + \nabla \cdot \left(\rho \mathbf{v} \otimes \mathbf{v} - \frac{1}{\mathcal{M}_A^2} \mathbf{b} \otimes \mathbf{b} + \frac{1}{\mathcal{M}^2} \rho \mathbb{I} + \frac{1}{\mathcal{M}_A^2} b^2 \mathbb{I} \right) \\ = \nabla \cdot \left(\frac{2\rho}{\text{Re}_{\text{shear}}} \mathbb{S} + \frac{\rho}{\text{Re}_{\text{bulk}}} \mathbb{B} \right) \end{aligned} \quad (\text{D1})$$

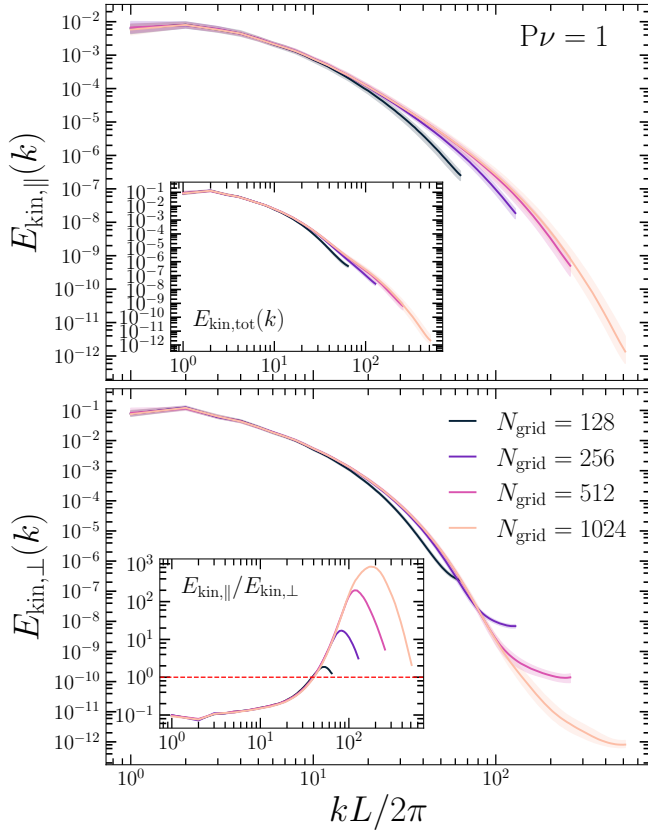


Figure C3. The compressible ($E_{\text{kin},\parallel}(k)$; top) and incompressible ($E_{\text{kin},\perp}(k)$; bottom) kinetic energy spectra for the $P\nu = 1.0$ ensemble of simulations (the same as the middle and bottom panel in Figure 9), tabulated in Table 1. The inset in the top panel shows the total kinetic energy $E_{\text{kin}}(k)$, and the inset in bottom panel shows the ratio between compressible and incompressible spectral kinetic energies, $E_{\text{kin},\parallel}(k)/E_{\text{kin},\perp}(k)$. We find good convergence in $E_{\text{kin},\perp}(k)$, flattening out well before the Nyquist frequency, indicating that $k\nu_{\text{shear}}$ is resolved. However, for $E_{\text{kin},\parallel}(k)$, the dissipation scale appears to be unresolved, which results in an extended sub-shear-viscous range of scales that grows with N_{grid} .

as in Section 2.2, and take the Stokes limit, $\text{Re}_{\text{bulk}} = \text{Re}_{\text{shear}} \rightarrow 0$, which maps us to the dynamical equations for the high- k , viscous modes in the sub-bulk-viscous range (see Figure 1),

$$\frac{\partial \rho \mathbf{v}}{\partial t} = \nabla \cdot \left(\frac{2}{\text{Re}_{\text{shear}}} \mathbb{S} + \frac{1}{\text{Re}_{\text{bulk}}} \mathbb{B} \right) \quad (\text{D2})$$

where we have assumed $\nabla \rho$ is small compared to $\sim \nabla \otimes \mathbf{v}$. Now taking the dot product with \mathbf{v}_{\perp} and taking ensemble averages,

$$\frac{1}{2} \frac{\partial \langle \rho v_{\perp}^2 \rangle_{\mathcal{V}}}{\partial t} = \frac{\partial \langle E_{\text{kin},\perp} \rangle_{\mathcal{V}}}{\partial t} \quad (\text{D3})$$

$$= \left\langle \mathbf{v}_{\perp} \cdot \nabla \cdot \left(\frac{2}{\text{Re}_{\text{shear}}} \mathbb{S} + \frac{1}{\text{Re}_{\text{bulk}}} \mathbb{B} \right) \right\rangle_{\mathcal{V}}, \quad (\text{D4})$$

utilising $\langle v_j \partial_t \rho v_i \rangle_{\mathcal{V}} = \partial_t \langle \rho v_j v_i \rangle_{\mathcal{V}}$ (Wang et al. 2018b). Decomposing the remaining total velocity terms into

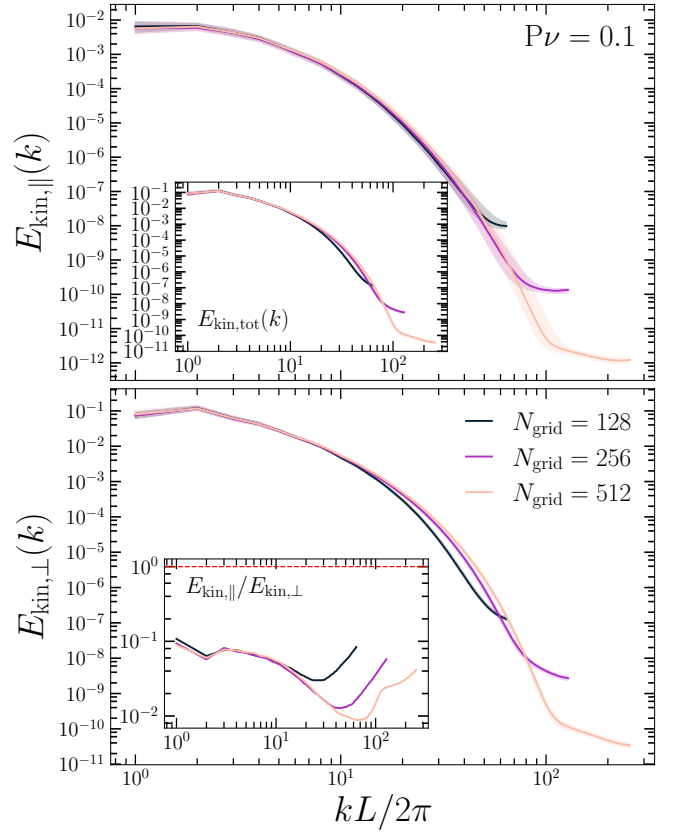


Figure C4. The same as Figure C3 but for the $P\nu = 0.1$ ensemble of simulations, which is the $P\nu$ where the bulk viscosity and shear viscosity are approximately equal. With the inclusion of bulk viscosity that matches the shear viscosity, $E_{\text{kin},\parallel}(k)$ now has a resolved dissipation scale that is (qualitatively) at a similar k mode as the dissipation scale in $E_{\text{kin},\perp}(k)$.

$\mathbf{v} = \mathbf{v}_{\perp} + \mathbf{v}_{\parallel}$, the first term is simply,

$$\frac{2}{\text{Re}_{\text{shear}}} \langle \mathbf{v}_{\perp} \cdot \nabla \cdot \mathbb{S} \rangle_{\mathcal{V}} = \frac{1}{\text{Re}_{\text{shear}}} \left\langle \mathbf{v}_{\perp} \cdot \nabla^2 \mathbf{v}_{\perp} + \frac{4}{3} \mathbf{v}_{\perp} \cdot \nabla^2 \mathbf{v}_{\parallel} \right\rangle_{\mathcal{V}}, \quad (\text{D5})$$

and the second term is,

$$\frac{1}{\text{Re}_{\text{bulk}}} \langle \mathbf{v}_{\perp} \cdot \nabla \cdot \mathbb{B} \rangle_{\mathcal{V}} = \frac{1}{\text{Re}_{\text{bulk}}} \langle \mathbf{v}_{\perp} \cdot \nabla^2 \mathbf{v}_{\parallel} \rangle_{\mathcal{V}}, \quad (\text{D6})$$

hence

$$\begin{aligned} \frac{\partial \langle E_{\text{kin},\perp} \rangle_{\mathcal{V}}}{\partial t} &= \left(\frac{4\text{Re}_{\text{shear}}^{-1}}{3} + \text{Re}_{\text{bulk}}^{-1} \right) \langle \mathbf{v}_{\perp} \cdot \nabla^2 \mathbf{v}_{\parallel} \rangle_{\mathcal{V}} \\ &+ \text{Re}_{\text{shear}}^{-1} \langle \mathbf{v}_{\perp} \cdot \nabla^2 \mathbf{v}_{\perp} \rangle_{\mathcal{V}}. \end{aligned} \quad (\text{D7})$$

Likewise for the 1st moment compressible kinetic energy equation,

$$\begin{aligned} \frac{\partial \langle E_{\text{kin},\parallel} \rangle_{\mathcal{V}}}{\partial t} &= \left(\frac{4\text{Re}_{\text{shear}}^{-1}}{3} + \text{Re}_{\text{bulk}}^{-1} \right) \langle \mathbf{v}_{\parallel} \cdot \nabla^2 \mathbf{v}_{\parallel} \rangle_{\mathcal{V}} \\ &+ \text{Re}_{\text{shear}}^{-1} \langle \mathbf{v}_{\parallel} \cdot \nabla^2 \mathbf{v}_{\perp} \rangle_{\mathcal{V}}. \end{aligned} \quad (\text{D8})$$

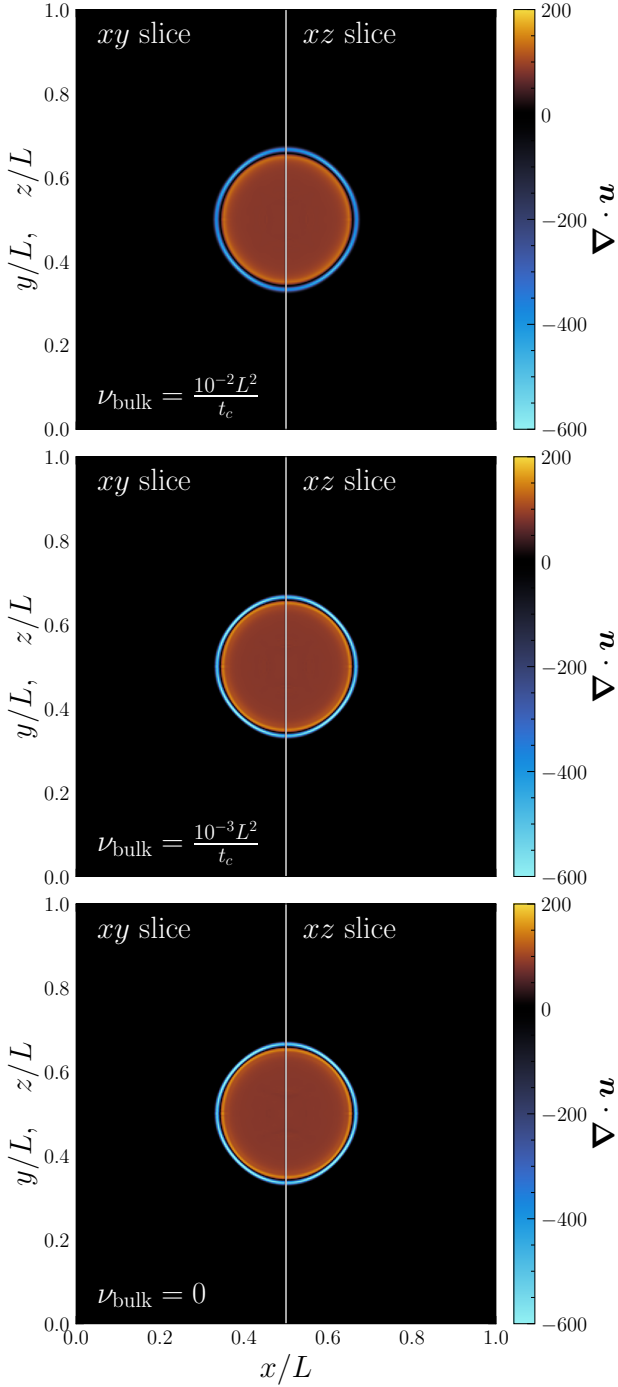


Figure D1. The velocity divergence from the three-dimensional Sedov test showing that bulk viscous fluxes are acting isotropically on the Sedov blast wave. Left of the vertical white line we show the xy slice, and right of the line the xz slice, with almost perfect symmetric between the two slices. Each panel as a different ν_{bulk} (labelled in the bottom-left corner), varying from the strongest, $\nu_{\text{bulk}} = 10^{-2}L^2/t_c$ (top), to the ideal limit, $\nu_{\text{bulk}} = 0$ (bottom). Each simulation is visualised at the same time realisation. The $\nu_{\text{bulk}} = 10^{-2}L^2/t_c$ simulation has a visibly thicker blast wave, with smaller $\nabla \cdot \mathbf{u}$ compared the ideal case.

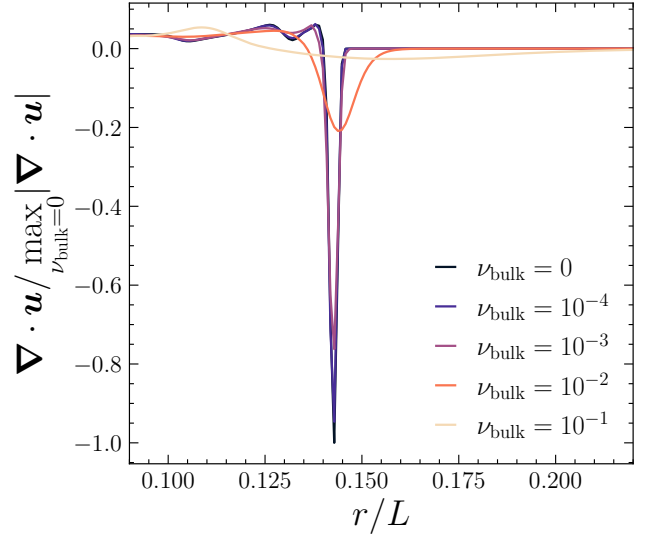


Figure D2. One-dimensional radial profiles of $\nabla \cdot \mathbf{u}$ for a two-dimensional Sedov-Taylor blast wave with varying ν_{bulk} , in units of L^2/t_c , all at the same $t/t_c = 10^{-2}$. The $\nabla \cdot \mathbf{u}$ is normalised by the absolute maximum $\nabla \cdot \mathbf{u}$ for the $\nu_{\text{bulk}} = 0$ simulation. As ν_{bulk} increases, the bulk viscosity strongly damps the compressive blast wave (strong $\nabla \cdot \mathbf{u} < 0$ region) and retards the evolution of the wave.

APPENDIX E: BULK VISCOSITY IMPLEMENTATION

E1 Viscous fluxes and explicit time-stepping

We add the bulk viscous fluxes following the split, second-order explicit scheme in our [Bouchut et al. \(2010\)](#) solver. This adds additional fluxes to each sweep in the solver, both in the momentum equation, $\mathbb{F}(\rho v)$ Equation 13 where fluxes are just directly σ , and the energy equation, $\mathbb{F}(\rho E)$ (not discussed in the main text, since the dynamo with isothermal equation of state), where fluxes are $\mathbf{v} \cdot \sigma$. Now we systematically go through of the cell-face fluxes added in each co-ordinate sweep of the momentum equation. We adopt the notation that $\overline{X_{ijk}} = (X_{ijk} + X_{i-1jk})/2$ is the average of quantity X_{ijk} between the cell center X_{ijk} and the cell face, e.g. for coordinate i , X_{i-1jk} . In three-dimensions, the additional momentum fluxes in the x sweep are,

$$\mathbb{F}_{\mathbb{B}}(\rho v_x) = -\frac{\nu_{\text{bulk}}}{2\Delta x} (v_{x,ijk} - v_{x,i-1jk}) \quad (\text{E1})$$

$$-\frac{\nu_{\text{bulk}}}{4\Delta y} (v_{y,ij+1k} - v_{y,ij-1k} + v_{y,i-1j+1k} - v_{y,i-1j-1k}) \quad (\text{E2})$$

$$-\frac{\nu_{\text{bulk}}}{4\Delta z} (v_{z,ijk+1} - v_{z,ijk-1} + v_{z,i-1jk+1} - v_{z,i-1jk-1}) \quad (\text{E3})$$

$$\approx \nu_{\text{bulk}} (\overline{\partial_x v_x} + \overline{\partial_y v_y} + \overline{\partial_z v_z}) \quad (\text{E4})$$

the y sweep,

$$\mathbb{F}_{\mathbb{B}}(\rho v_y) = -\frac{\nu_{\text{bulk}}}{4\Delta x} (v_{x,i+1jk} - v_{x,i-1jk} + v_{x,i+1j-1k} - v_{x,i-1j-1k}) \quad (\text{E5})$$

$$-\frac{\nu_{\text{bulk}}}{2\Delta y} (v_{y,ijk} - v_{y,ij-1k}) \quad (\text{E6})$$

$$-\frac{\nu_{\text{bulk}}}{4\Delta z} (v_{z,ijk+1} - v_{z,ijk-1} + v_{z,ij+1k+1} - v_{z,ij+1k-1}) \quad (\text{E7})$$

$$\approx \nu_{\text{bulk}} (\overline{\partial_x v_x} + \overline{\partial_y v_y} + \overline{\partial_z v_z}) \quad (\text{E8})$$

and the z sweep,

$$\mathbb{F}_{\mathbb{B}}(\rho v_z) = -\frac{\nu_{\text{bulk}}}{4\Delta x} (v_{x,i+1jk} - v_{x,i-1jk} + v_{x,i+1jk+1} - v_{x,i-1jk+1}) \quad (\text{E9})$$

$$-\frac{\nu_{\text{bulk}}}{4\Delta y} (v_{y,ij+1k} - v_{y,ij-1k} + v_{y,ij+1k+1} - v_{y,ij-1k+1}) \quad (\text{E10})$$

$$-\frac{\nu_{\text{bulk}}}{2\Delta z} (v_{z,ijk} - v_{z,ijk-1}) \quad (\text{E11})$$

$$\approx \nu_{\text{bulk}} (\overline{\partial_x v_x} + \overline{\partial_y v_y} + \overline{\partial_z v_z}) \quad (\text{E12})$$

noting that when the sweep is in the same direction as the derivative, the average over the center to the face can be algebraically simplified to just two terms. We perform the same for the $\mathbb{F}(\rho E)$, but with the additional \mathbf{v} scalar product that needs to be carried through the averages. Adding diffusion to our the MHD model makes it mixture of hyperbolic and parabolic equations. Since we are using an explicit scheme, $f_j^{n+1} = f_j^n + \Delta t \partial_i F_{ij}^n$, this changes the global Δt time-step to advance between state f_j^n to f_j^{n+1} , which is necessary to ensure numerical stability. The diffusion time step becomes,

$$\Delta t \leq \text{CFL} \min \left\{ \frac{1}{2} \frac{\Delta x^2}{\nu_{\text{shear}}}, \frac{1}{2} \frac{\Delta x^2}{\nu_{\text{bulk}}}, \frac{1}{2} \frac{\Delta x^2}{\eta} \right\}, \quad (\text{E13})$$

where CFL is the Courant–Friedrichs–Lewy number, and we have added an additional diffusion timescale for ν_{bulk} . This becomes costly for stiff problems, such as low ν_{bulk} , ν_{shear} and η , and at high-resolution, Δx^2 .

E2 Three-dimensional viscous Sedov test

A simple numerical test that we can perform to check that the fluxes have been added correctly is a bulk viscous version of the Sedov test in three-dimensions. Because Sedov-Taylor is an intrinsically isotropic test problem, we can use it to directly explore if the additional $\nu_{\text{bulk}} \nabla \cdot (\rho \nabla \cdot \mathbf{v})$ diffusion isotropically decays the strong $\nabla \cdot \mathbf{v} < 0$ shock wave from the explosion. We follow the standard Sedov setup, with a central enhancement of internal energy density, e , and hence pressure density p , in a small region $p = (\gamma - 1)e / [(4/3)\pi r^3]$, with γ , the adiabatic index and r the radial coordinate away from the center of three-dimensional and two-dimensional domains $[0, L]$ discretised with 288^3 grids in three-dimensions and 1024^2 in two-dimensions. All of the boundaries conform to outflow conditions. We use $p = 10^5 p_0$, where $p_0 = 1$ is the ambient pressure, and $\gamma = 7/5$ (diatomic γ equation of state), such that the solution to the problem is identical to the self-similar Taylor-von Neumann Sedov blastwave solution. For ambient density $\rho_0 = 1$, the sound speed in the

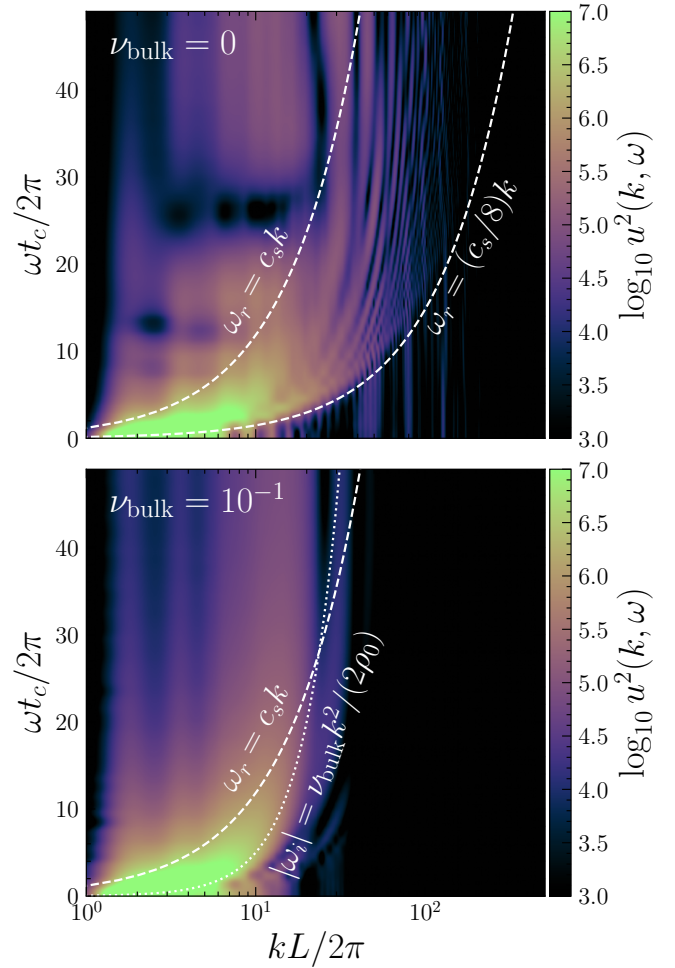


Figure E1. The velocity dispersion relation $\omega(k)$ for the two-dimensional Sedov-Taylor blast wave simulations with $\nu_{\text{bulk}} = 0$ (top panel) and $\nu_{\text{bulk}} = 10^{-1} L^2/t_c$ (bottom panel). We plot both real ω_r (dashed) and imaginary $|\omega_i|$ (dotted) components of the dispersion relation shown in Equation E15, describing a standard sound wave, ω_r , and the quadratic wave damping from ν_{bulk} , $|\omega_i|$. The top panel, where the blast wave is the strongest, shows deviations from the linear theory, due to the strong nonlinearity of the blast wave, especially at high- k and high- ω , which exhibit significant steepening. However, we still find with a some amount of low to moderate- k and ω sound waves, with lower sound speeds than $c_s = \sqrt{\gamma p_0/\rho_0}$. These modes are completely damped in the bottom panel, where ν_{bulk} is the highest. The only modes left are low- k , low- ω sound waves, bounded by the quadratic damping.

ambient medium is $c_s = \sqrt{\gamma p_0/\rho_0} = \sqrt{\gamma} = \sqrt{7/5}$. This provides a sound-crossing time $t_s = L/c_s = \sqrt{5/7}$, which we use to non-dimensionalise the runtime of the simulations.

We run three-dimensional simulations at $\nu_{\text{bulk}} = \{10^{-2}, 10^{-3}, 10^{-4}, 0\} L^2/t_c$, each simulation resulting in a factor of 10 smaller Δt . We show a visualisation of the xy and xz slices of $\nabla \cdot \mathbf{u}$ for three different simulations in Figure D1. The top is the most viscous simulation, $\nu_{\text{bulk}} = 10^{-2} L^2/t_c$, and the bottom is the ideal simulation, $\nu_{\text{bulk}} = 0$. All simulations are normalised to the same range of $\nabla \cdot \mathbf{u}$. The low and high divergence shell around the blast wave is dampened and thickened as ν_{bulk} increases, as expected, but the key result

of this plot is that the blast wave is isotropically symmetric, indicating that the bulk viscous fluxes have been added correctly in each sweep.

Since we know the fluxes have been added correctly in three-dimensions we turn to the two-dimensional problem, which is easier to run at higher resolutions and higher ν_{bulk} . We show a one-dimensional profile in $r = \sqrt{x^2 + y^2}$ for two-dimensional simulations at $\nu_{\text{bulk}} = \{10^{-1}, 10^{-2}, 10^{-3}, 10^{-4}, 0\} L^2/t_c$. The increasing ν_{bulk} diffuses the $\nabla \cdot \mathbf{u} = 0$ away, both in the strongly $\nabla \cdot \mathbf{u} < 0$ blast wave itself and in the $\nabla \cdot \mathbf{u} > 0$ post-shock region.

The final code test that we do is on the wave - ν_{bulk} viscosity interactions. In the absence of ν_{shear} , we can derive the linear dispersion relation from the Navier-Stokes equation,

$$\omega^2 + i\omega \frac{k^2}{\rho_0} \nu_{\text{bulk}} - c^2 k^2 = 0. \quad (\text{E14})$$

Assuming $\omega \frac{k^2}{\rho_0} \nu_{\text{bulk}} \ll c^2 k^2$ (i.e., the viscosity is slow compared to the sound speed), we find the approximate solutions for bulk viscous sound waves,

$$\omega \approx \underbrace{c_s k}_{\omega_r} - i \underbrace{\frac{\nu_{\text{bulk}}}{2\rho} k^2}_{\omega_i}, \quad (\text{E15})$$

where ω is the temporal frequency, ω_r is the real component, describing the classical dispersion relation for sound waves, and ω_i is the imaginary component, showing the wave damping from ν_{bulk} . W

e plot $\omega(k)$ for the two-dimensional simulations with $\nu_{\text{bulk}} = 0$ (top panel) and $\nu_{\text{bulk}} = 10^{-1} L^2/t_c$ (bottom panel) in Figure E1. We plot ω_r and $|\omega_i|$ on the dispersion relation for the one-dimensional u_i along r/L , to indicate which modes resemble linear sound waves and which modes are being quadratically damped by ν_{bulk} . We use $c_s = \sqrt{\gamma p_0/\rho_0} = \sqrt{7/5}$ and $\rho = \rho_0$, even though both c_s and ρ change as a function of time and space. For the $\nu_{\text{bulk}} = 0$ case, we see a range of signatures from linear sound waves with different temperatures (most likely due to the post and pre-shock temperatures changing $c_s \propto \sqrt{T}$) but most of the energy is in the low- k , low- ω sound wave. At high- k , we see significant steepening, which is expected for nonlinear structures like shocks. There are a large range of cooler $\sqrt{7/5}/8 \leq c_s \leq \sqrt{7/5}$ sound waves moving from low- k , low- ω to moderate- k , moderate- ω . All of these modes are suppressed (indeed, truncated more or less right at $|\omega_i|$) in the strong ν_{bulk} case. The only feature left is the low- k , low- ω structure, that closely resembles a sound wave with $c_s = \sqrt{7/5}$. Hence, more or less as we show in the main text, the bulk viscosity suppresses the high- k sound waves, gets rid of any nonlinear mode steepening from shocks, and leaves only the low- k sounds waves. We see no significant artefacts and the process that we describe qualitatively matches the linear theory well, hence we conclude that the bulk viscosity implementation is working as it should.

This paper has been typeset from a T_EX/L^AT_EX file prepared by the author.